

SYNTHESIS OF DISPERSIBLE LiFePO_4 PARTICLES WITH CONTROLLED
SIZE AND MORPHOLOGY VIA POLYOL ROUTE

A THESIS SUBMITTED TO
THE GRADUATE SCHOOL OF NATURAL AND APPLIED SCIENCES
OF
MIDDLE EAST TECHNICAL UNIVERSITY

BY

ELİF COŞKUN

IN PARTIAL FULFILLMENT OF THE REQUIREMENTS
FOR
THE DEGREE OF MASTER OF SCIENCE
IN
METALLURGICAL AND MATERIALS ENGINEERING

AUGUST 2022

Approval of the thesis:

**SYNTHESIS OF DISPERSIBLE LiFePO₄ PARTICLES WITH
CONTROLLED SIZE AND MORPHOLOGY VIA POLYOL ROUTE**

submitted by **ELİF COŞKUN** in partial fulfillment of the requirements for the degree of **Master of Science in Metallurgical and Materials Engineering, Middle East Technical University** by,

Prof. Dr. Halil Kalıpçılar
Dean, Graduate School of **Natural and Applied Sciences**

Prof. Dr. Ali Kalkanlı
Head of the Department, **Metallurgical and Materials Eng.**

Assoc. Prof. Dr. Simge Çınar Aygün
Supervisor, **Metallurgical and Materials Eng., METU**

Prof. Dr. Bora Maviş
Co-Supervisor, **Mechanical Eng., Hacettepe University**

Examining Committee Members:

Prof. Dr. Mehmet Kadri Aydınol
Metallurgical and Materials Eng., METU

Assoc. Prof. Dr. Simge Çınar Aygün
Metallurgical and Materials Eng., METU

Prof. Dr. Hüsni Emrah Ünalın
Metallurgical and Materials Eng., METU

Assoc. Prof. Dr. Emre Büküşođlu
Chemical Eng., METU

Assist. Prof. Dr. Recep Yüksel
Chemistry, Eskişehir Osmangazi University

Date: 22.08.2022

I hereby declare that all information in this document has been obtained and presented in accordance with academic rules and ethical conduct. I also declare that, as required by these rules and conduct, I have fully cited and referenced all material and results that are not original to this work.

Name Last name: Elif Coşkun

Signature:

ABSTRACT

SYNTHESIS OF DISPERSIBLE LiFePO_4 PARTICLES WITH CONTROLLED SIZE AND MORPHOLOGY VIA POLYOL ROUTE

Coşkun, Elif

Master of Science, Metallurgical and Materials Engineering

Supervisor: Assoc. Prof. Dr. Simge Çınar Aygün

Co-Supervisor: Prof. Dr. Bora Maviş

August 2022, 119 pages

Despite their widespread use in energy storage, high cost and safety are two major concerns for lithium-ion batteries (LIBs). The lack of safe, scalable, robust, and energy-efficient methods enabling high yield synthesis is one of the main reasons for the high cost of electroactive materials. This need has driven an interest in polyol synthesis technique due to simplicity and scalability. As applied in the synthesis of LiFePO_4 (LFP) nanoparticles, polyol methods have generally been performed at high temperatures. In this study, a scalable, safe, highly efficient, low temperature polyol process was developed to synthesize hierarchical, dispersible LFP nanoparticles. Unlike previous examples where high chain polyols were common solvents of choice, the use of higher polarity and lower boiling point ethylene glycol was proposed. The relationship between the amount of water in the reaction medium, the boiling point of the polyol and the solubility of the reagents used was revealed. LFP crystallization was observed at temperatures as low as 170 °C and 97% yield was attained after 9 hours of reaction at this temperature.

The morphology and size of the LFP particles are critical to enable fast diffusion of lithium ion in structure, to achieve high volumetric energy density and to eliminate the potential processing problems during electrode fabrication. In electroactive particles, while the nano-size offers faster reaction kinetics compared to larger sizes, it increases the suspension viscosity, limits the tap density, and thus decreases the volumetric energy density. The synthesis of hierarchical particles having united structure constructed from nano-units, has recently gained attention. Designing dispersible hierarchical structures leading to low suspension viscosity, high electrochemical behavior and tap density is essential. In this thesis, citric acid and ascorbic acid were used to design hierarchical sub-micrometer sized LFP particles with nano-size primary units via polyol method. The electrochemical behavior, dispersibility, tap density and suspension viscosity of the synthesized powders were investigated. Using hierarchical LFP particles leads to significantly low suspension viscosities and remarkable increase in the tap density compared to its nanosized counterparts reported in literature.

Keywords: Lithium Iron Phosphate, Scalable Synthesis of Electroactive Particles, Polyol Method, Hierarchical Particles, Suspension Rheology

ÖZ

POLİOL YÖNTEMİ İLE KONTROLLÜ BOYUT VE MORFOLOJİYE SAHİP DAĞITILABİLİR LiFePO₄ PARÇACIKLARININ SENTEZİ

Coşkun, Elif
Yüksek Lisans, Metalurji ve Malzeme Mühendisliği
Tez Yöneticisi: Assoc. Prof. Dr. Simge Çınar Aygün
Ortak Tez Yöneticisi: Prof. Dr. Bora Maviş

Ağustos 2022, 119 sayfa

Enerji depolamada yaygın kullanımlarına rağmen, yüksek maliyet ve güvenlik lityum iyon bataryalar (LIBs) için iki önemli endişe kaynağıdır. Yüksek verimli sentez sağlayan, güvenli, ölçeklendirilebilir, adapte edilebilir ve enerji verimli bir yöntemin eksikliği elektroaktif malzemelerin yüksek maliyetlerinin ana nedenlerindedir. Bu ihtiyaç, sadeliği ve ölçeklendirilebilirliği nedeniyle poliol sentez yöntemine olan ilgiyi arttırmıştır. Bununla birlikte LiFePO₄ (LFP) nanoparçacıklarının poliol sentezi yüksek sıcaklıklarda gerçekleştirilmektedir. Bu çalışmada, hiyerarşik ve dağıtılabilir LFP nanoparçacıklarını sentezlemek için ölçeklendirilebilir, güvenli, yüksek verimli, düşük sıcaklık poliol yöntemi kullanılmıştır. Sentez ortamı olarak yüksek zincirli poliollerin yaygın çözücü olarak kullanıldığı örneklerinin aksine, bu çalışmada daha yüksek polariteye ve daha düşük kaynama noktasına sahip etilen glikol kullanımı önerildi. Reaksiyon ortamındaki su miktarı, poliolün kaynama noktası ve kullanılan reaktantların çözünürlüğü arasındaki ilişki ortaya çıkarıldı. LFP kristallizasyonu 170 °C kadar düşük sıcaklıklarda gözlemlendi ve 9 saat reaksiyondan sonra %97 verim elde edildi.

LFP parçacıklarının morfolojileri ve boyutları, yapıda lityum iyonunun hızlı difüzyonunu sağlamak, yüksek hacimsel enerji yoğunluğuna erişebilmek ve elektrot üretimi sırasında ortaya çıkabilecek operasyonel sorunları ortadan kaldırmak için kritik öneme sahiptir. Elektroaktif malzemelerde nano-boyut daha büyük boyutlarla kıyaslandığında hızlı reaksiyon kinetiğini sağlarken, süspansiyon viskozitesini arttırmakta, doldurma yoğunluğunu düşürmekte ve böylece hacimsel enerji yoğunluğunu azaltmaktadır. Nano-birimlerden oluşan hiyerarşik yapıların sentezi son zamanlarda ilgi görmektedir. Düşük süspansiyon viskozitesine, yüksek elektrokimyasal davranışa ve doldurma yoğunluğuna sahip dağıtılabilir hiyerarşik yapıların tasarlanması esastır. Bu tezde, sitrik asit ve askorbik asit, poliol yöntemi ile nano-boyutlu birincil birimlere sahip hiyerarşik mikrometre-altı boyutlu LFP parçacıklarının tasarlanması için kullanılmıştır. Sentezlenen tozların elektrokimyasal davranışı, dağıtılabilirliği, doldurma yoğunluğu ve süspansiyon viskoziteleri incelenmiştir. Hiyerarşik LFP parçacıklarının kullanılması, literatürde raporlanan nano-boyutlu parçacıklara kıyasla önemli ölçüde düşük süspansiyon viskozitelerinin elde edilmesine ve doldurma yoğunluğunda önemli bir iyileşmeye yol açmıştır.

Anahtar Kelimeler: Lityum Demir Fosfat, Ölçeklendirilebilir Elektroaktif Malzeme Sentezi, Poliol Yöntemi, Hiyerarşik Parçacıklar, Süspansiyon Reolojisi

To my parents...

ACKNOWLEDGMENTS

I owe my sincere thanks to my advisor Dr. Simg'e Çınar Aygün for her patience, guidance and endless support. She always shares her experience and knowledge with me. It would be impossible to complete my thesis without her guidance.

I would like to thank to my co-advisor Prof. Dr. Bora Maviş. It was a real privilege and honor for me to share of his scientific knowledge.

I also would like to thank Prof. Dr. Caner Durucan, Prof. Dr. Mehmet Kadri Aydınol and Dr. Zeynep Çulfaz Emecen. Their doors were always open to me whenever I needed to use laboratory facilities.

It was my pleasure to work with my laboratory colleagues Bayram Yıldız, Yasemin Aşkar, Orçun Dinçer, Mert Ulusel, Emre Altın, Mustafa Utku Yıldırım, Ekin Kurşun, Doğu Şeyda, Burak Cengiz, Duygu İnce, Mert Oral and İbrahim Egemen Küçük.

This work was supported by Middle East Technical University, Scientific Research Projects under grant number TEZ-YL-308-2022-10866, GAP-308-2022-10858 and HDESP-308-2021-10814.

I would like to thank also to Görkem Yasin Ak, Mustafa Caner Görür, Burak Çamlođlu, Volkan Ertaş, Atalay Balta, Uzay Anıl Bilgin, Doğucan Bakkalbaşı, Uđur Aydođan, Begüm Erdem and Mehmet Demirođlu for their friendship.

I am grateful to my parents, Nazmiye Coşkun and Hüseyin Çelik Coşkun, for their endless love, support, and patience. I am so lucky to have you in my life.

TABLE OF CONTENTS

ABSTRACT.....	v
ÖZ	vii
ACKNOWLEDGMENTS	x
TABLE OF CONTENTS	xi
LIST OF TABLES	xiv
LIST OF FIGURES	xv
CHAPTERS	
1 INTRODUCTION	1
2 LITERATURE REVIEW	3
2.1 Lithium-Ion Batteries	3
2.2 Lithium Based Cathode Materials.....	6
2.3 Cathode Material Synthesis Methods.....	6
2.3.1 Polyol Method for Nanomaterial Synthesis	7
2.3.2 The Reaction Medium in Polyol Synthesis.....	7
2.3.3 Ethylene Glycol in Polyol Synthesis.....	8
2.3.4 Polyol Synthesis for LiFePO ₄	9
2.4 Importance of Reagent Solubility for Nucleation and Growth of Nanomaterials	13
2.5 Importance of Physical Properties of LiFePO ₄ on Electrochemical Behavior, Tap Density and Viscosity	13
2.5.1 Importance of Particle Size	14
2.5.2 Importance of Particle Shape	15

2.5.3	Importance of Dispersibility	19
2.6	The Control Over the Size and Shape of LiFePO ₄ using Ascorbic Acid or Citric Acid	21
2.7	Hierarchical LiFePO ₄ Particles	26
2.8	Objective of This Thesis	29
3	EXPERIMENTAL DETAILS	31
3.1	Materials	31
3.2	Experimental Methods	32
3.2.1	Preparation of Reagents	32
3.2.2	Synthesis of LiFePO ₄ Particles.....	33
3.2.3	Synthesis of LiFePO ₄ Particles with Acid Addition.....	35
3.2.4	Combined Addition of Citric Acid and Ascorbic Acid	35
3.2.5	Post-Processes of LiFePO ₄ Particles	37
3.2.5.1	Washing and Drying Procedures	37
3.2.5.2	Heat Treatment Procedures	37
3.3	Particle Characterization	39
3.3.1	Electrochemical Behavior.....	41
3.3.2	Rheology Measurements	42
4	POLYOL SYNTHESIS OF LiFePO ₄	45
5	THE INFLUENCE OF POST-PROCESSING TREATMENTS ON THE DISPERSIBILITY AND PURITY OF LiFePO ₄	53
5.1	Effects of Heat Treatment.....	53
5.2	Effect of Washing Procedure Applied After Synthesis on the Particle Dispersion.....	57

5.3	Effect of Exchange by More Strongly Coordinating Agents on Dispersion	58
6	THE SYNTHESIS OF HIERARCHICAL LiFePO_4 PARTICLES WITH CONTROLLED SIZE AND SHAPE	65
6.1	Addition of Ascorbic Acid	65
6.2	Addition of Citric Acid.....	71
6.3	Combined Addition of Ascorbic Acid and Citric Acid.....	73
6.4	Effects of Citric Acid Concentration.....	80
6.5	Addition Sequence of Citric Acid During Precursor Preparation	85
7	CONCLUSIONS.....	89
	REFERENCES	93
	APPENDICES	
A.	BOILING POINT OF REACTION MEDIUM AND YIELD CALCULATIONS	109
B.	HEATING PROFILE OF PRECURSOR SUSPENSION IN THE HEATING MANTLE	111
C.	CALCULATIONS OF EXPERIMENTS WITH ORGANIC ACID ADDITION	112
D.	ATR-FTIR DECONVOLUTION WITH FITYK-CURVE FITTING AND PEAK FITTING SOFTWARE	113
E.	PARTICLE SIZE ANALYSIS USING IMAGE J SOFTWARE	115
F.	COMPARISON OF ORGANIC AND AQUEOUS ELECTROLYTE .	119

LIST OF TABLES

TABLES

Table 2.1 Summary of reaction conditions reported for the LiFePO_4 synthesis via polyol route.....	11
Table 2.2 The reagents used for LiFePO_4 synthesis via polyol route reported in the literature.....	12
Table 2.3 Tap densities of hierarchical structures reported in the literature.....	28
Table 3.1 Experimental details of ascorbic acid and/or citric acid addition.....	36
Table 3.2 Experimental details of feeding sequences and citric acid amounts.	36
Table 4.1 pH values of the samples taken from the reaction medium.....	46
Table 6.1 Properties of synthesized LiFePO_4 particles in this thesis	88
Table A.1 Experimental details of LiFePO_4 synthesis without organic acid addition.	109

LIST OF FIGURES

FIGURES

Figure 1.1. The relationship between components of material science and electroactive materials.....	2
Figure 2.1. Schematic representation of lithium-ion batteries	4
Figure 2.2. Schematic representation of suspension flow batteries	5
Figure 2.3. The chemical structure of ethylene glycol.....	9
Figure 2.4. The relationship between particle size and viscosity. (a) The relationship between the particle size and the number of particles in the same volume. (b) The relationship between the particle size and the rheological behavior of suspensions with same particle loading.	15
Figure 2.5. (a) Lithium-ion transfer paths in the LiFePO_4 unit cell ⁷⁵ . (b) The schematic representation of the morphology of (010) exposed LiFePO_4 particles ⁷⁶ . (c) The LiFePO_4 particles in plate-like morphology.....	16
Figure 2.6. The FE-SEM micrograph of LiFePO_4 (a) nanoparticles, (b) nanorods, and (c) nanoplates. (d) The change of the specific discharge capacities according to the particle shape and the current rate.	17
Figure 2.7. (a) The effect of particle anisotropy on the packing density. The packing density increases as the aspect ratio of the particles approaches 1 (as anisotropy decreases). Packing of ellipsoid shape (b) and (c) spherical shape particles. The packing of ellipsoid shape is denser than the one of spherical shape. (d) The effect of particle anisotropy on the suspension viscosity as a function of particle loading.	19
Figure 2.8. Dry and liquid states of particles	20
Figure 2.9. Pechini sol-gel method (a) Chemical structure of a citric acid and polyethylene glycol molecules. (b) Complexation reaction between citric acid and metal ions. (c) Polymerization reactions between citric acid, ethylene glycol and metal-citrate complexes	22
Figure 2.10. The chemical structure of ascorbic acid.	23

Figure 2.11. The changes in LiFePO ₄ morphology with acidity of reaction medium	24
Figure 2.12. X-ray diffraction pattern and FE-SEM micrograph of synthesized LiFePO ₄ particles showing the change of the crystallographic planes by addition of ascorbic acid (AA), citric acid (CA) and polyethylene glycol (PEG)	25
Figure 2.13. Examples of hierarchical LiFePO ₄ particles (a) Spherical structure formed by dense compact nanoplates. (b) Sphere-shaped made of tightly cohered sheets. (c) Microflowers which consist of rectangular nanoplates. (d) Mesoporous spindle-like particles. (e) Bow-shaped particles consisted of platelet subunits. (f) Microspheres made of nanograins	28
Figure 3.1. Characterization of the reference LiFePO ₄ /C particles. (a) FE-SEM micrograph. (b-c) Particle size measurements using laser diffraction. (b) Number-weighted and (c) volume-weighted size distribution of particles.....	32
Figure 3.2. The photographs of (a) LiOH and (b) FeSO ₄ precursors at the end of dispersion process.....	33
Figure 3.3. Schematic representation of LiFePO ₄ synthesis.	34
Figure 3.4. The photographs of the mixtures of (a) FeSO ₄ and H ₃ PO ₄ precursors (Step 2), and (b) FeSO ₄ , H ₃ PO ₄ and LiOH precursors (Step 3).	35
Figure 3.5. Heat treatments applied to synthesized LiFePO ₄ particles.	39
Figure 3.6. The 3-electrode system used for measurements in aqueous electrolyte.	42
Figure 4.1. Crystallinity, color and morphology change of synthesized LiFePO ₄ particles with reaction temperature and duration. (a) The color changes of the reaction medium. (b) The X-ray diffraction patterns. The FE-SEM micrographs of (c) 35 °C, (d) 120 °C, (e) 150 °C, (f) 170 °C, (g) 170 °C after 15 min., (h) 170 °C after 9 h. For (c), (d) and (e), the inset scales are 1 μm and the outer scales are 1 μm. For (f), (g) and (h), the inset scales are 500 nm, and the outer scales are 1 μm.	48
Figure 4.2. Characterization of LiFePO ₄ particles synthesized at 170 °C for 9 h. (a) The FE-SEM micrograph. The HR-TEM nanographs at (b) relatively low and (c)	

relatively high magnifications. (d) ATR-FTIR spectrum in the wavenumber range of 1800-400 cm^{-1} . (e) The specific discharge capacities at a current rate 0.1 C 50

Figure 5.1. The characterization of powders exposed to Heat Treatment Procedure 1. (a) The X-ray diffraction patterns and the color of powders before and after the heat treatment. The dispersion characteristics of powders in DIW (b) before and (c) after the heat treatment. (d) The FE-SEM micrographs of particles after HT₁. The arrows on the inset figure show the interparticle necks. Inset scale is 500 nm. 54

Figure 5.2. Characterization of LFP particles exposed to Heat Treatment Procedure 2. (a) The X-ray diffraction patterns and dispersibility of particles in DIW before and after the heat treatment. (b) The FE-SEM micrographs of the heat-treated powders. The inset figure (the scale bar is 1 μm) shows the particles on the surface of the agglomerate. (c) The HR-TEM nanographs of the heat-treated sample. 56

Figure 5.3. Characterization of LFP particles exposed to Heat Treatment Procedure 3. (a) FE-SEM micrographs of the heat-treated particles. Dispersibility of particles (b) before and (c) after the heat treatment. 57

Figure 5.4. The effects of the washing procedure W₂. (a) The ATR-FTIR spectrum of the particles washed with W₂ (b) Dispersibility of the particles in DIW after washing with W₂ and heat treatment of the HT₂. 58

Figure 5.5. The characterization of Sample H before and after exposed to the Heat Treatment Procedure 1. (a) The X-ray diffraction patterns and dispersibility of particles. (b) The FE-SEM micrographs of the Sample H_HT₁. 59

Figure 5.6. The characterization of Sample H before and after exposed to Heat Treatment Procedure 2. (a) The X-ray diffraction patterns and dispersibility in DIW. (b) The FE-SEM micrographs of Sample H (b) before and (c) after the heat treatment. The inset scales are 300 nm. 61

Figure 5.7. The ATR-FTIR spectra of the powders (a) before and (b) after the heat treatments. In both plots, the powders synthesized with and without use of acids were compared. 63

Figure 6.1. Effects of ascorbic acid addition on the LiFePO_4 particles. (a) The X-ray diffraction patterns, and the FE-SEM micrographs of particles synthesized (b) in the absence and (c) presence of the ascorbic acid. The inset scales are 200 nm. 67

Figure 6.2. Comparison of the sedimentation behavior and the particle dimensions of synthesized particles with and without use of ascorbic acid. * shows measured primary size from the SEM micrographs using ImageJ software. 200 – 250 particles were measured for each sample. For the secondary particle size measurements, about 3000 particles were measured. ** shows the size measurements obtained using Scherrer equation. 68

Figure 6.3. Tap densities of 170 °C 9 h. (large fusiforms), A (small fusiforms) and reference powders. Tap density of synthesized particles was higher than the reference powder. 69

Figure 6.4. (a) Rheological behavior of the synthesized and the reference powders. Images showing the flow behavior of (b) of Sample A, (c) Sample 170 °C 9 h, and (c) the reference powder. 71

Figure 6.5. Effects of using citric acid during LiFePO_4 synthesis. (a) X-ray diffraction pattern and the (b) FE-SEM micrographs of Sample B. 72

Figure 6.6. Effect of combined addition of citric acid and ascorbic acid to the reaction medium during synthesis of LiFePO_4 . For Sample C, ascorbic acid was added with citric acid while for Sample D, it was added 15 minutes after the reaction temperature reached to 170 °C. (a) X-ray diffraction patterns and FE-SEM micrographs (b) of Sample C and Sample D. The inset scales are 300 nm. 75

Figure 6.7. Comparison of the sedimentation behavior and the particle dimensions of synthesized particles with combined addition of ascorbic acid and citric acid. * shows measured primary size from the SEM micrographs using ImageJ software. 200 – 300 particles were measured for each sample. For the secondary particle size measurements, about 3000 particles were measured. ** shows the size measurements obtained using Scherrer equation. 76

Figure 6.8. The tap density comparison of the Sample C, the Sample D and the reference powder.....	77
Figure 6.9. (a) The rheological behavior of the suspensions prepared from synthesized (Sample C and Sample D) and the reference powders. Images showing the flow behavior of (b) the Sample C, the Sample D, and the reference powder suspensions.	78
Figure 6.10. Effect of Heat Treatment Procedure 2 on Sample D. (a) The X-ray diffraction patterns, (b) The specific discharge capacities in 3-electrode aqueous setup of Samples D and Sample D_HT ₂ . (c) The FE-SEM micrograph of D_HT ₂ .	80
Figure 6.11. The effect of doubled citric acid concentration on the synthesized particle characteristics. (a) The X-ray diffraction patterns, (b) FE-SEM micrographs, and (c) The sedimentation behavior and particle size measurements of Sample E. Inset scale of FE-SEM micrograph is 300 nm. * shows measured primary size from the SEM micrographs using ImageJ software. 200 particles were measured for Sample E. ** shows the crystallite sizes obtained by application of Scherrer equation. 3000 particles were measured for secondary particle size of both samples.....	82
Figure 6.12. Tap density comparison of the Sample C, the Sample D and the reference powder.....	83
Figure 6.13. (a) The rheological behavior of aqueous suspensions of Sample D, Sample E and their comparison with the one of the reference powders. The images showing the flow behavior of the suspensions prepared from (b) the Sample D, (c) the Sample E, and (c) the reference powder.	84
Figure 6.14. The effect of feeding sequence of citric acid on the synthesized particle characteristics. (a) The X-ray diffraction patterns and the FE-SEM micrograph of (b) the Sample D, (c) the Sample F, (d) the Sample G, and (e) the Sample H. The inset scales are 500 nm.	86
Figure 6.15. The tap densities of the samples D, F, G, H, and the reference powder.	87
Figure B.1. Heating profile of precursor suspension in the heating mantle.....	111

Figure D.1. Deconvolution of ATR-FTIR spectra in the wavenumber range of 1230-800 cm^{-1} for (a) Sample 170 °C 9 h. (b) Sample H. The arrows on the figure show the peaks indicating the anti-site defects 113

Figure D.2. Deconvolution of ATR-FTIR spectra in the wavenumber range of 1750-1500 cm^{-1} for (a) Sample 170 °C 9 h. (b) Sample H..... 114

Figure E.1. An example for the average size calculation of Sample 170 °C 9 h. (a) Measurement of secondary particles. (b) Measurement of primary particles 115

Figure E.2. An example for the average size calculation of Sample A (a) Measurement of secondary particles. (b) Measurement of primary particles 115

Figure E.3. An example for the average size calculation of Sample C. (a) Measurement of length of secondary particles. (b) Measurement of width of secondary particles. (c) Measurement of length of primary particles. (d) Measurement of width of primary particles. 116

Figure E.4. An example for the average size calculation of Sample D (a) Measurement of length of secondary particles. (b) Measurement of width of secondary particles. (c) Measurement of primary particles..... 116

Figure E.5. An example for the average size calculation of Sample E (a) Measurement of length of secondary particles. (b) Measurement of width of secondary particles. (c) Measurement of primary particles..... 117

Figure E.6. An example for the average size calculation of Sample F (a) Measurement of length of secondary particles. (b) Measurement of width of secondary particles. (c) Measurement of primary particles..... 117

Figure E.7. An example for the average size calculation of Sample G (a) Measurement of length of secondary particles. (b) Measurement of width of secondary particles. (c) Measurement of primary particles..... 117

Figure E.8. An example for the average size calculation of Sample H (a) Measurement of length of secondary particles. (b) Measurement of width of secondary particles. (c) Measurement of primary particles. 118

Figure F.1. Specific discharge capacities of 170 °C 9 h. in half cell setup with organic electrolyte and 3-electrode vial cell setup with aqueous electrolyte.....119

CHAPTER 1

INTRODUCTION

Even though lithium-ion batteries are being used extensively throughout the world, electroactive material synthesis methods and the design of electroactive materials still require improvement¹. The need for safe and cost-efficient electroactive material synthesis becomes more critical as the use of LIBs increases.

Designing the physical properties of LFP electroactive material is critical for achieving high volumetric energy density, cost and energy efficient operation and processing. The high specific discharge capacity attracts attention for nano-sized and plate-shaped LFP particles because of easier lithium ion transfer, while low tap density and high suspension viscosity of these particles reduce the volumetric energy density and cause operational and processing difficulties². The answers to these problems in synthesis method and electroactive material design can be found in the process, performance, property, and structure components of material science. Using the simple and scalable polyol route, size, morphology and dispersibility of the synthesized particles can be designed, hierarchical structures can be obtained and the rheological behavior, tap density and electrochemical behavior of the particles can be improved as illustrated based on the materials science paradigm in Figure 1.1.

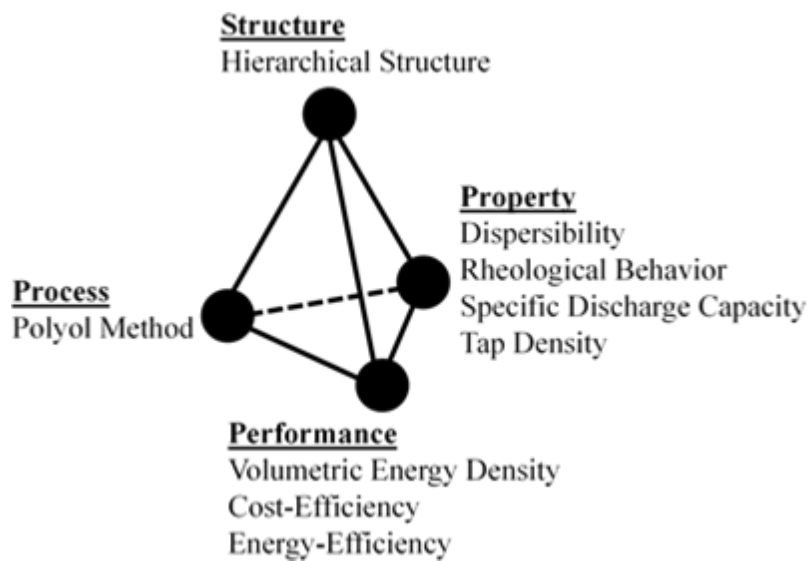


Figure 1.1. The relationship between components of material science and electroactive materials.

The main purpose of this study is to design and synthesize hierarchical LiFePO_4 (LFP) electroactive materials by the polyol route at low temperature and high yield. Electroactive material synthesis methods, design of LFP particles and design strategies in literature are reviewed in Chapter 2. In Chapter 3, the experimental procedure followed in this thesis is reported. The synthesis of LFP particles by the polyol route is described in Chapter 4 and the post-processing treatments affecting the dispersibility and purity of the synthesized particles are presented in Chapter 5. In Chapter 6, the control over the size and morphology of the hierarchical particles is demonstrated.

CHAPTER 2

LITERATURE REVIEW

Lithium-ion batteries, cathode materials and their synthesis techniques are covered in the first part of this chapter. The studies on the polyol process for the synthesis of lithium iron phosphate (LiFePO_4 , LFP) cathode material are reviewed and the importance of dissolution of reagents for the nanomaterial synthesis is emphasized. Hierarchical LFP structures are also introduced, along with a description of how the physical characteristics of the LFP (its size, shape, and dispersibility) affect the tap density, suspension viscosity, and specific discharge capacity. The hierarchical LFP structures and influence of ascorbic acid and citric acid additives on the morphology of the particles are discussed and the chapter is concluded with the objective of this thesis.

2.1 Lithium-Ion Batteries

The need for improved energy storage systems is increasing globally as a result of the growing demand for clean and sustainable energy, intermittent energy sources and that drives the advances in batteries. Only the global electric vehicle (EV) fleet itself exceeded 5.1 million vehicles in 2018 and it is expected that EVs will have a market share of 86% by 2060³.

The battery offers chemical energy storage that can be delivered as portable electrical energy with a high conversion efficiency and no gaseous emissions. A cheap, secure, rechargeable (secondary) battery with high voltage, capacity, and rate capability is still of particular interest⁴. Gravimetric energy density, long cycle life and environmental friendliness of lithium-ion batteries have enabled its worldwide use⁵.

Schematic representation of a typical lithium-ion battery (LIB) is presented in Figure 2.1. The three functional parts of a LIB are the anode, cathode, and electrolyte. Anode and cathode materials are the sites of the redox reactions. For LIB's, the anode serves as the source and the cathode as the sink of Li^+ ions. The most typical anode materials used in industrial LIBs are carbon-based materials⁶. Li^+ ion transfer from anode to cathode is enabled by an electrolyte. The electrolytes used in LIBs can be classified as organic-solvent-based, ionic-liquid-based, polymer-based, and concentrated electrolytes. The conventional electrolyte used is 1 M lithium hexafluorophosphate (LiPF_6) in ethylene carbonate (EC) / dimethyl carbonate (DMC) (1:1)⁷.

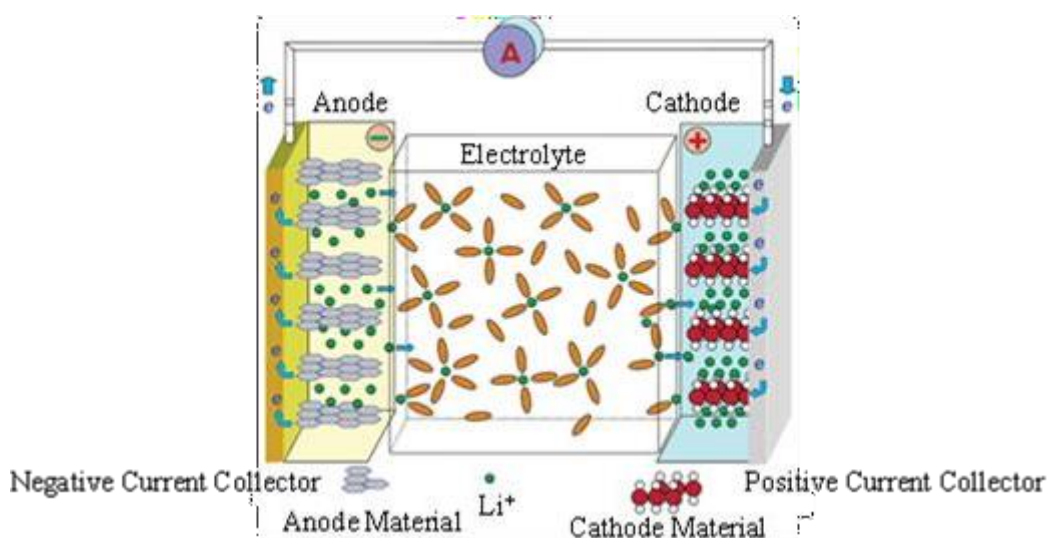


Figure 2.1. Schematic representation of lithium-ion batteries⁸.

For large-scale energy storage, flow battery systems with electroactive materials based on lithium have recently been investigated^{9,10}. Although the most widely studied flow battery systems are redox flow batteries, the limited solubility of the electroactive materials in the electrolyte reduces the obtained energy density. For example, the energy density of vanadium, the reference electroactive material for redox flow batteries, is about one-fourth of the LIBs¹¹. The concept of suspension flow battery, in which electroactive materials are suspended in electrolyte, was

proposed to overcome the low energy density caused by the solubility limit¹². Figure 2.2 describes the suspension flow batteries. Unlike typical LIBs, in flow battery systems, the anode and cathode materials are circulated within the battery cells while storing them in separate tanks. This design allows for the separation of the energy and power units, quick system scaling, and low investment costs^{13–15}. Organic electrolytes are known to harm the environment and raise CO₂ emissions. This is why aqueous electrolytes are essential for large-scale energy storage systems for factors such as sustainability, safety, and environmental responsibility¹⁶. The absence of solubility restrictions in suspension flow batteries also allows the use of reliable and economical aqueous electrolyte systems. Aqueous electrolyte has been the subject of studies and further research is ongoing¹⁷.

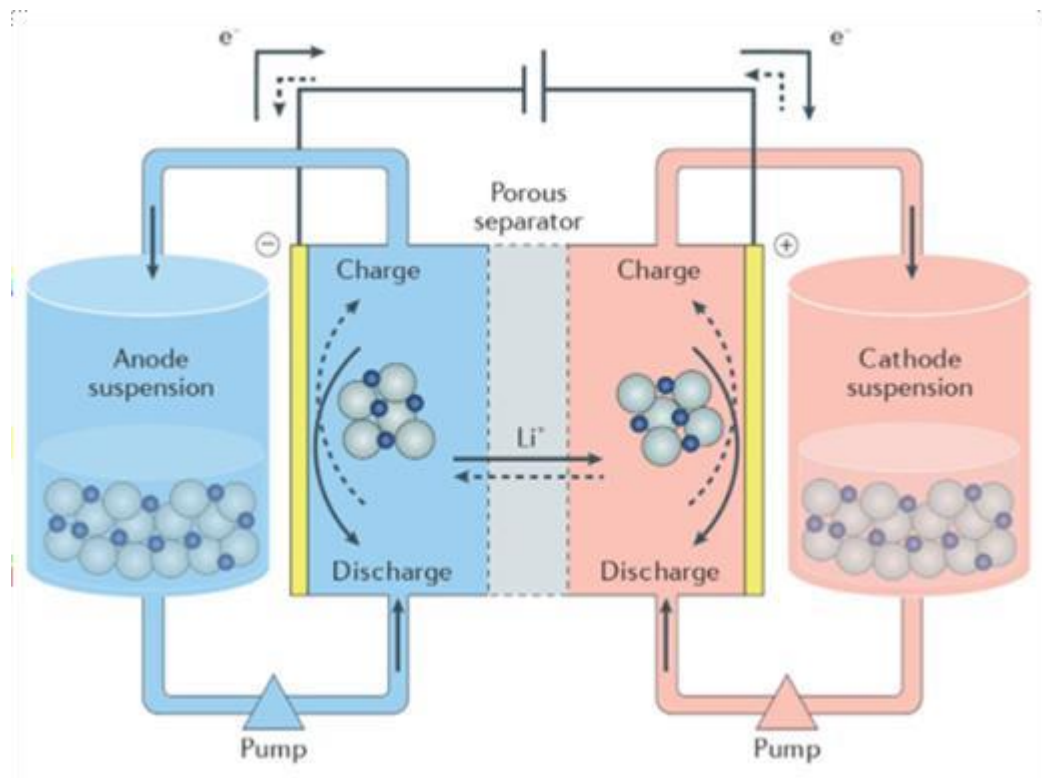


Figure 2.2. Schematic representation of suspension flow batteries⁹.

2.2 Lithium Based Cathode Materials

When the currently used and promising Li-based cathode materials are examined, four main groups attract attention: Lithium Cobalt Oxide (LiCoO_2 , LCO), Lithium Manganese Oxide (LiMn_2O_4 , LMO/Spinel), LiMPO_4 (M=Mn, Fe, Co, and their combinations), Lithium mixed Nickel-Manganese-Cobalt Oxide ($\text{LiNi}_{1-y-z}\text{Mn}_y\text{Co}_z\text{O}_2$ (NMC)¹⁸. Among the promising candidates for the cathodes of LIBs, LiFePO_4 (LFP) is one of the well-studied and commercialized member of the family of olivine-type lithium transition metal phosphates. LFP stands out due to its high theoretical capacity (170 mAh g^{-1}), high voltage plateau (3.45 V vs Li^+/Li), stability, safety, nontoxicity and relative low cost among other Li-based cathode materials.¹⁹⁻²¹.

2.3 Cathode Material Synthesis Methods

The reference LIBs are currently 5 - 10 times more expensive than the cost target. Dramatic market growth is exposed by the challenges for cost reduction and scalability²². To face these challenges, the electroactive material synthesis methods used in LIBs have been significantly diverse and involve freeze drying, sol-gel, template-directed synthesis, solvothermal/hydrothermal, supercritical fluid synthesis, mechanical activation, ionothermal method, biosynthesis, coprecipitation methods, and solid-state methods^{23,24}. Among variety of methods used for the synthesis of Li-based electroactive materials, the solid-state method is common²⁵. However, inhomogeneity, uncontrollable particle growth and agglomeration are among the problems of this synthesis method²⁶. These problems are attempted to be solved by solution-based methods²⁷. Environmentally friendly and cost-efficient water (H_2O) stands out among other solvents thanks to its high polarity. In aqueous environments, inorganic salts can efficiently be dissolved and morphology and composition control can be achieved²⁸. However, because of its low boiling point, the barrier against crystallization may not be overcome and crystallization cannot be

achieved during the reaction. Therefore, a calcination step is generally required for better crystallization. On the other hand, a calcination step may cause the formation of agglomerates or aggregates^{29,30}. It is possible to reach high temperatures at high pressures using the hydrothermal method, and a higher level of crystallization can be obtained without the need for an additional calcination step. Nevertheless, hydrothermal method requires complex reactor designs for efficient mixing under pressure, high investment costs for precise control of the reaction temperature and safety. In addition, it necessitates the use of reaction vessel construction materials that are resistant towards the potentially corrosive reaction medium intended to be used^{31,32}.

2.3.1 Polyol Method for Nanomaterial Synthesis

Although higher levels of crystallization require additional calcination steps or complex reactor designs when solution-based techniques are used, it can be achieved under atmospheric pressure without the need for calcination using high chain polyols having high boiling points. Furthermore, dispersible particle synthesis without a secondary phase formation is possible since polyols also act as reducing and capping agents³³. Since the reaction medium can reach higher temperatures without pressurizing the vessel, synthesis can be performed in a safe way. With this simpler reactor design, effective mixing of the reaction medium and a precise temperature control is facilitated^{34,35}. However, inorganic salt solubilities in high chain polyols are low. This often necessitates the use of reagents with higher costs to reach high solid yields³⁶.

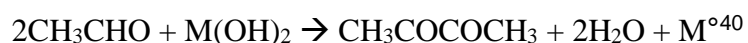
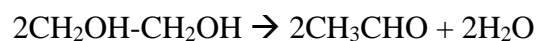
2.3.2 The Reaction Medium in Polyol Synthesis

High chain polyols (diethylene glycol (DEG), triethylene glycol (TEG) and tetraethylene glycol (TtEG)) are commonly used reaction mediums to reach high temperatures for nanomaterial synthesis³³. Also, the solid yield can be lower at

higher temperatures due to increased solubility of the nanomaterial precipitates at these temperatures. In terms of precipitation reaction efficiency, lower temperatures are preferable. Reaction yield is also related to the solubility of reactant reagents in the polyol³³. Since the polarities of the high chain polyols are lower than the low chain polyols (normalized empirical solvent polarities are 0.790, 0.713, 0.682 and 0.664 for ethylene glycol (EG), DEG, TEG and TtEG, respectively³⁷), EG's ability to dissolve inorganic salts is more than that of high chain polyols. In addition, it is important that EG reduces metals more effectively than other polyols³⁸. Also, since the viscosity of EG is lower than that of high-chain polyols (16.9, 35.7, 49.0 and 58.3 mPa.s at 25 °C for EG, DEG, TEG and TtEG, respectively³⁹), it is expected that it would be easier to mix the reaction medium. This fact, in turn, will result in higher mobility and the reactivities of the ions involved in the formation of the final product because of the higher collision probability of the species in the reaction medium.

2.3.3 Ethylene Glycol in Polyol Synthesis

EG is used as a reaction medium mostly for the synthesis of metal nanoparticles. The general mechanism of the metal particle synthesis includes dissolution of the metal salts to metal ions in the EG medium, reduction of metal ions by EG and growth of metal nanoparticles. Reduction of metal ions by oxidation of the EG occurs in two steps. In the first step, acetaldehyde (CH₃CHO) is released with dehydration of the EG (CH₂OH-CH₂OH) and the acetaldehyde is oxidized with formation of diacetyl (CH₃COCOCH₃) in the second step. In this second step, the reduction of metallic ion also takes place to form the metal particle (M⁰).



The oxidation of EG to reduce metal ions is the key point for the synthesis of metal nanoparticles. However, for the polyol synthesis of metal oxides, the dissolution of

the reagents in the polyol medium is more critical as it provides free ions to the reaction medium and allows the reaction medium to reach supersaturation. Only then, the thermodynamic requirements for metal oxide particle precipitation can be met⁴¹. Because of the higher polarity of EG compared to other polyols, reagents are more soluble in EG which makes the metal oxide synthesis more feasible.

There have been studies that report metal oxide synthesis using EG as the reaction medium. In a selection of these studies, hierarchical structures can be formed, EG concentration being a strong determinant of the structure⁴²⁻⁴⁴. However, the structure formation was generally associated with OH groups of EG (Figure 2.3) and the complexes formed between the metal ions and EG molecules⁴⁴. The mechanism of the hierarchical structure formation has not been completely revealed yet and requires more effort³³. Nevertheless, the effect of EG oxidation is expected to be less pronounced in metal oxide synthesis.

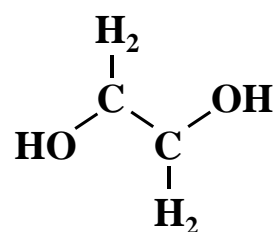


Figure 2.3. The chemical structure of ethylene glycol.

2.3.4 Polyol Synthesis for LiFePO₄

There are considerable number of studies reporting the LFP particle synthesis using the polyol method (Table 2.1 and Table 2.2). In these studies, high chain polyols (DEG, TEG and TtEG) are mostly used as reaction medium to reach high synthesis temperatures as shown in Table 2.1. All of these polyols, except for one specific case, have long carbon chain. In this one specific study, LFP particles were synthesized using EG, however the electrochemical behavior of the synthesized LFP particles was not reported. When studies conducted using high-chain polyols are

examined, it can be noted exact synthesis conditions were rarely described. In some studies, it was claimed that synthesis was carried out at temperatures higher than the reaction medium's known boiling point. It is not clear how these temperatures were reached (i.e., possibly due to an increase in the boiling point with dissolution of the reactants in the initial precursor) or whether the reaction medium temperature was measured at all. In addition, the relationship between the initial molarities of the reagents and the water contribution from them, and the final boiling point of the reaction medium have been overlooked. The amount of crystal water in the raw materials and, if it was used, the water from the phosphoric acid source needs to be accounted for with a rigorous stoichiometric analysis, because the water amount can reach significantly high levels and considerably lower the boiling point of the polyol used. This effect seems to be completely ignored in the polyol based LFP synthesis work found in the literature.

The reagents used for LFP synthesis, and the methods used for their dissolution are shown in Table 2.2. The extensive use of acetates, which are more expensive than inorganic salts, is noteworthy. Although reagent solubility is effective on the nucleation-growth of nanomaterials and particle morphology, reported information on the solubility of reagents is limited.

Table 2.1 Summary of reaction conditions reported for the LiFePO₄ synthesis via polyol route

Polyol	Reaction Conditions	Calcination Conditions	Reference
DEG	245 °C 18 h.	500 °C 1 h. under Ar for NiO coating	45
TEG	280 °C 4, 10, 16 h.	700 °C 4 h. under N ₂ for carbon coating	46
TtEG	335 °C 16 h.	No	47
TEG	240 °C 14 h.	600 °C 10 h. under Ar/N ₂ (95:5) for carbon addition	48
TEG	335 °C 12 h.	No	49
DEG	245 °C 18 h.	700 °C 2 h. under Ar/N ₂ (95:5) for carbon coating	50
TtEG	320 °C 1, 4, 8, 16, 32 h.	No	51
TEG	~270 °C 18 h.	No	52
DEG, TEG, TtEG	Under ebullition 4 h.	700 °C 1 h. under N ₂ for carbon coating	53
TEG	240 °C 18 h.	No	54
TtEG	320 °C 4 h.	No	55
TEG	295 °C 5 h.	650 °C 1 h. under N ₂ for carbon composite	56
TEG	~260 °C 18 h.	700 °C 2 h. under Ar for carbon addition	57
TtEG	320 °C 16 h.	No	58
EG	180 °C 6 h.	No	59
TtEG	200 °C 1.5 h. and 260 °C 3 h.	No	60

Table 2.2 The reagents used for LiFePO₄ synthesis via polyol route reported in the literature

Li ⁺ Reagent	PO ₄ ³⁻ Reagent	Fe ²⁺ Reagent	Dissolution of Reagents	Reference
LiH ₂ PO ₄	LiH ₂ PO ₄	FeSO ₄ ·7H ₂ O	Yes*	45
LiOH·H ₂ O	FePO ₄ ·2H ₂ O	FePO ₄ ·2H ₂ O	Milling in an agate jar for 4 h.	46
LiCH ₃ COO	NH ₄ H ₂ PO ₄	Fe(CH ₃ COO) ₂	No	47
LiCH ₃ COO ₂ ·H ₂ O	NH ₄ H ₂ PO ₄	FeCl ₂ ·4H ₂ O	Vigorous agitation and ultrasonication	48
LiOH·2H ₂ O	FePO ₄ ·2H ₂ O	FePO ₄ ·2H ₂ O	Yes*	49
LiH ₂ PO ₄	LiH ₂ PO ₄	Fe(NO ₃) ₃	No	50
LiCH ₃ COO	H ₃ PO ₄	Fe(OH)(CH ₃ COO) ₂	Yes*	51
LiCH ₃ COO ₂ ·2H ₂ O	NH ₄ H ₂ PO ₄	Fe(CH ₃ COO) ₂ ·4H ₂ O	Mechanical agitation for 30 min. at RT**	52
Li(CH ₃ CO ₂) ₂ ·2H ₂ O	H ₃ PO ₄	Fe(CH ₃ CO ₂) ₂	No	53
LiCH ₃ COO·2H ₂ O	NH ₄ H ₂ PO ₄	Fe(CH ₃ COO) ₂ ·2H ₂ O	Mechanical agitation for 30 min. at RT**	54
Li(CH ₃ COO)	NH ₄ H ₂ PO ₄	Fe(CH ₃ COO) ₂	Yes*	55
LiOH·H ₂ O	Fe ₃ (PO ₄) ₂ ·8H ₂ O and H ₃ PO ₄	Fe ₃ (PO ₄) ₂ ·8H ₂ O	No	56
LiCH ₃ COO·2H ₂ O	NH ₄ H ₂ PO ₄	Fe(CH ₃ COO) ₂ ·4H ₂ O	Under magnetic stirring at RT**	57
Li(CH ₃ COO)	NH ₄ H ₂ PO ₄	Fe(CH ₃ COO) ₂	No	58
LiOH·H ₂ O	H ₃ PO ₄	FeSO ₄ ·7H ₂ O	Under magnetic stirring	59
LiCO ₃	H ₃ PO ₄	Fe(C ₅ H ₇ O ₂) ₃	No	60

*The information reported for the dissolution of reagents is limited. ** RT: Room Temperature

2.4 Importance of Reagent Solubility for Nucleation and Growth of Nanomaterials

Two strategies, the top-down and the bottom-up, are techniques being used for synthesizing nanomaterials. Bulk materials are transformed into nano-sized particles using the top-down approach, but it can be challenging to control the particle size, particle size distribution and particle shape. In the bottom-up approach, atoms are assembled to nucleate particles with clearly defined size and shape⁶¹. When theories for the nucleation and growth of bottom-up synthesis are investigated, classical and non-classical theories can be seen. In both theories, it is seen that Gibbs free energy is a strong function of supersaturation for the transformation, which creates the driving force for nucleation and growth. For instance, it has been determined that supersaturation is the primary influence on the nucleation rate based on the classical nucleation theory. The nucleation rate increased by 10^{70} when the supersaturation was doubled⁶². It is essential that all the solid reagents are dissolved into ions to build up the necessary supersaturation levels for nucleation.

Reagent dissolution is also a critical factor in the analysis of the value of activation energy required for nucleation⁶³. Nucleation can take place on a preexisting surface with a smaller barrier against nucleation (heterogeneous nucleation). If undissolved reagents are present in the initial stages of synthesis, this can lead to uncontrolled heterogeneous nucleation in the solution causing irregularities in particle morphologies and/or aggregations⁶⁴.

2.5 Importance of Physical Properties of LiFePO₄ on Electrochemical Behavior, Tap Density and Viscosity

In this section, size, shape and dispersibility of LFP particles, the three main physical characteristics of particles known to be affecting the volumetric energy density and cost-efficient processing and operation, were reviewed.

2.5.1 Importance of Particle Size

For electroactive materials, as the particles size decreases, the diffusion path of ions and electrons shortens, the charge-discharge reactions become faster and the specific discharge values tend to increase towards theoretical values. As particle size increases, paths for diffusion of Li^+ become longer. While Li^+ delithiation is 0.01 s for nano-sized defect-free LFP particles, this time is 1 s for micrometer-sized particles which means much weaker conductivity⁶⁵. In the study of Nan et al., the first discharge capacity of the LFP particle with lithium-ion transfer path of 35 nm was found to be 169 mAh/g at a current density of 0.05 C, while the same with a path of 70 nm is 115 mAh/g under the same conditions⁶⁶. Additionally, because small particles have a higher surface area to volume ratio, more ions can transfer between the electrolyte and the electroactive material, contributing to the higher specific discharge values⁶⁷.

Although small-sized particles are advantageous in terms of their electrochemical behavior in typical LIBs, due to their inherent agglomeration tendency stemming mainly from their high surface to volume ratio, the volumetric energy density can turn out to be low as the amount of electroactive material that can be loaded per unit volume (tap density) of the electrodes would be low⁶⁸. In addition, with a high surface area the solid electrolyte interface (SEI) that can form between the particle and the electrolyte would be even more exacerbated, leading to a higher probability of unwanted parasitic reactions and resulting in further capacity losses due to high surface energy.⁶⁹⁻⁷¹

For the same volume, the number of particles in a system consisting of small particles is higher compared to another one containing larger particles. For this reason, the interaction between particles is more in systems containing small particles as shown in Figure 2.4 (a) and higher suspension viscosities are expected in these systems as shown in Figure 2.4 (b)⁷².

Electroactive particle suspension viscosity is critical for both typical LIBs and suspension electrodes. For typical LIBs, cracks can form on the tape-cast foil during the preparation of the electrode if the slurry's viscosity is high, making its processing difficult. The viscosity of the suspension electrodes affects the pump power required for circulation of the suspension in the system. Low suspension viscosity for the same solid content is favorable as the required pump power, thus operational cost, is reduced.

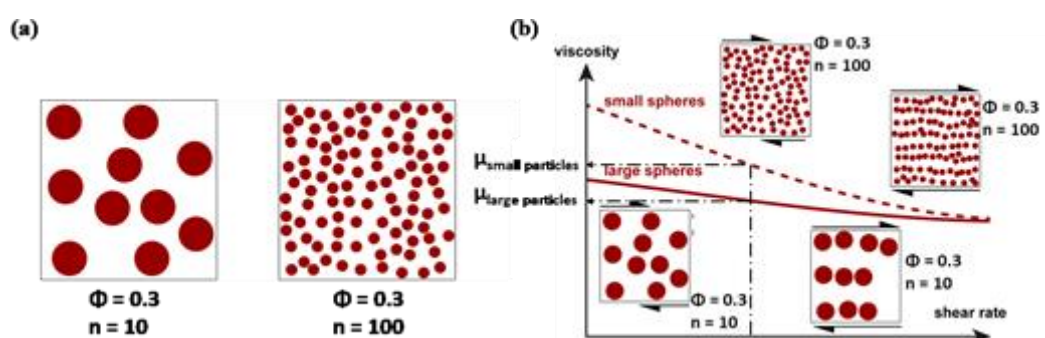


Figure 2.4. The relationship between particle size and viscosity. (a) The relationship between the particle size and the number of particles in the same volume. (b) The relationship between the particle size and the rheological behavior of suspensions with same particle loading.

Since Li^+ diffusion is easier in nano-sized particles, the electrochemical properties of nano-sized particles are better than the micrometer-sized particles, but they are not impressive in terms of properties that affect processing and operation, such as tap density and suspension viscosity.

2.5.2 Importance of Particle Shape

There is a direct relation between the crystal structure, particle shape and electrochemical behavior of electroactive materials. In LFP, Li^+ extraction and insertion occur along [010] direction (Figure 2.5 (a)). Reducing the diffusion path in this direction have the potential to fasten the Li^+ based redox reaction and increase

the specific discharge capacity. In order to reduce the thickness of crystal in [010] direction, the crystal growth should be directed towards [100] and [001] directions (Figure 2.5 (b))⁷³. Such directional growth of crystals results in asymmetric final particle morphology, i.e., plate-like morphology in olivine structure of LFP⁷⁴. Examples of plate-like LFP particles with crystal growth directed in the [100] and [100] directions are shown in Figure 2.5 (c).

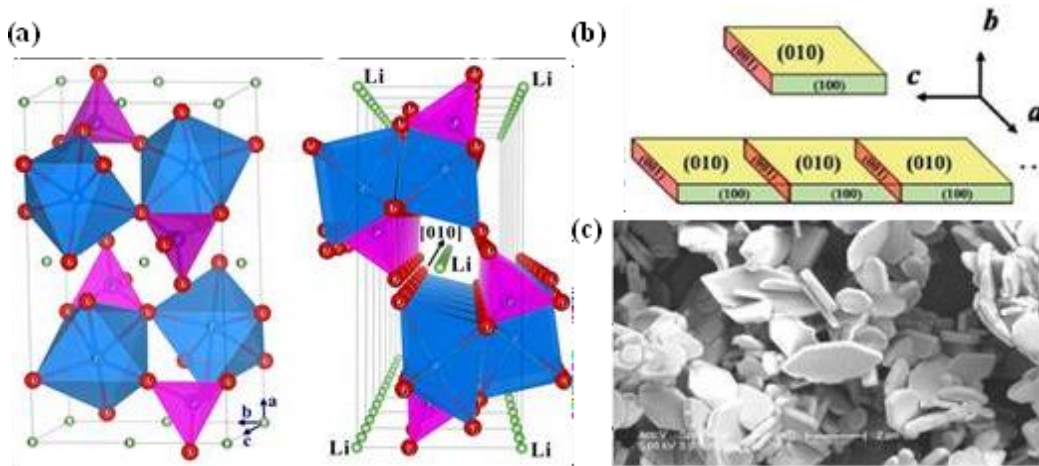


Figure 2.5. (a) Lithium-ion transfer paths in the LiFePO₄ unit cell⁷⁵. (b) The schematic representation of the morphology of (010) exposed LiFePO₄ particles⁷⁶. (c) The LiFePO₄ particles in plate-like morphology⁷⁷.

Pei et al. synthesized LFP/C nanoparticles (200 nm in size), nanorods (90 nm in diameter along b-axis and 200 nm-1 μm in length) and nanoplates (20 nm thickness along b-axis and 50 nm width) by hydrothermal method and FE-SEM micrographs of the synthesized particles are shown in Figure 2.6 (a), (b) and (c) respectively. It was found that specific discharge capacities rose as the crystal thicknesses decreased along b-axis as shown in Figure 2.6 (d)⁷⁸.

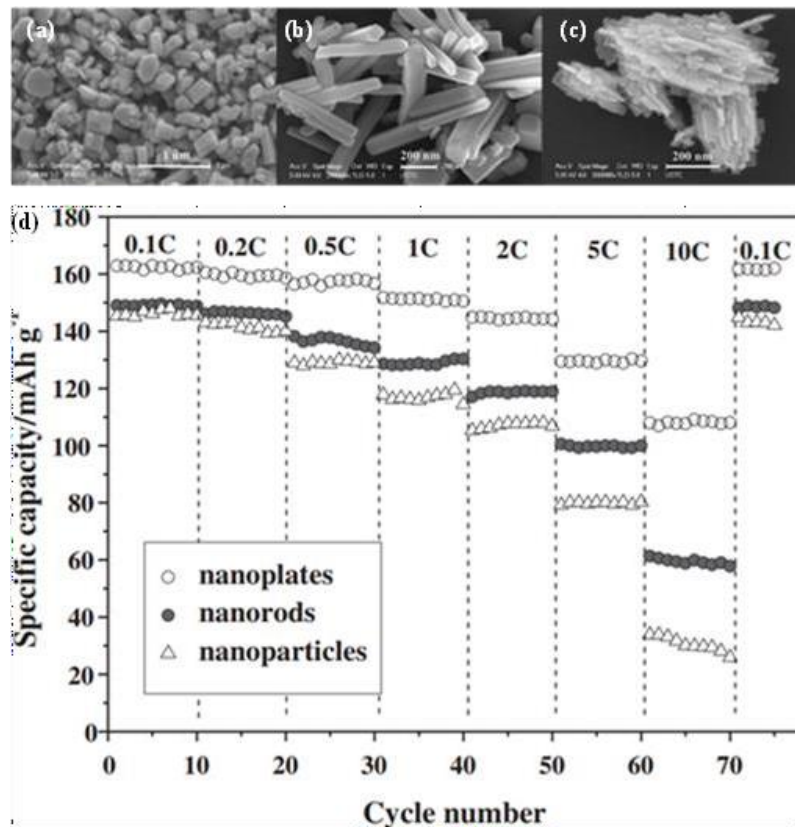


Figure 2.6. The FE-SEM micrograph of LiFePO₄ (a) nanoparticles, (b) nanorods, and (c) nanoplates. (d) The change of the specific discharge capacities according to the particle shape and the current rate⁷⁸.

Although the electrochemical characteristics of plate-shape LFP particles were superior compared to the ones of nanorods and nanoparticles, they can behave poorly in terms of their tap density which is another important aspect of electroactive materials. It is known that the random close packing densities of anisotropic particles are generally low, and the packing density increases as the particle aspect ratio (Length (L) divided by diameter (D)) decreases as shown in Figure 2.7⁷⁹. It is commonly assumed that combined with the nano-size effects discussed above, any anisotropy in the overall morphology of the particles lead to lower tap densities. Therefore, even if anisotropic particles may exhibit high specific discharge capacity (capacity/mass), their volumetric energy density (capacity/volume) may remain low⁶⁸. For increasing the tap density, thus the volumetric energy density, in LFP

electrodes, using spherical shaped particles were found to be the best option⁸⁰. Interestingly, Donev et al. revealed that ellipsoid shaped particles are more random densely packed than the spherical particles (Figure 2.7 (b) and (c)). They reported that the packing will be denser as the number of contact points without overlapping between the particles becomes higher due to the increased mechanical stability of the particles (Figure 2.7 (b)). The maximum packing density occurred when the ellipsoids' aspect ratio was equal to 1.5⁸¹.

The spherical shaped LFP particles were preferred not only for higher tap density but also for their low viscosity suspensions. As seen in Figure 2.7 (d), at the same solid amount (particle loading rate), the viscosity of the spherical-shaped particles is lower than the viscosity of the plate-shaped or rod-shaped particles⁸². When the anisotropic shape requirement for improved electrochemical performance and the spherical shape requirement for viscosity are considered, it is obvious that the shape of the particles should be optimized to develop Li-ion batteries with high volumetric energy density and better processing and operational capabilities.

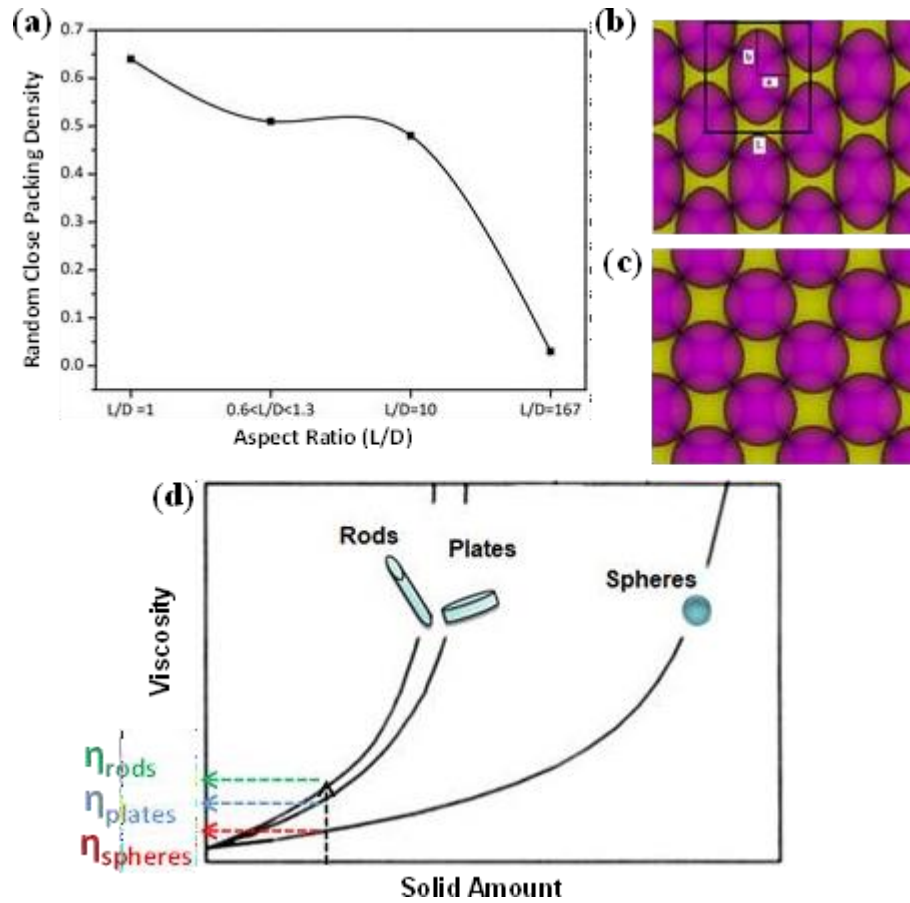


Figure 2.7. (a) The effect of particle anisotropy on the packing density. The packing density increases as the aspect ratio of the particles approaches 1 (as anisotropy decreases)⁷⁹. Packing of ellipsoid shape (b) and (c) spherical shape particles. The packing of ellipsoid shape is denser than the one of spherical shape⁸¹. (d) The effect of particle anisotropy on the suspension viscosity as a function of particle loading⁸².

2.5.3 Importance of Dispersibility

When particles with a certain average size are mentioned in any study, generally monodispersed single particles are considered, and these particles are thought to be suspended and homogeneously dispersed. However, it is often very likely that these particles are not well-dispersed but may be agglomerates or aggregates (or their

mixture) of the primary crystallites. Powders may compose of only primary particles (i.e., crystallites) after synthesis, however, they may form agglomerates via van der Waals interactions or aggregates via stronger chemical bonds, particularly during drying stage. Agglomerates and aggregates behave differently when re-dispersed in a liquid⁸³. Figure 2.8 summarizes these behaviors as such when dry powders are dispersed in the liquid, the agglomerates may break up into primary particles or remain as agglomerates. Aggregates, on the other hand, cannot break up but stay as they are or form larger agglomerates of aggregates.

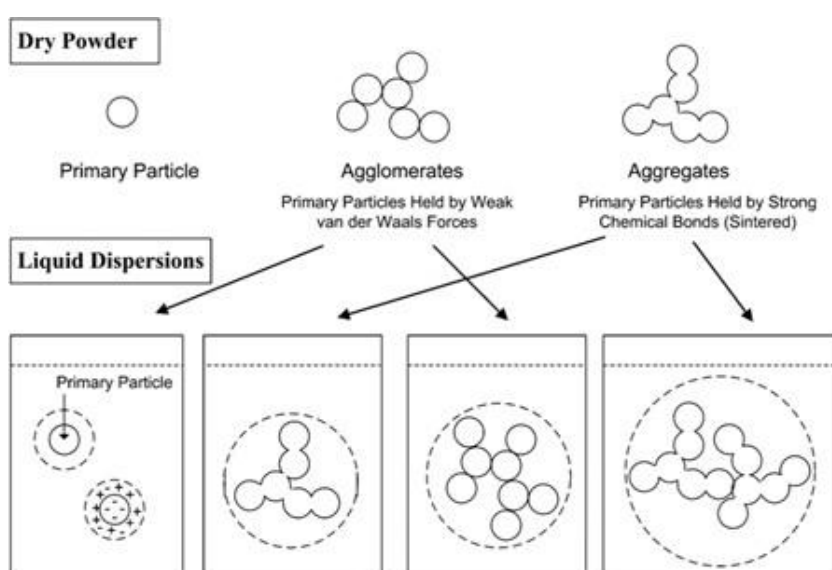


Figure 2.8. Dry and liquid states of particles⁸³.

Li^+ diffusion is higher for single particles compared to their agglomerates or aggregates because of their higher available surface area. As a result, the rate capability of dispersed particles increases^{29,84}.

The number of articles highlighting the importance of homogeneous dispersion of electroactive particles during electrode preparation have increased over the years because of its positive effect on electrochemical performance^{85–87}. In these studies, pre-existing agglomerations were detected and the electrode slurries homogenized through high-energy techniques such as ball milling and ultrasonication^{85,88}.

The agglomeration state of particles is also expected to have an impact on the ease of electrode processing because of its direct relation with the rheological behavior of suspension⁸⁹. The suspension viscosity of individually dispersed particles is commonly lower than that of agglomerated particles at the same solids content⁹⁰. Increased suspension viscosity in the presence of agglomerates or aggregates introduces operational challenges not only during electrode preparation in LIBs, but also in suspension flow batteries as the power requirement for circulation of electrode suspensions would increase. Moreover, use of such particles in suspension flow batteries may also result in sedimentation or accumulation of particles inside the cell assembly, which would then restrict their active use and lower the overall performance of the energy storage system.

2.6 The Control Over the Size and Shape of LiFePO₄ using Ascorbic Acid or Citric Acid

In nanomaterial synthesis, organic additives such as glucose, sugar, hexadecyltrimethylammonium bromide (CTAB), ascorbic acid and citric acid change the particle size and morphology by affecting the synthesis conditions. Therefore, these additives are widely used for particle design^{77,91-94}. Among these additives, citric acid (CA) is used in the synthesis of metal oxides in the Pechini sol-gel method. In the first step of this method, CA with its three carboxyl groups (Figure 2.9 (a)) can facilitate the formation of metal-citrate complexes with two or higher valence metal ions (Figure 2.9 (b)). In the next step, these complexes interact with the polyols (such as EG and PEG) and form polymeric resin (Figure 2.9 (c)). When high temperature (500 °C-1000 °C) process is applied to the polymeric resin, crystallized, pure metal oxide synthesis takes place⁹⁵.

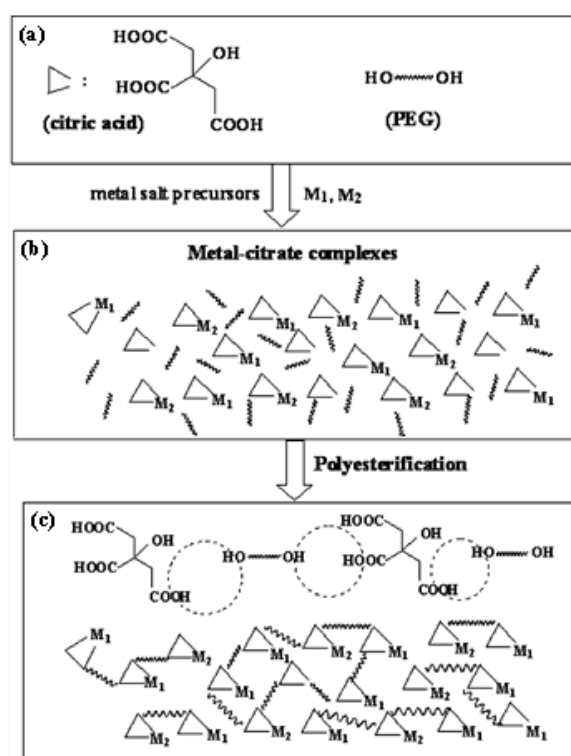


Figure 2.9. Pechini sol-gel method (a) Chemical structure of a citric acid and polyethylene glycol molecules. (b) Complexation reaction between citric acid and metal ions. (c) Polymerization reactions between citric acid, ethylene glycol and metal-citrate complexes⁹⁵.

When the LFP synthesis with the addition of CA is examined, it is seen that it was aimed both to prevent the formation of secondary phases by preventing the iron oxidation and to increase the electronic and ionic conductivity as a carbon source⁹⁶. Zhang et al., investigated the effect of CA on LFP particles synthesized by ball milling. They observed that the particle surfaces were rougher with the presence of CA, and this was attributed to the carbon coating provided by CA. Also, the surface area increased from 14 m²/g to 23 m²/g and the crystallite size decreased from 110 nm to 80 nm with the addition of CA⁹⁷.

Ascorbic acid (AA) (Figure 2.10) is also widely used in LFP synthesis. It is mostly used to prevent the iron oxidation and as a carbon source. For instance, Yang et al., investigated the effect of AA on LFP particles synthesized by hydrothermal method.

However, they reported that the addition of AA did not affect the composition, morphology, and size of LFP⁹⁸. Ni et al., on the other hand, reported that the addition of AA prevented the formation of secondary phase. While Li₃PO₄ secondary phase was observed in LFP particles without AA addition, pure LFP particles were synthesized after AA addition. Large agglomerates of 1 μm consisting of 100 nm primary particles have been reported without AA addition. However, 50-100 nm in size and nearly mono-dispersed particles were observed with the addition of AA. These differences were explained by the fact that AA adsorbed to the particles and prevented the particles from being fused⁹⁹.

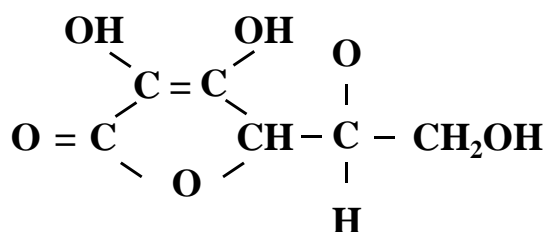


Figure 2.10. The chemical structure of ascorbic acid.

AA and CA added in the synthesis affect the acidity of the reaction medium. The acidity of the reaction medium affects the morphology of the synthesized particles. When the studies with reported pH values are examined, it is seen that the synthesis is mostly hydrothermal synthesis in which the reaction medium is water¹⁰⁰⁻¹⁰². In one of these studies, Gu et al., added ammonia to the reaction medium and changed the pH between 5 and 8. They reported that secondary phase was formed when pH was 5, 6 and 8. They associated the reason of this secondary phase with the H⁺ and OH⁻ concentrations in the reaction medium which changed the solubility of the reagents¹⁰³. Liu et al., synthesized LFP particles at pH range between 11.04 and 5.40 by controlling the amount of LiOH and H₃PO₄ used as reagents. Except for the highest (11.04) and lowest (5.40) pH value, LFP was obtained and it was concluded that LFP synthesis was favorable in a neutral or slightly basic reaction medium¹⁰². Song et al., changed the pH in the range of 2.50 and 8.87 using sulfuric acid and ammonia and reported the morphology change of the synthesized particles. While morphology of the synthesized particles was acute angle diamond flake-like when

pH was 2.5, it changed to hexagon flake-like, round flake-like and irregular flake-like as the pH increased. It is noteworthy that LFP was synthesized without the formation of secondary phase at pH as low as 2.5, contrary to other presented studies¹⁰⁴. Lin et al., adjusted the pH of the reaction medium with ammonia. The secondary phase was detected when pH was between 8.2 and 9.0. Pure LFP synthesis was possible when pH was 9.8. When the morphologies of the synthesized particles were examined, it was observed changes from cube-cluster-like to rugby-like structure when pH was increased¹⁰⁵. Studies reported with solvothermal method, where the reaction medium is EG, are limited. Huang et al., synthesized LFP particles by solvothermal method using EG as reaction medium. They changed the acidity of the reaction medium by adjusting the amounts of LiOH and H₃PO₄ and investigated the effect of acidity on particle morphology. They reported that (010) exposed spindle shaped plates were synthesized at pH values above isoelectric point where the net charge of the particle was zero. However, (100) exposed plates were synthesized below the isoelectric point (Figure 2.11). The difference between growth behavior at below and above the isoelectric point was explained by the absorption of different kinds of ions and complexes to different surfaces to stabilize naked the faces¹⁰⁶. Considering all these, it is seen that when the acidity of the reaction medium changes, the composition and morphology of the particles change, and these changes varied with the conditions of each study.

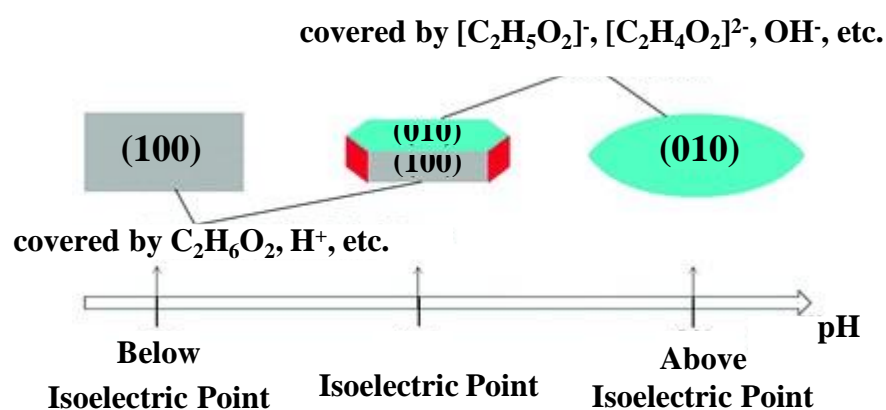


Figure 2.11. The changes in LiFePO₄ morphology with acidity of reaction medium¹⁰⁶.

Morphology design by controlling the selective growth of the surfaces using additives is a widely used method⁶⁴. In the study of Yang et al., using AA, CA, and PEG sources separately and under hydrothermal reaction conditions, the growth direction of the LFP particles and accordingly, the shape of the LFP particles could be varied significantly. In the synthesis using AA, (010) surfaces of the plate-shaped particles were emphasized, whereas (100) surfaces of the particles were remarkably larger when CA was used as the additive. No change in morphology was observed when PEG was added. This was explained by equally probable two causes; either LFP surfaces were not affected by PEG or all surfaces of the LFP were equally affected by it. The situation is different with AA and CA. It is thought that when AA is added, it adsorbs onto the high-energy surfaces, causing the growth of LFP crystals along the [200] and [002] directions and resulting in the synthesis of plate-shaped particles with a (020) enlarged surface. In the case of CA, a different mechanism is offered due to the strong chelating properties of CA towards Fe^{2+} and Li^+ ions. CA, due to the presence of Fe^{2+} and Li^+ ions in the (010) and/or (100) planes, most probably strongly chelated these ions and (100) surface-enlarged particles dominated the scene¹⁰⁷. The changes in the growth of the planes and morphology with the additives used can be seen in the XRD pattern presented in Figure 2.12.

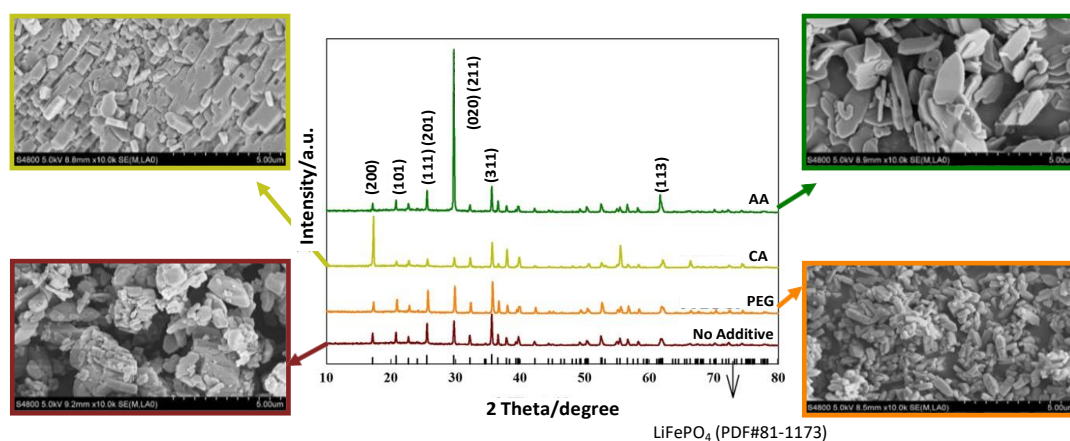


Figure 2.12. X-ray diffraction pattern and FE-SEM micrograph of synthesized LiFePO_4 particles showing the change of the crystallographic planes by addition of ascorbic acid (AA), citric acid (CA) and polyethylene glycol (PEG)¹⁰⁷.

2.7 Hierarchical LiFePO₄ Particles

LFP particles come in a variety of sizes and shapes as described in the earlier sections, and each structure has its own benefits and drawbacks. The electrochemical behavior of nanosized particles is superior compared to the larger ones while leading to low tap densities or vice versa. To benefit from the advantages of the LFP particles in all forms and sizes, synthesis of hierarchical LFP structures has drawn interest in recent years¹⁰⁸. In hierarchical structure, small primary particles are joined together in a specific order to form secondary particles so that the higher electrochemical performance of small sized primary particles and the higher tap densities of the larger secondary structures are brought together in one particle.

Examples of hierarchical LFP particles reported in the literature are presented in Figure 2.13. Wei et al. synthesized mono-dispersed spherical particles by the solvothermal method. The resulting particles were 8-10 μm in diameter and consisted of 20-30 nm thick plates (Figure 2.13 (a)). Although the mechanism of the formation of such primary or secondary particles was not clearly discussed, the use of polyvinylpyrrolidone (PVP) and lithium acetate (CH_3COOLi) in synthesis might have an effect. As a result, 155 mAh/g discharge capacity was attained at 0.1 C current density¹⁰⁹. Wang et al. reported the hydrothermal synthesis of spherical LFP particles with 10 μm diameter consisting of tightly cohered sheets (Figure 2.13 (b)). The formation of this structure was associated with the hydroxyl groups in the sucrose molecule used in synthesis and a discharge capacity of 154 mAh/g was reached at 0.1 C current density.¹¹⁰ Wang et al. used the solvothermal method to synthesize the microflowers shown in Figure 2.13 (c). These hierarchical structures consisted of rectangular nanoplates that were 6-8 μm long, 1-2 μm wide, and 50 nm thick. It was argued that the ratio of water to ethanol of the solvent has an effect on the morphology of the LFP particles. The hierarchical structure could be synthesized while using only ethanol as the solvent. However, when the solvent was changed to water and ethanol mixture, hierarchical structure was not obtained. Hierarchical particles had an initial discharge capacity of 162 mAh/g at 0.1 C¹¹¹. Xia et al.

synthesized mesoporous spindle-like particles with an initial discharge capacity 163 mAh/g at 0.1 C by the solvothermal method (Figure 2.13 (d)). These spindle-like particles were formed of numerous nanocrystalline self-assemblies of 100 nm length and 50 nm thickness. The pH of the reaction media was found to be effective in the formation of LFP primary particles in this specific shape and agglomeration of primary nanoparticles into secondary structures was explained by Oswald ripening¹¹². Guo et al. used the ionic liquid solvothermal method to synthesize the bow shaped LFP particles consisting of platelet subunits with thicknesses of 100-200 nm and widths of 300-500 nm as shown in Figure 2.13 (e). The homoepitaxial aggregation of plates to minimize the total energy of the system was reported as the formation mechanism of bow-shaped LFP particles¹¹³. The resulting particles had an initial discharge capacity of 156 mAh/g at a rate of 0.2 C. Wu et al. synthesized the 1-2 μm diameter LFP microspheres, shown in Figure 2.13 (f), that were composed of nanograins with a diameter of 20-100 nm, by chemical co-precipitation that is followed by heat treatment. The nano-grains were organized in an ordered pattern and attached side by side. It was discussed that polyethylene glycol (PEG, molecular weight 6000), which was utilized as a dispersant, helped the formation of hierarchical structures. These particles showed a discharge capacity of 160 mAh/g at 0.1 C of current density¹⁰⁸.

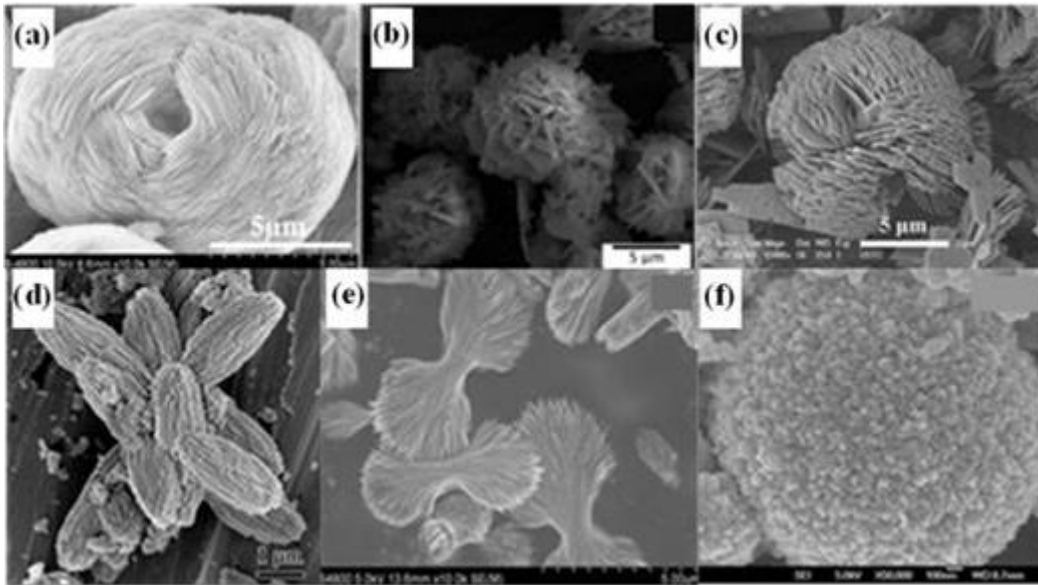


Figure 2.13. Examples of hierarchical LiFePO₄ particles (a) Spherical structure formed by dense compact nanoplates¹⁰⁹. (b) Sphere-shaped made of tightly cohered sheets¹¹⁰. (c) Microflowers which consist of rectangular nanoplates¹¹¹. (d) Mesoporous spindle-like particles¹¹². (e) Bow-shaped particles consisted of platelet subunits¹¹³. (f) Microspheres made of nanograins¹⁰⁸.

The common feature of all these particles with hierarchical structure was their high tap density (listed in Table 2.3) due to their shape and size. Compared the tap density values of nanosized particles are below 1.0 g/cm³¹¹⁴, the difference is significant. Although the suspension viscosities of hierarchical particles have not been reported in the open literature yet, it is expected to be much lower compared to the ones of nanosized particles with the comparable discharge capacity at same particle loading.

Table 2.3 Tap densities of hierarchical structures reported in the literature.

Tap Density (g/cm ³)	Reference
1.50	109
1.40	110
1.17	111
1.30	108

2.8 Objective of This Thesis

Literature review presented above attests to the strong need for a scalable and high yield electroactive material synthesis route. Although with their obvious advantages the polyol methods come forward, until now all efforts along those lines have been concentrated on using high chain polyols with the high temperature crystallization ability as the sought-after advantage. Despite the obvious fact that boiling points of the polyols would be lowered as more water was introduced to the reaction medium, it seems like this important point has just been neglected. Compared to inorganic reagents, acetates of the metal ions, which were the common choices in many of these polyol studies, are more soluble yet more costly. No studies have been found that provide a compromise between the solubility of more cost-efficient inorganic reagents, the amount of water added for increasing the solubility, and decrease in the boiling point of the reaction medium. In this study, the boiling point of the reaction medium was calculated as a function of the initial concentrations of the reagents and regarding the maximum solubilities of the reagents their initial concentrations were kept at reasonably high levels. With these reaction and reactor design constraints, a scalable and high yield LFP synthesis method that remained functional at relatively low temperatures was developed.

It was clarified in the literature review that optimization of shape, size and dispersion of LFP particles is needed for higher tap density, lower suspension viscosity and easier Li^+ diffusion. While keeping the ion diffusion paths is shown to be possible by preferential absorption of organic molecules on high energy crystal facets, these manipulations generally lead to anisotropic crystal growth that may not be optimal for high tap density and low suspension viscosity. For this reason, the synthesis of hierarchical structures comes to the fore. Particle design is further possible by changing the growth directions with the use of AA and CA, simultaneously. The addition of AA is known to cause the (010) plane to grow preferentially while the addition of CA has its effects such that the (100) surfaces are more exposed. While CA and AA were used separately in the synthesis of LFP in the reported

hydrothermal method, there have been no studies where these two additives were used together and within a polyol-based route. Considering all these aspects, it should be possible to design the primary and secondary structures of hierarchical LFP particles by adding these acids in the polyol separately, together, at different concentrations and feeding sequences. By constricting the crystallite growth along both high and low energy crystal facets and letting these crystallites build into higher order hierarchical structures that are preferably spherical, the performance goals stated above can be reached.

CHAPTER 3

EXPERIMENTAL DETAILS

3.1 Materials

Ortho-phosphoric acid (H_3PO_4 , 85.0%), lithium hydroxide (LiOH, 99.0%), iron (II) sulfate heptahydrate ($\text{FeSO}_4 \cdot 7\text{H}_2\text{O}$ 99.0+%), N-methyl-2-pyrrolidone (NMP) were purchased from Merck. L-(+)-ascorbic acid (AA, purity > 99%) and carbon black were purchased from Alfa Aesar. Mono(ethylene glycol) (EG, $\geq 99.5\%$) was purchased from Tekkim. Citric acid (CA, purity > 99%) was purchased from Fisher Chemical. Also, battery grade polyvinylidene fluoride (PVDF) was used. The reference carbon-coated LFP (has a Brunauer-Emmet-Teller (BET) specific surface area of $10 \text{ m}^2/\text{g}$) was used as received without further purifications and XRD diffractogram of the powder did not show any other phase than LFP. FE-SEM micrograph of the reference powder presented in Figure 3.1 (a). The particles are polydisperse, aggregated and has irregular shape. Particle size measurements presented in Figure 3.1(b) shows that the average size of particles is 430 nm in water according to number percentage distribution. The larger aggregates of particles with sizes of about $1.20 \mu\text{m}$ revealed themselves when volume percentage distribution was plotted. Deionized water (DIW) with the resistivity of $18.2 \text{ M}\Omega\text{-cm}$ and technical ethanol (EtOH, purity > 96%) and acetone (purity > 99.5%) were used.

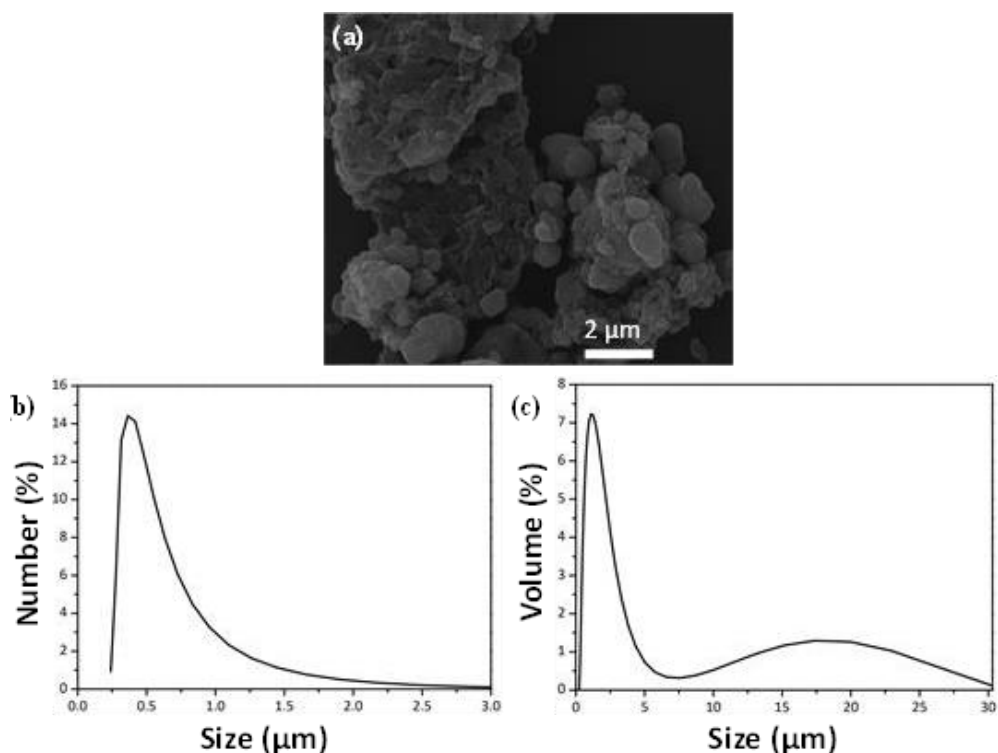


Figure 3.1. Characterization of the reference LiFePO_4/C particles. (a) FE-SEM micrograph. (b-c) Particle size measurements using laser diffraction. (b) Number-weighted and (c) volume-weighted size distribution of particles.

$\text{FeSO}_4 \cdot 7\text{H}_2\text{O}$ is a chemical very sensitive to humidity, so it was stored in a desiccator in order to keep the H_2O to FeSO_4 ratio constant.

3.2 Experimental Methods

3.2.1 Preparation of Reagents

For polyol synthesis of LFP nanoparticles, the molarity of the iron ions was fixed at 0.1 mol L^{-1} and the amounts of reagents were determined such that the stoichiometric ratio of $\text{Li}:\text{Fe}:\text{P}$ was 3:1:1. The total volume of precursor suspension was 180 mL.

Because of the direct effect of water content on the boiling point of EG, the total amount of water coming from the reagents were calculated and the corresponding

boiling point of EG was estimated. In order to set the reaction temperature to 170 °C, an excess of 0.054 mole of water was used to dissolve more LiOH in EG. The details of calculations were presented in Appendix A (Table A.1).

The reagents were separately dispersed and dissolved in EG for preparation of precursor suspension. To dissolve $\text{FeSO}_4 \cdot 7\text{H}_2\text{O}$ and H_3PO_4 (85 wt%), half and one sixth of the EG was used, respectively. LiOH was mixed with the rest of the EG (one third of the total EG) and the determined amount of extra water was added into this mixture to obtain homogeneous dispersion without any sedimented particles at the bottom of its container. Each mixture was magnetically stirred overnight at 35 °C (Step 1 in Figure 3.3). This mixing temperature was found to be critical, because, at lower temperatures, LiOH could not be homogeneously dispersed, while at higher temperatures, the color of the Fe-precursor solution was changed indicating the oxidation of iron ions. At the end of the stirring process, FeSO_4 and H_3PO_4 solutions were clear while the LiOH mixture was cloudy which was evidence for the complete dissolution of FeSO_4 and H_3PO_4 , and incomplete, but significant, dissolution of LiOH. The appearance of the resulting LiOH and FeSO_4 precursors were presented in Figure 3.2 (a) and (b), respectively.

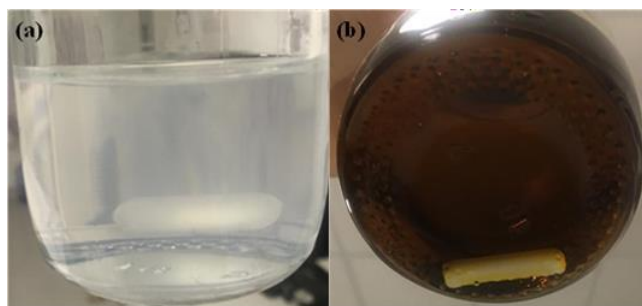


Figure 3.2. The photographs of (a) LiOH and (b) FeSO_4 precursors at the end of dispersion process.

3.2.2 Synthesis of LiFePO_4 Particles

For combination of reagents to form precursor suspension, first, FeSO_4 and H_3PO_4 were mixed simultaneously at 35 °C and magnetically stirred for 15 minutes (Step 2

in Figure 3.3). Clear solutions of FeSO_4 and H_3PO_4 precursors can be seen in Figure 3.4 (a). Then, LiOH dispersion was added into the mixture. This black-colored, viscous suspension (seen in Figure 3.4 (b)) was stirred for another 15 minutes to obtain homogeneity (Step 3 in Figure 3.3). The prepared suspension was transferred into a 250 mL, five-neck, round bottom flask, placed into a heating mantle and a refluxing condenser unit was attached on top of the flask (Step 4 in Figure 3.3). The temperature of the stirrer was first set to $170\text{ }^\circ\text{C}$ and monitored via both the thermocouple and the thermometer placed in the reaction medium. 20 mL aliquots were taken from the reaction medium first when the temperature is $35\text{ }^\circ\text{C}$ (initial condition), then when temperature reached to $120\text{ }^\circ\text{C}$, $150\text{ }^\circ\text{C}$ and $170\text{ }^\circ\text{C}$ during heating. The heating profile was recorded and presented in Appendix B (Figure B.1). After the temperature of reaction medium increased to $170\text{ }^\circ\text{C}$, the effect of reaction duration on LFP particle synthesis was investigated. To this end, two more samples, after 15 minutes and 9 hours, were taken from the reaction medium.

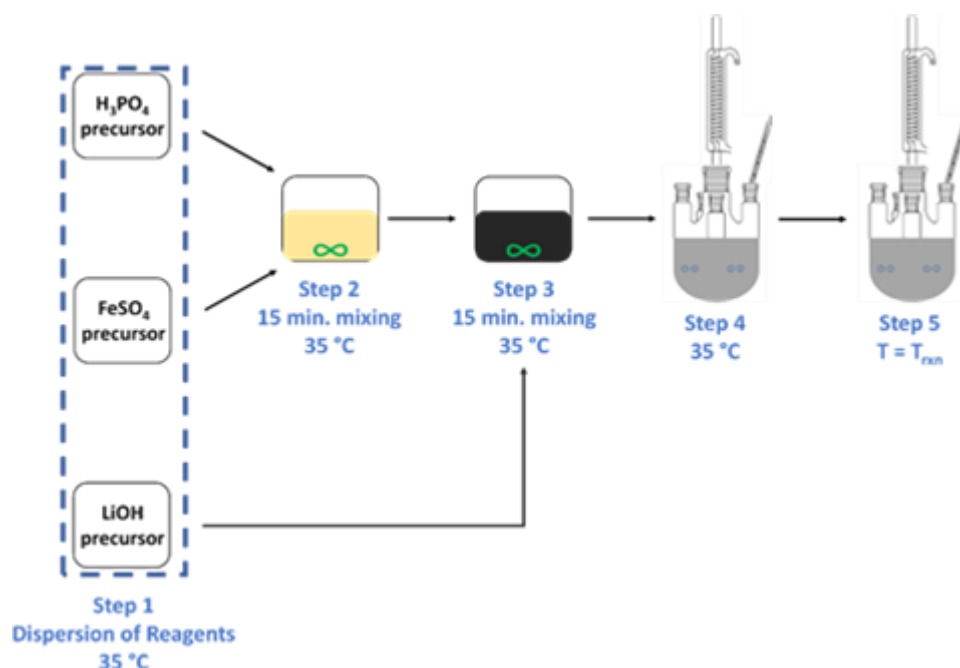


Figure 3.3. Schematic representation of LiFePO_4 synthesis.

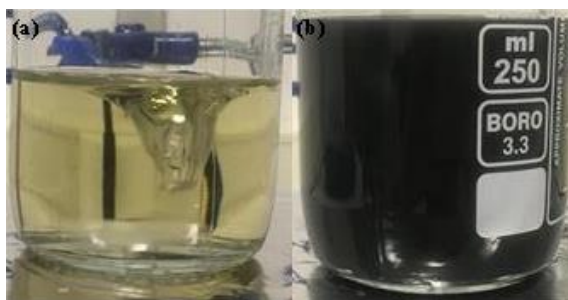


Figure 3.4. The photographs of the mixtures of (a) FeSO_4 and H_3PO_4 precursors (Step 2), and (b) FeSO_4 , H_3PO_4 and LiOH precursors (Step 3).

3.2.3 Synthesis of LiFePO_4 Particles with Acid Addition

The same procedure described in Section 3.2.2 was followed while investigating the effects of ascorbic acid and/or citric acid additions in polyol synthesis of LFP. The differences made in the experimental procedure were tabulated in Table 3.1. For ascorbic acid addition (Sample A), H_3PO_4 and FeSO_4 precursors were added simultaneously on the solid AA in Step 2 and the reaction temperature was set to $170\text{ }^\circ\text{C}$ and held at that temperature for 2 hours in Step 5.

For citric acid addition (Sample B), H_3PO_4 and FeSO_4 precursors were added simultaneously on solid CA in Step 2. The reaction temperature was set to $170\text{ }^\circ\text{C}$ and continued for 18 hours in Step 5.

Calculations of the amounts of AA and CA used were presented in Appendix C.

3.2.4 Combined Addition of Citric Acid and Ascorbic Acid

For the combined addition of CA and AA, three variations were employed. Compared to Sample A and Sample B, half of the original amount of each acid was used to keep the total amount constant for the first two cases. To prepare Sample C, H_3PO_4 and FeSO_4 precursors were added simultaneously on the CA and AA powder mixture in Step 2 as in previous cases. During preparation of Sample D, H_3PO_4 and FeSO_4 precursors were added simultaneously on the CA in powder form in Step 2.

AA was added (injected) 15 minutes after the reaction temperature was increased to 170 °C in Step 5. In both cases, the reaction duration was 2 hours.

In the third case (Sample E), the same experimental procedure used in preparation of Sample D was followed, but the amount of CA doubled, and the reaction time increased to 9 hours.

Table 3.1 Experimental details of ascorbic acid and/or citric acid addition

Sample	AA Amount (g)	CA Amount (g)	Addition of AA after 170 °C	Time (h)
A	0.722	-	No	2
B	-	0.720	NA	18
C	0.361	0.361	No	2
D	0.361	0.361	Yes	2
E	0.361	0.720	Yes	9

As a separate set of experiments, the effect of CA feeding sequence was investigated. Four different scenarios were studied as presented in Table 3.2. In all cases, AA was added into the reaction medium 15 minutes after the temperature had reached 170 °C in Step 5 and the reaction duration was 2 hours. The first scenario was Sample D. In the second one (Sample F), CA was added into phosphate precursor in Step 1. In the third case (Sample G), the total CA amount was divided into two and added into the phosphate and iron precursor solution in Step 1. In the last case, (Sample H), CA was added into the iron precursor solution in Step 1.

Table 3.2 Experimental details of feeding sequences and citric acid amounts.

Sample	CA in $[PO_4^{3-}]$ source	CA in $[Fe^{2+}]$ source
D	-	-
F	0.360	-
G	0.180	0.180
H	-	0.360

3.2.5 Post-Processes of LiFePO₄ Particles

After the completion of reaction, the powders were first washed off from the mother liquor, dried in an oven, then heat treated. In order to explore the influences of the post-processes on the particle properties, each process was examined separately.

3.2.5.1 Washing and Drying Procedures

After the synthesis of LFP particles, powder was first recovered by centrifugation at 10,000 rpm for 30 minutes. Then, washed, first, with DIW and then, with ethanol to remove the reaction residues. A total of 120 mL DIW and 120 mL of EtOH were used. After mixing each solvent with particles, the suspension was first magnetically stirred for 5 minutes, then ultrasonicated for another 2 minutes and magnetically stirred again for another 5 minutes. Centrifugation at 10,000 rpm for 15 minutes was applied to separate supernatant and the particles. The exact same procedure was then repeated using 120 mL of EtOH. This washing procedure was labeled as W₁ and used in synthesis of powders in this study unless stated otherwise.

To investigate the effect of excess DIW amount on the removal of reaction residues, the second washing procedure (W₂) was employed. In this case, the DIW amount was increased to 180 mL in the first step and this part of the procedure was repeated 3 times using 540 mL DIW in total. The procedure was continued with the regular ethanol-wash using 120 mL of EtOH.

The synthesized and washed LFP particles were dried in a drying oven at 120 °C overnight.

3.2.5.2 Heat Treatment Procedures

The dry powders were exposed to three different heat treatments. These heating procedures were plotted in Figure 3.5. Prior to heat treatments, the oven was purged with nitrogen gas (N₂) for 15 minutes and with argon gas (Ar) for 5 minutes at room

temperature. Argon gas-purge continued through the entire heat treatment. “HT_x” was added to the labels of the heat treated LFP particles where x defines the heating procedure.

In the first procedure (HT₁), the temperature was, first, increased from room temperature to 300 °C with rate of 2 °C/min and the sample was held at this temperature for 1 hour. Then, the temperature was increased to 600 °C with a heating rate of 10 °C/min and kept at this temperature for 3 hours.

In the second procedure (HT₂), the temperature was directly increased from room temperature to 500 °C with rate of 10 °C/min and the sample was held at this temperature for 1 hour.

In the third procedure (HT₃), the temperature was directly increased from room temperature to 500 °C with rate of 1 °C/min and the sample was held at this temperature for 1 hour.

The samples were let to cool in the oven until the temperature dropped to 120 °C. Temperature drop from 500 °C to 120 °C took 2.5 hours while it took 3 hours when it dropped from 600 °C. Argon-purge continued during the whole heating and cooling stages.

HT₂ was employed to all synthesized particles unless stated otherwise.

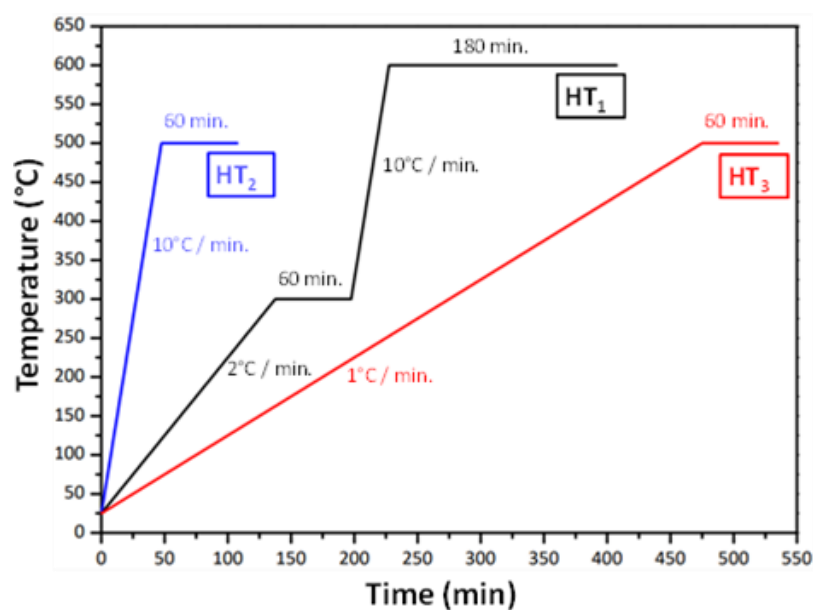


Figure 3.5. Heat treatments applied to synthesized LiFePO₄ particles.

3.3 Particle Characterization

X-Ray Diffraction (XRD) analysis of the powders was done using Rigaku Ultima-IV system with Cu K α radiation (0.154 nm) operating at 40 kV and 30 mA between 10 ° and 80 ° at a scanning rate of 2 °/min.

The crystallite sizes were calculated using the Scherrer equation ($d = 0.9 \lambda / \beta_{1/2} \cos \theta$) from the average of the 3 most intense peaks ($\lambda = 1.5406 \text{ \AA}$). LaB₆ was chosen as the standard to define instrumental broadening. The total broadening, or FWHM of the peaks, was calculated using Fityk-Curve and Fitting Software (PseudoVoigt function was used and the FWHM value of each peak was obtained after the fitting). Instrumental broadening was subtracted from the total broadening and the sample broadening was calculated. Finally, this value was replaced in the Scherrer equation, and the crystallite size was obtained.

For field emission scanning electron microscope (FE-SEM) sample preparation, 0.0125 g of powder was, first, dispersed in 5 mL of DIW and ultrasonicated for 2 minutes, then, a drop from this suspension placed onto a silicon wafer and left to dry.

A thin gold layer was deposited onto the samples for 2 minutes using Emitech SC7620 Sputter Coater. FE-SEM characterizations were done using FEI Nova Nano SEM 430. FE-SEM was operated under a voltage of 20 kV.

Image J software was used for particle size analysis. The pixel SEM micrograph dimensions were converted to physical dimensions by Analyze → Set Scale section. The particles were then counted (Appendix E) and the average particle size and standard deviation of the particles was calculated.

High-resolution transmission electron microscope (HR-TEM) analysis was carried out by JEOL JEM2100F. To prepare the HR-TEM samples, the powders were mixed with ethanol and held in an ultrasonic bath for 60 minutes. A drop from this suspension was placed onto the CF300-Cu Carbon film grid with a micropipette and left to dry overnight.

Particle size analysis of the reference LFP/C particles was conducted using laser diffractometry (Mastersizer 2000S, Malvern Instruments). Before the analysis, 0.0125 g of powder was, first, dispersed in 5 mL of DIW and ultrasonicated for 2 minutes. Analysis was done in DIW, pump power was 3,500 rpm and ultrasonication was 100% during the measurement.

Brunauer-Emmett-Teller method was used for the surface area analysis performed under nitrogen atmosphere by Quantachrome Autosorb 1C-MS analyzer.

Fourier transform infrared spectroscopy (FTIR, Frontier-PerkinElmer) with PIKE GladiATR Reflection Specular Reflectance tool was performed at room temperature to identify absorption bands at the surface of LFP particles.

To calculate the tap density, a volume of 0.1 cm³ was filled with powder and the weight of the powder was measured. To place the powders in the eppendorf (0.5 cm³) properly, after adding the certain volume of powders, the cylinder was hit to the laboratory bench 1000 times, and more powders added to fill the entire volume. This experiment was repeated three times from the start, the tap densities were computed, and the average of the results were reported with the standard deviation. Due to the

human factor in these experiments, the results may not reflect the absolute values, yet they are expected to be self-consistent.

3.3.1 Electrochemical Behavior

For organic electrolyte system, electrodes were prepared by mixing LFP powders, carbon black and polyvinylidene difluoride in N-methyl-2-pyrrolidone solvent (5 wt.% NMP-PVDF solution) in a mixer mill with a ratio of 60:30:10. A doctor blade was used to coat the slurry onto an aluminum foil current collector with a thickness of 200 μm after mixing. The coated slurry was cut into 18 mm diameter discs after being pre-dried on a hot plate at 120 $^{\circ}\text{C}$ for half an hour. Finally, NMP and moisture were evaporated by drying the electrode for 12 hours at 120 $^{\circ}\text{C}$ under vacuum. As counter electrode and separator, lithium foil (half-cell tests) and glass microfiber paper were used respectively. The electrolyte was a mixture of ethylene carbonate (EC) and dimethyl carbonate (DMC) (1:1) including 1 M LiPF_6 . Cells were constructed in an argon-filled glove box. Measurements were performed on a Bio-Logic EC-LAB MPG2 electrochemical station (Bio-Logic Science Instruments).

For experiments with aqueous electrolyte, a 3-electrode vial cell setup, 3-electrode system was used. Ag/AgCl, platinum (Pt) wire and 2.5 M $\text{Li}_2\text{SO}_4(\text{aq})$ were used as reference electrode, counter electrode and electrolyte, respectively as shown in Figure 3.6. The working electrode was fabricated with LFP:CB:PVDF ratio of 60:30:10. First, LFP powders, carbon black and binder were mixed in a mortar and a homogenous mixture was obtained. After cutting three Nickel (Ni) foams with a diameter of 1.4 mm, foam with a diameter of 0.7 mm was cut out of one of the foams and a small foam and a ring-shaped foam were obtained. All nickel foams were cleaned with acetone and ethanol for 10 minutes before drying for 30 minutes at 90 $^{\circ}\text{C}$. The prepared slurry was applied to small foam and dried at 120 $^{\circ}\text{C}$ overnight. After pressing two pieces of 1.4 mm diameter foam initially under 800 psi (pre-pressing), this assembly was placed on the bottom. The small foam that was loaded with the slurry and ring-shaped foam that fitted around this were placed in the

middle. Ni wire with a diameter of 0.8 mm, which was used as a current collector, was attached to this structure and other large, pressed foam (i.e., two pieces of 1.4 mm diameter foam pre-pressed under 800 psi) was placed on top of all. The working electrode was ready for testing after this sandwich was additionally pressed at 4500 psi. Before starting the electrochemical measurements, the electrolyte was purged with N_2 and the gas continued to flow over the electrolyte during the whole measurement. Measurements were performed on a VersaSTAT 3 electrochemical station (Princeton Applied Research).

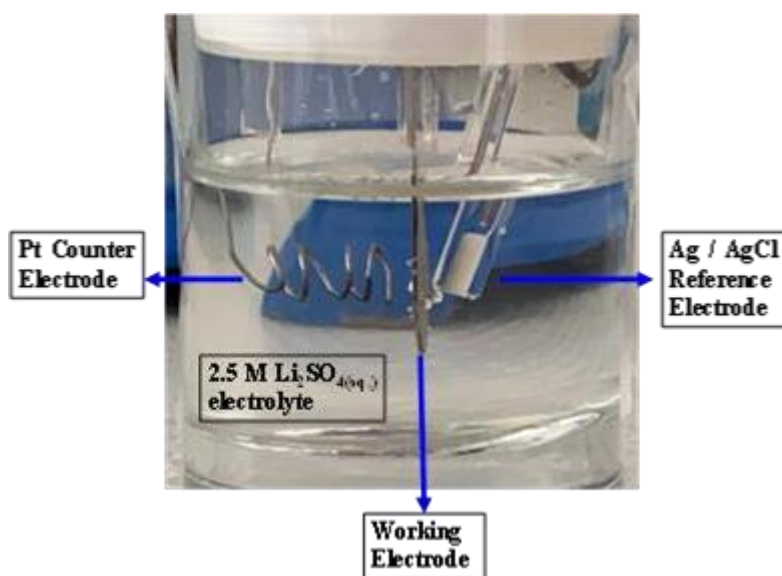


Figure 3.6. The 3-electrode system used for measurements in aqueous electrolyte.

3.3.2 Rheology Measurements

For characterization of rheological behavior, suspensions containing 40 wt.% of powder were prepared in DIW. Prior to the experiment, suspensions were magnetically stirred for 2 hours. A rheometer (Anton Parr, MRC 102) with a cone and plate geometry (stainless steel with diameter of 40 mm and 4° of cone angle) was used to characterize the rheological behavior of aqueous LFP suspensions. A solvent trap was used to avoid water evaporation during the measurements. Four consecutive measurements were recorded at $25^\circ C$. Each run consisted of 2 half loops

(downward and upward). During the upward loop, the shear rate increased from 0.5 to 500 s^{-1} and decreased from 500 s^{-1} to 0.5 during the downward loop. There were 31 points recorded for each half loop. The data was reproducible for each of the 4 runs and the measurements recorded during the last run were reported.

For sedimentation experiments, suspensions containing 1 wt.% of powder were prepared in 10 mL of DIW. Prior to the experiment, suspensions were ultrasonicated for 2 minutes. Sedimentation behavior of the suspensions was observed for a week.

CHAPTER 4

POLYOL SYNTHESIS OF LiFePO_4

The synthesis of crystalline LFP particles in EG was studied with a reaction vessel operated under ambient atmospheric pressure condition. Using EG as a solvent was a challenge in such a system, because the relatively low boiling point of EG compared to its longer-chain counterparts could have been inadequate for crystallization of LFP. Moreover, it was realized that the water coming from the reagents could further decrease the boiling point of EG as they are miscible within each other. Using inorganic salts possesses the cost advantage in LFP synthesis via polyol processes, yet their solubility in EG is related with the overall water content of the mixture. Therefore, it was important to find the maximum possible reaction temperature at a given set of initial concentrations of the reactants. Based on the rough stoichiometric calculations presented in Appendix A, the reaction temperature that could be kept stable within 1 °C was estimated to be 170 °C in the experimental setup used in this study. The effect of temperature on crystallization of LFP particles was studied by taking aliquots of samples during heating up of the reaction medium at various temperatures. These samples taken from the reaction medium were characterized. The pH values of the samples were presented in Table 4.1. As shown in Figure 4.1 (a), the color of the reaction medium changed from black to lighter gray at 150 °C and greenish at 170 °C.

Table 4.1 pH values of the samples taken from the reaction medium.

Sample	<i>pH</i>
35 °C	7.62±0.01
120 °C	6.67±0.02
150 C°	6.41±0.02
170 °C	6.36±0.01
170 °C 15 min.	6.45±0.01
170 °C 9 h.	5.09±0.01

XRD analysis of the collected powder samples, presented in Figure 4.1 (b), showed that the crystallization started at temperatures higher than 120 °C. At 120 °C and below, the powders were amorphous. Upon reaching temperatures 150 °C and higher, crystallization started as inferred from the defined peaks of XRD diffractogram. Although the amorphous contribution was detected at 150 °C, it was not at 170 °C. All the diffraction peaks could be indexed to the orthorhombic olivine structure (space group Pnma). The absence of any peaks in XRD diffractograms which could be associated with Fe³⁺ impurities was noteworthy. Such impurities are common in LFP synthesis and may reduce the rate capability and cause instability¹¹⁵. In order to eliminate impurity or second phase formation, either the reactions were conducted under inert atmosphere or additional heat treatments were employed. In polyol synthesis with EG, we could eliminate their formation probably because EG has a better reducing ability.

FE-SEM micrographs in Figure 4.1 from (c) to (h) were correlated with the XRD diffractogram. While irregular, large, agglomerated particles were observed in samples synthesized temperatures at 120 °C or lower, the dissolution of irregular,

agglomerated particles into fusiform shaped LFP crystals began at 150 °C. Well-shaped, fusiform LFP crystals were only observable when the reaction temperature increased to 170 °C. Combined with SEM analysis, the color changes observed during the course of the reaction was found to be related with the changes in the reaction medium. While the light gray color was associated with the irregular shaped, amorphous structures, the greenish color and the low viscosity of the reaction medium was associated with crystallization. When compared to the studies in Table 2.1, it is seen that 170 °C is the lowest temperature at which the synthesis of crystalline LFP particles was reported.

Even though all the irregular shaped particles were seemed to be disappeared at 170 °C according to SEM analysis, it is still critical to calculate the yield, i.e., the amount of LFP particles produced based on the reactants used, in terms of the feasibility of the synthesis technique. There is no reported study in the literature about the yield of LFP powders synthesized via polyol route. In theory, for the reactants used in this study (0.054 mol LiOH, 0.018 mol H₃PO₄ and 0.018 mol FeSO₄), 0.018 mol of LFP is expected to be synthesized if the reaction yield is 100%. In this study, when the temperature reached 170 °C, the reaction yield was determined as 91%. When the synthesis time extended to 9 hours, the reaction yield was increased to 97% (calculations for the reaction yields were described in Appendix A.). As observed in Figure 4.1, the crystal structure or the morphology of particles did not significantly change with time during the course of the reaction at 170 °C. Since highest yield was obtained for synthesized particles at 170 °C for 9 hours of reaction, these particles are further characterized and used in the rest of work if otherwise indicated.

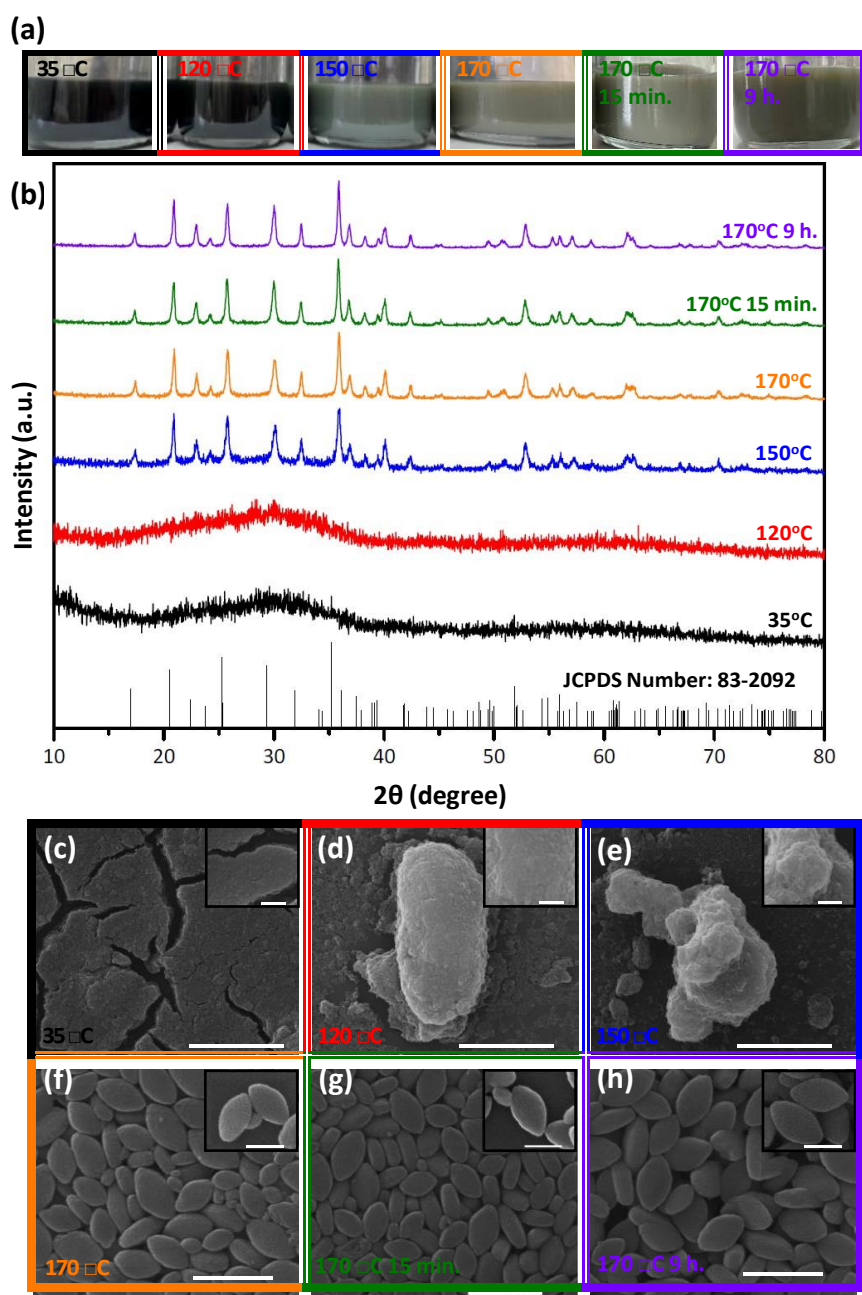


Figure 4.1. Crystallinity, color and morphology change of synthesized LiFePO_4 particles with reaction temperature and duration. (a) The color changes of the reaction medium. (b) The X-ray diffraction patterns. The FE-SEM micrographs of (c) 35 °C, (d) 120 °C, (e) 150 °C, (f) 170 °C, (g) 170 °C after 15 min., (h) 170 °C after 9 h. For (c), (d) and (e), the inset scales are 1 μm and the outer scales are 1 μm . For (f), (g) and (h), the inset scales are 500 nm, and the outer scales are 1 μm .

The FE-SEM analysis of these particles at higher magnification (Figure 4.2 (a)) showed that the synthesized particles had hierarchical structure such that secondary structures were formed from collection of much smaller primary particles. These primary particles could also be detected in the HR-TEM nanographs (Figure 4.2 (b) and (c)). At higher magnifications, it was realized that the primary particles were almost spherical. The short chain of EG was considered to play an important role in the formation of the spherical morphology of the primary particles. Because the ion exchange rate varies with the length of the polyol used as the reaction medium, it affects the growth mechanism of the particles. As the steric effect is found to be less in short-chain polyols, faster ion exchange and higher growth rates occur when the reaction media is EG¹¹⁶. This condition might facilitate the faster access of Li⁺, Fe⁺² and PO₄⁻³ ions to the particle surface compared to long-chain polyols and led to the isotropic growth.

The primary particle size was calculated using the Scherrer equation as ~40 nm. The BET specific surface area of the sample was measured as 25 m²/g. The average equivalent particle size can be calculated using the equation $D_{\text{BET}} = 6000/(\rho \cdot \text{SA})$ where D_{BET} is the average diameter of spherical particles, ρ is theoretical density (3.47 g/cm³ for LFP), and SA is surface area by assuming the particles are solid, spherical-shaped, monodisperse and non-porous¹¹⁷. The non-porous, spherical equivalent of the sample had an average diameter of 70 nm. The secondary size measured from the FE-SEM micrographs using ImageJ software was 400±65 × 255±35 nm. The difference between the secondary particle sizes indicated that the sample had a porous structure. The porous structures allow the electrolyte to penetrate between the particles, thus providing enhanced interface between electroactive material and electrolyte. The pathway providing Li-ion diffusion is expected to be larger in porous structures compared to non-porous structures due to the enhanced interface between electroactive material and electrolyte, resulting in better electrochemical performance¹¹⁸. Considering the recently reported BET specific surface area values, the obtained specific surface area is notably high^{119–122}. Also, the formation of secondary particles in fusiform shape from spherical primary

particles might be attributed to the presence of EG, because EG is known to act as a soft template for nanomaterials and responsible for facilitating the assembly of nanoparticles into nanoplates^{73,123,124}. In addition to being a reducing agent, EG had also been found to play a role in the morphology of primary particles and formation of hierarchical structures as a soft template. Our experiments involving organic acid, discussed in next chapters, further supported this conclusion.

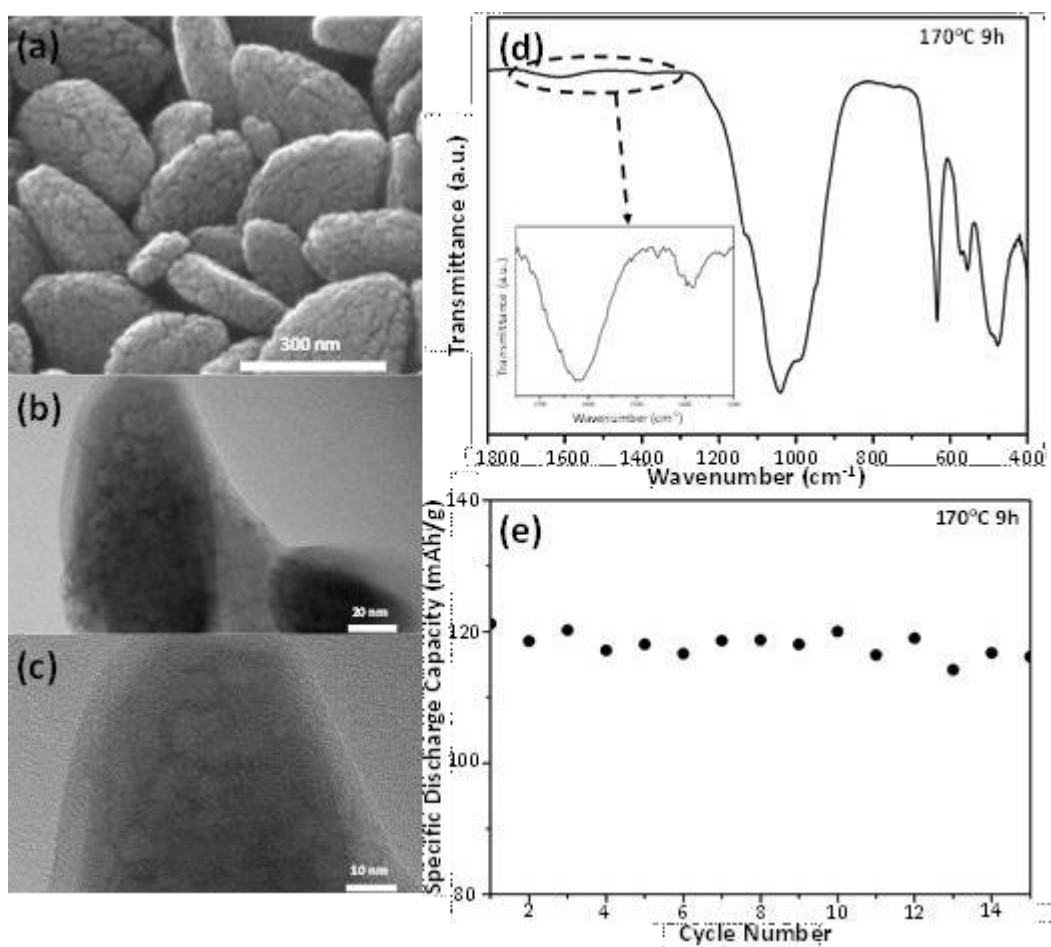


Figure 4.2. Characterization of LiFePO_4 particles synthesized at $170\text{ }^\circ\text{C}$ for 9 h. (a) The FE-SEM micrograph. The HR-TEM nanographs at (b) relatively low and (c) relatively high magnifications. (d) ATR-FTIR spectrum in the wavenumber range of $1800\text{-}400\text{ cm}^{-1}$. (e) The specific discharge capacities at a current rate 0.1 C .

The amorphous coverage around crystalline LFP particles was observed in HR-TEM nanographs even though they were not obvious enough to distinguish in SEM

micrographs (Figure 4.2 (a)-(c)). The ATR-FTIR analysis of the powders showed that only intrinsic LFP bands were observed in the fingerprint region between 1300-400 cm^{-1} , indicating no impurity phase (Figure 4.2 (d))¹²⁵. Stretching vibrations of PO_4^{3-} ions were observed in the wavenumber range of 1300-850 cm^{-1} and bending vibrations in the range of 650-400 cm^{-1} ¹²⁵. The peaks were observed in the 1750-1500 cm^{-1} and 1450-1300 cm^{-1} wavenumber range associated with C-O stretching, O-H bending and C-H bending and indicating the organic residues remained on the particles after synthesis and washing procedures.

The electrochemical charge-discharge test in organic electrolyte was carried out to assess the electrochemical performance over the voltage range of 2.5-4.2 V and a current rate of 0.1 C for 15 cycles as shown in Figure 4.2 (e). The specific discharge capacity of the sample was measured as 121 mAh/g. This value was measured as 115 mAh/g at a current rate 0.05 C for the LFP particles with similar secondary particle size and morphology, synthesized by the solvothermal method and increased electronic and ionic conductivity by carbon coating. 70 nm Li^+ diffusion path was considered as the reason for low specific discharge capacity⁶⁶. Since smaller primary particles provided shorter Li^+ diffusion path, higher specific discharge capacity at higher current rate could be obtained although subsequent heat treatment, coating or doping was not applied. It is known from ATR-FTIR spectra and HR-TEM micrographs that powder has amorphous organic residues. By applying heat treatment, the specific discharge capacity can be increased by carbonization of organic residues around the particle.

CHAPTER 5

THE INFLUENCE OF POST-PROCESSING TREATMENTS ON THE DISPERSIBILITY AND PURITY OF LiFePO_4

It was shown in the previous chapter that organic mother liquor residues were present on the synthesized LFP particles. There are three ways reported to eliminate or minimize the remaining EG on particle surface: (i) carbonization of residues via heat treatment (graphitization), (ii) removal of organic residues via repeated centrifugation and dispersion (washing) with water, and (iii) exchange of organic residues using strongly coordinating agents³³. Each of these approaches were evaluated and discussed in this chapter.

5.1 Effects of Heat Treatment

With heat treatment, organic residues are either be completely removed from the surface or converted in to carbon via its pyrolysis¹²⁶. Heat treatment can also increase the crystallinity of the LFP powders which are synthesized at relatively low temperature¹²⁷. Presence of carbon on LFP particles are known to enhance the electronic and ionic conductivity, which lead to higher discharge capacities¹²⁸.

Three different heat treatment procedures were applied to the synthesized LFP particles. In the first case (HT₁), temperature was increased to 300 °C with heating rate of 2 °C min⁻¹ and then increased to 600 °C with heating rate of 10 °C min⁻¹ and kept at this temperature for 3 hours. Even though the heat treatment was performed in inert argon atmosphere, oxidation peaks appeared in XRD diffractogram indicated the oxide formation (Figure 5.1 (a)). While the color of the LFP particles was initially green, after the heat treatment, it turned to red, which is the color of iron oxide (Fe_2O_3). The particles were dispersible in DIW and had a green color before the heat treatment (Figure 5.1 (b)). After the heat treatment, sedimentation occurred when the

particles were dispersed in DIW, and the color of the suspension were orange (Figure 5.1 (c)).

The SEM micrographs, given in Figure 5.1 (d), showed that the particles' fusiform shape deteriorated, and the necks were formed between the particles which might explain the particle sedimentation behavior observed in Figure 5.1 (c).

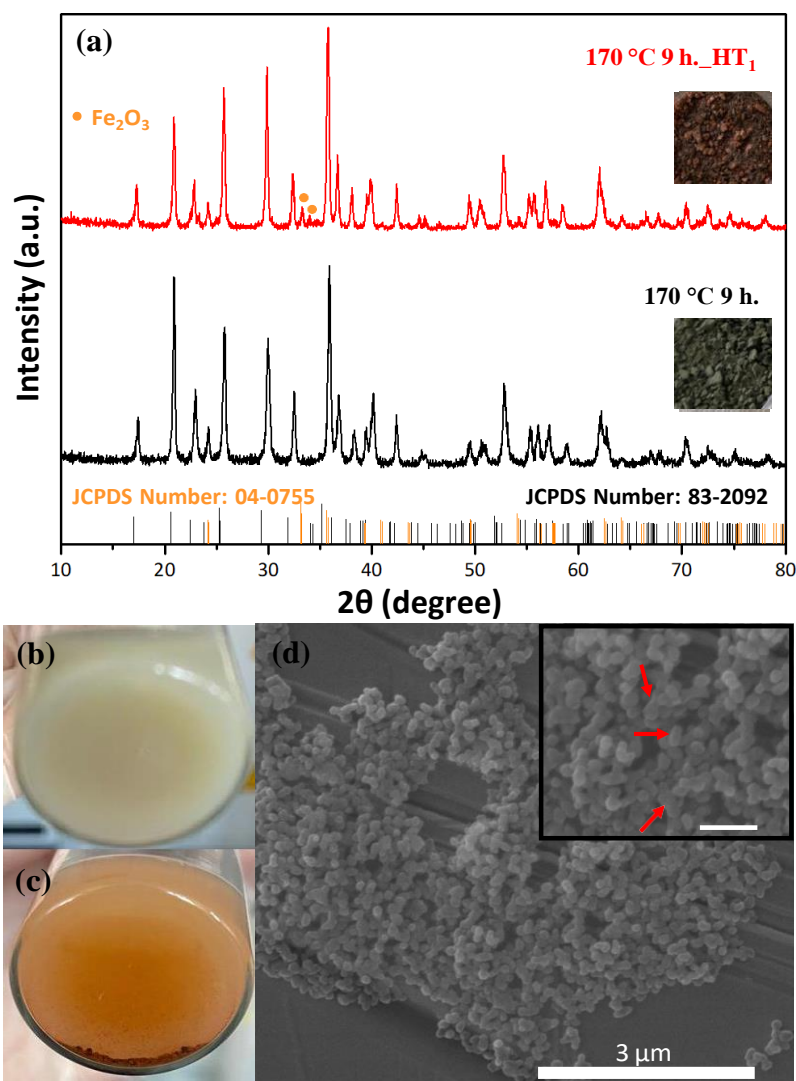


Figure 5.1. The characterization of powders exposed to Heat Treatment Procedure 1. (a) The X-ray diffraction patterns and the color of powders before and after the heat treatment. The dispersion characteristics of powders in DIW (b) before and (c) after the heat treatment. (d) The FE-SEM micrographs of particles after HT₁. The arrows on the inset figure show the interparticle necks. Inset scale is 500 nm.

The second heat treatment procedure (HT₂) was applied under the same atmospheric conditions at lower temperatures (500 °C) and for a shorter time (with heating rate of 10 °C/min) to avoid oxidation and hard agglomeration. As inferred from the XRD pattern in Figure 5.2 (a), the oxide peaks disappeared, yet formation of hard agglomerates persisted as observed in the SEM micrograph in Figure 5.2 (b) and sediments can be seen in the images presented in the inset of Figure 5.2 (a). It is noteworthy that the morphology of the particles was preserved during the heat treatment. The necks formed between the particles could be clearly seen in the HR-TEM nanographs of the particles that were subjected to heat treatment (Figure 5.2 (c)). Based on this analysis, the neck formation seemed to be originating from the organic residues because they served as a binder.

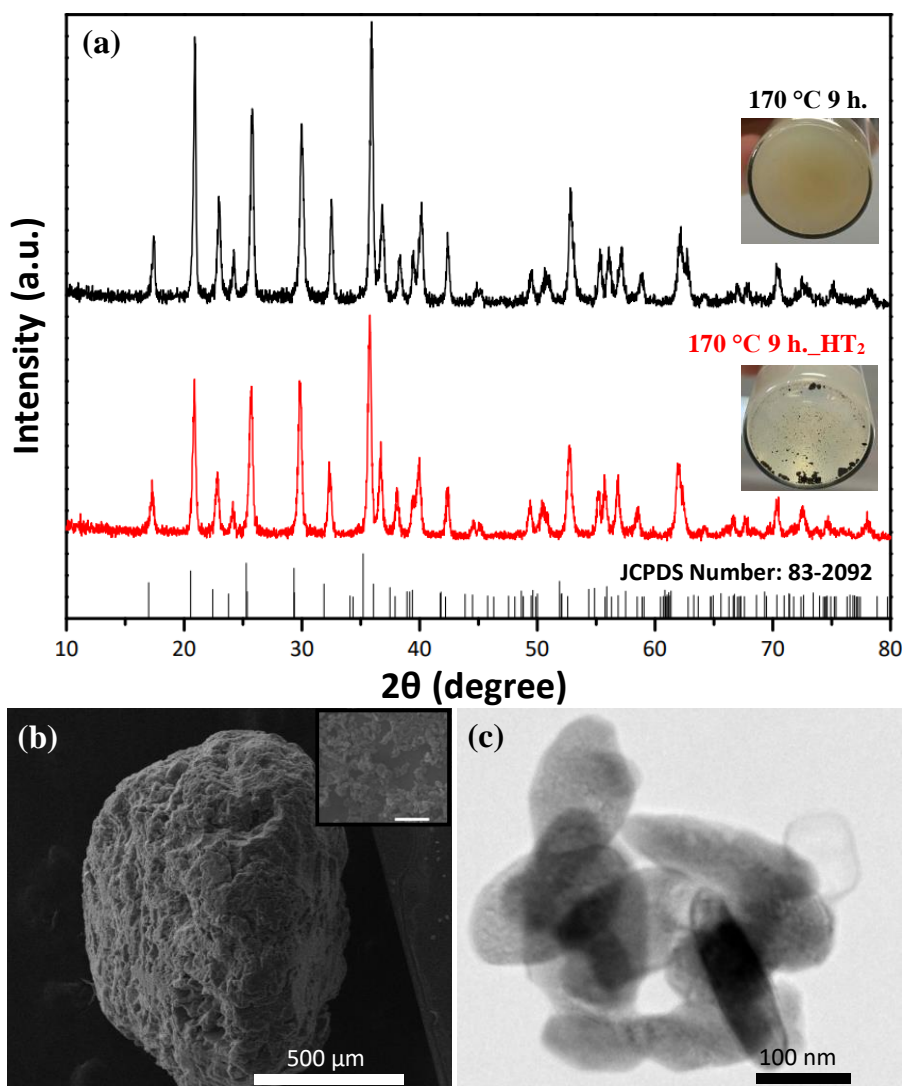


Figure 5.2. Characterization of LFP particles exposed to Heat Treatment Procedure 2. (a) The X-ray diffraction patterns and dispersibility of particles in DIW before and after the heat treatment. (b) The FE-SEM micrographs of the heat-treated powders. The inset figure (the scale bar is 1 μm) shows the particles on the surface of the agglomerate. (c) The HR-TEM nanographs of the heat-treated sample.

In order to minimize the hard agglomerate formation during heat treatment, the third heat treatment procedure (HT₃) was employed at the same temperature, but with a slower heating rate of 1 $^{\circ}\text{C}/\text{min}$. Slowing down the heat treatment duration was not effective in elimination of hard agglomerate formation (Figure 5.3 (a)) and the heat-

treated particles were not dispersible enough and black sediments were seen at the bottom of the container soon after particles were dispersed in DIW (Figure 5.3 (c)).

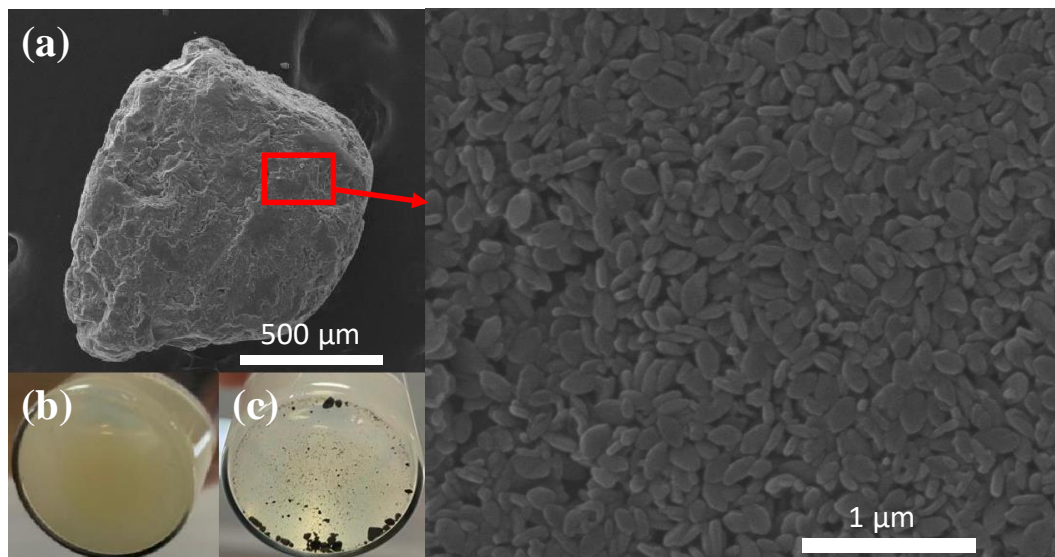


Figure 5.3. Characterization of LFP particles exposed to Heat Treatment Procedure 3. (a) FE-SEM micrographs of the heat-treated particles. Dispersibility of particles (b) before and (c) after the heat treatment.

Even though the oxidation could be prevented with heat treatment at 500 °C under inert argon atmosphere and remaining organic residues could be converted into carbon, during carbonization necks formed among the LFP particles and led to a hard agglomeration problem regardless from the heating rates used during the treatments.

5.2 Effect of Washing Procedure Applied After Synthesis on the Particle Dispersion

Neck formation during carbonization was considered to be originated from the organic residues (i.e., EG in the reaction medium) left among the particles. In order to solve the severe agglomeration problem experienced during heat treatments, more vigorous washing was applied to the as-synthesized particles in order to remove these organic residues between the particles. Since EG is miscible with water at room temperature in all proportions, it was planned to remove the EG-based mother liquor

using more DIW with extensive dispersion-centrifugation steps in the second washing procedure (W_2). The ATR-FTIR analysis of the LFP particles washed with the procedure W_2 were presented in Figure 5.4 (a). In Figure 5.4 (a), the 1750-1500 cm^{-1} and 1450-1300 cm^{-1} regions which were assigned to organic residues which may include C-H bending, O-H bending, and C-O stretching and confirmed that organic residues from mother liquor could not be completely eliminated. When these powders were also subjected to heat treatment (HT_2) and dispersed in DIW, the sedimentation occurred again indicating that the hard agglomeration problem persisted (Figure 5.4 (b)).

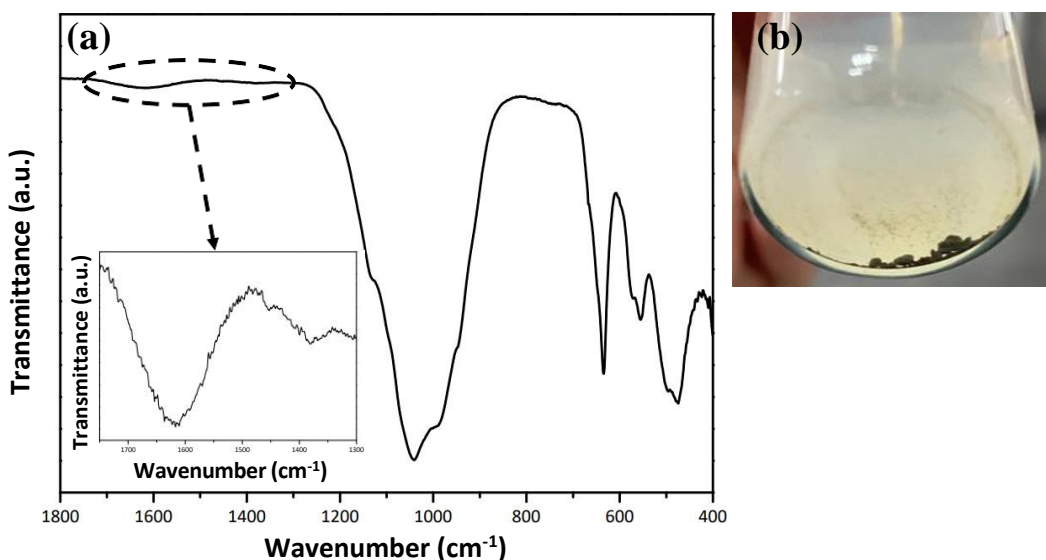


Figure 5.4. The effects of the washing procedure W_2 . (a) The ATR-FTIR spectrum of the particles washed with W_2 (b) Dispersibility of the particles in DIW after washing with W_2 and heat treatment of the HT_2 .

5.3 Effect of Exchange by More Strongly Coordinating Agents on Dispersion

After proving that the heat treatment and the repeated water washing were ineffective to remove organic residues, the third approach, exchanging the residues with more strongly coordinating agents, was investigated. Organic acids, namely ascorbic acid

or citric acid in this study, were expected to replace the EG bound on the LFP surfaces to a certain extent during the reaction. When both acids were used during synthesis (Sample H), particles were dispersible in aqueous environment as given in Figure 5.5 (a). When these particles were subjected to heat treatment (HT₁), neither color change in particles nor oxide peaks in XRD diffractograms were observed (Figure 5.5 (a)). It can be concluded from this observation that using acids protected the LFP particles from oxidation at relatively high temperatures (600 °C) while EG could not. However, hard agglomerates were still present in the SEM micrographs of the heat-treated Sample H_HT₁ as shown in Figure 5.5 (b).

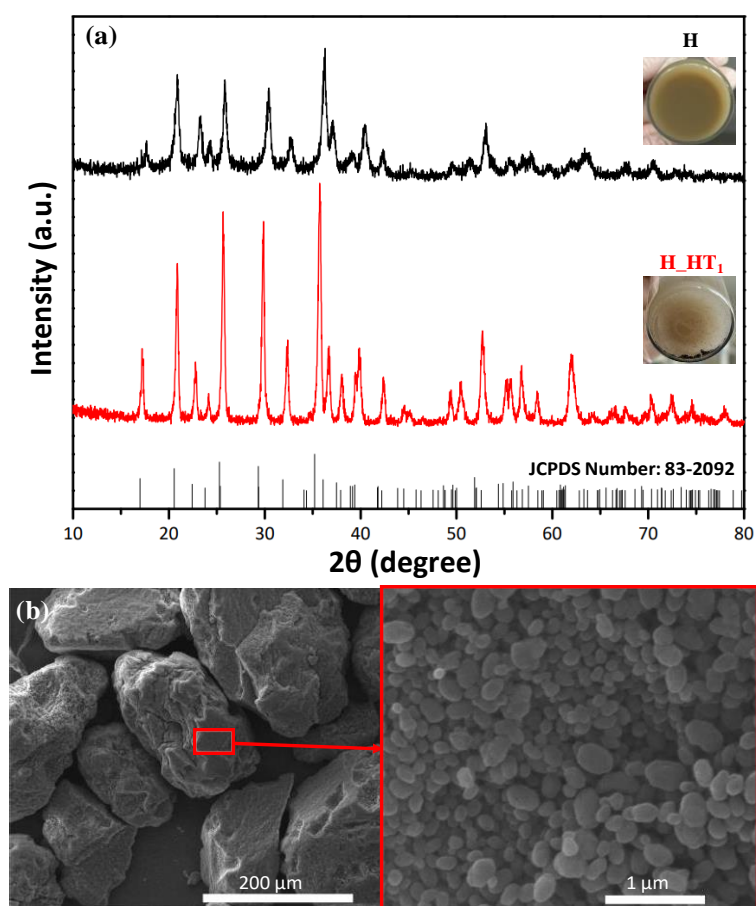


Figure 5.5. The characterization of Sample H before and after exposed to the Heat Treatment Procedure 1. (a) The X-ray diffraction patterns and dispersibility of particles. (b) The FE-SEM micrographs of the Sample H_HT₁.

When the heat treatment 2 (HT₂) was employed to the same particles, no oxide-related peaks were observed in the XRD diffractogram (Figure 5.6 (a)), but more interestingly, hard agglomerates were not observed in the SEM micrographs (Figure 5.6 (c)). The particles were individually present on the micrograph and could be dispersed in water without any obvious sedimentation (Figure 5.6 (a)). It was also interesting to observe the morphology change in particles (Figure 5.6 (b)). When the organic acids were used during particle synthesis, the resulting particles exhibited more spherical shapes rather than the fusiform shape. This morphology change was attributed to the stronger interactions of acids with LFP surfaces compared to the ones of EG.

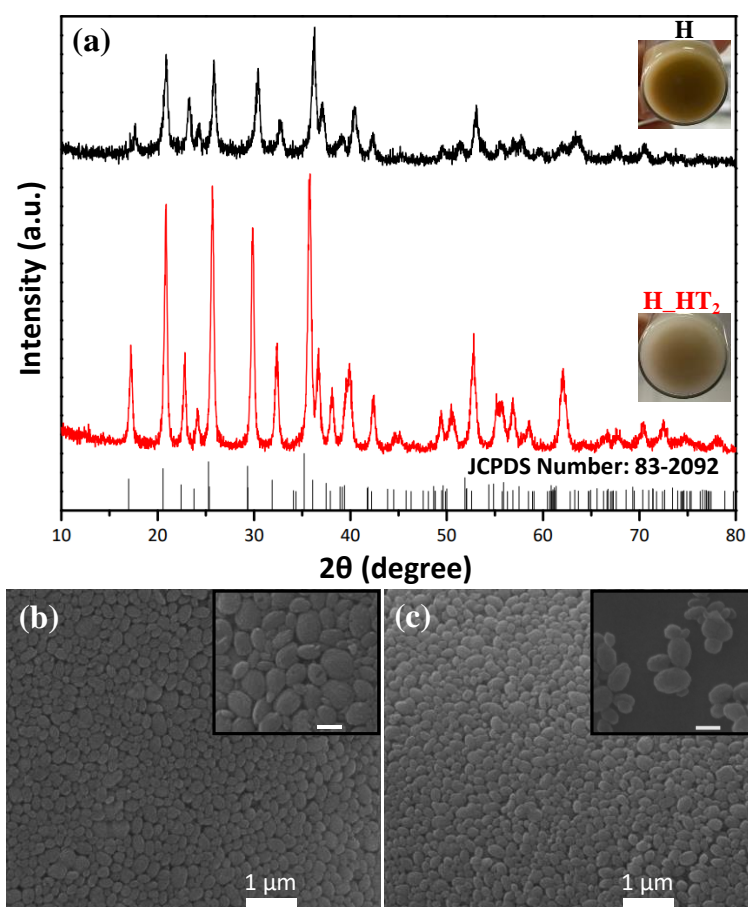


Figure 5.6. The characterization of Sample H before and after exposed to Heat Treatment Procedure 2. (a) The X-ray diffraction patterns and dispersibility in DIW. (b) The FE-SEM micrographs of Sample H (b) before and (c) after the heat treatment. The inset scales are 300 nm.

The ATR-FTIR analysis was conducted before and after the heat treatment to clarify the effect of organic acid addition on the particle surface (Figure 5.7 (a) and (b), respectively). Only intrinsic LFP bands were observed in the fingerprint region between $1300\text{-}400\text{ cm}^{-1}$, indicating the absence of a secondary phase¹²⁵.

The peaks around 1000 cm^{-1} , assigned to the symmetric stretching P-O vibration from the PO_4 polyhedra, was used in the discussions of anti-site defects in LFP crystals¹²⁹. The inhibition of Li^+ transfer in the [010] direction by the iron atoms at the positions of the lithium atoms is called anti-site defect. Anti-site defects were reported to cause low specific charge capacity¹³⁰. Less anti-site defects are expected

in the crystal if this peak shows a red shift. This peak appeared at 988 cm^{-1} in the samples prepared from acid-free unmodified reaction medium, while it shifted to 955 cm^{-1} in the samples synthesized in the presence of organic acids (Figure D.1) indicating less anti-site defects present in the samples with organic acid modified reaction media.

When the transmittance peaks between $1750\text{-}1500\text{ cm}^{-1}$ were deconvoluted on pristine samples (Figure D.2), it was seen that while there was a single peak at 1620 cm^{-1} in the pristine sample (the one synthesized without using organic acids), two peaks, at 1626 cm^{-1} and 1565 cm^{-1} , were present in the sample synthesized with use of organic acids. As a result, the transmittance peak at 1620 cm^{-1} was associated mostly with the EG-residue whereas the one at 1565 cm^{-1} was due to the presence of organic acids. While the former one was assigned to C=C or C=O bonds in the literature, the latter one was assigned to the carboxylate ($-\text{COO}^-$) complexes indicating the potential interactions of acids with LFP particle surface¹³¹⁻¹³⁴.

Lastly, the differences in transmittance peaks between $3650\text{-}3100\text{ cm}^{-1}$, commonly assigned to the O-H stretching mode, was observed in pristine samples¹³⁵. This difference can be attributed to the higher number of hydroxyl groups in the presence of organic acids compared to the case where only EG was used, which can be considered as another indication of the co-existence of acids and EG on the LFP surfaces after washing. As expected, these peaks completely disappeared after heat treatment at high temperatures (Figure 5.7 (b)).

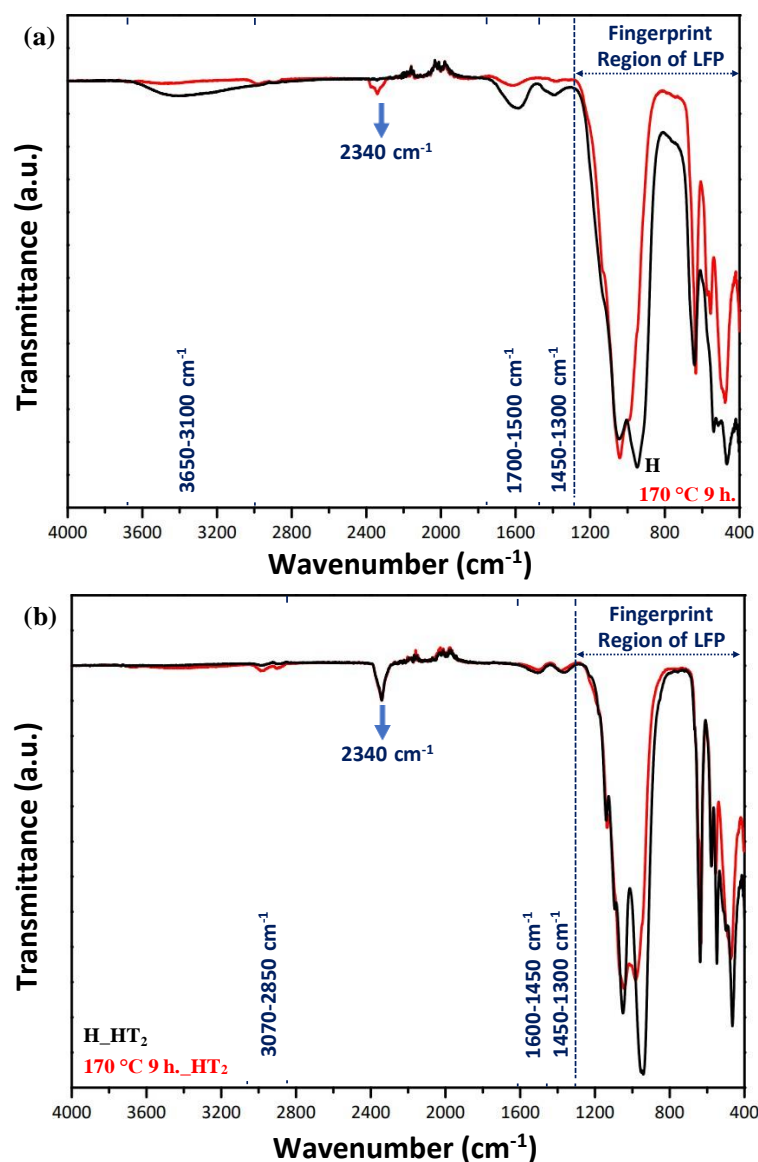


Figure 5.7. The ATR-FTIR spectra of the powders (a) before and (b) after the heat treatments. In both plots, the powders synthesized with and without use of acids were compared.

In conclusion, the FTIR analysis showed that the organic content remaining on LFP surfaces was probably a mixture of EG and organic acids, namely ascorbic and citric acids, that were used during synthesis. The positive interaction of acids and the LFP powders were also evident from the changes in particle morphologies.

In general, post processing studies showed that bridging between the particles stemmed from the organic residues and might lead to the formation of agglomerates during heat treatments, which, in turn, led to random agglomerations and sedimentation when the particles were mixed with water. It was realized that the presence of organics was not always detrimental as in the case of organic acid-containing samples, it was realized that using an additive which could strongly associate with the particle surface was critical to prevent the carbon bridge formation between particles during pyrolysis.

CHAPTER 6

THE SYNTHESIS OF HIERARCHICAL LiFePO_4 PARTICLES WITH CONTROLLED SIZE AND SHAPE

As discussed in the literature review, hierarchical structures provides means for optimization of electrochemical performace and processability. In Chapter 4, it was shown that the polyol method can be used in hierarchical LFP particle synthesis. In addition to the advantages of polyol method in low temperature synthesis with high solids yield, it also allows in situ interventions because of being an open atmosphere synthesis technique, which is a functionality that has never been explored in literature.

Moreover, as discussed in literature review, addition of citric acid (CA) or ascorbic acid (AA) affects the growth directions of LFP crystals during synthesis and consequently results in changes in the shape of LFP particles. It was realized during the studies reported in Chapter 5 that CA and AA, which were added to prevent the hard agglomeration problem occuring after heat treatment, also provided changes in particle shape and size. With all these capabilities, it was hypothesized, in this chapter, that the structure of LFP particles can be designed such that a balance between electrochemical behavior and processability can be found. To this end, AA and CA were added to the reaction medium at different concentrations and in different steps of reaction, and the influence of these parameters on the morphology and dimension of the primary and secondary particles were investigated.

6.1 Addition of Ascorbic Acid

There were examples of AA or CA use in LFP synthesis in literature, however, none of them were conducted in EG-based polyol synthesis conditions. Therefore, first, only AA was added to the reaction medium to understand its effect on LFP particles

synthesized by polyol method using EG (Sample A, described in Table 3.1). The pH of the precursor before the reaction started (Step 3 in Figure 3.3) was measured as 7.10 ± 0.03 . Comparing the precursor prepared without using organic acids, which has the pH of 7.62 ± 0.01 , the pH of precursor suspension decreased with addition of AA to the medium as expected, because the acid dissociation constants (pK_a) of AA are 4.10 and 11.6. The pH of the mother liquor at the end of the synthesis was 5.16 ± 0.02

The XRD patterns of the synthesized particles were presented in Figure 6.1 (a). All the diffraction peaks matched with pure LFP crystals without any indication of secondary phase. When the SEM micrographs were compared (Figure 6.1 (b) and (c)), it was observed that the AA addition did not affect either primary or secondary particle morphologies. In either case, the primary particles were almost spherical while the secondary structure was in fusiform shape. For each case, the primary particles were measured to be about 40 nm from the application of Scherrer equation on the XRD diffractograms and from the SEM micrographs using Image J software (Figure 6.2, Figure E.1 and E.2). The similarity between the results of both measurements proved that the smaller units observed within particles (i.e., primary particles) in SEM micrographs were single crystals. The secondary particle dimensions, on the other hand, were reduced from $400 \pm 65 \times 255 \pm 35$ nm (aspect ratio of 1.57) to $115 \pm 24 \times 75 \pm 16$ nm (aspect ratio of 1.53) when AA was used during reaction (Figure 6.2). As a result, it was concluded that the AA addition did not significantly change the growth behavior of crystals, and thus the shape of the primary particles, as opposed to the case of hydrothermal environment reported in literature¹⁰⁷, but instead it had an impact on the formation kinetics of secondary particles when the reaction was carried on in EG-based polyol reaction conditions. The coexistence of EG and organic acid on LFP particle surfaces after synthesis, as inferred from the FTIR analysis presented in Figure 5.7 (a), also supported this conclusion. Because, if primarily AA was adsorbed on the LFP crystal surfaces, it would have replaced EG molecules and only AA related transmittance peaks would

have been observed. These results showed that AA and EG are competing to adsorb on LFP surfaces.

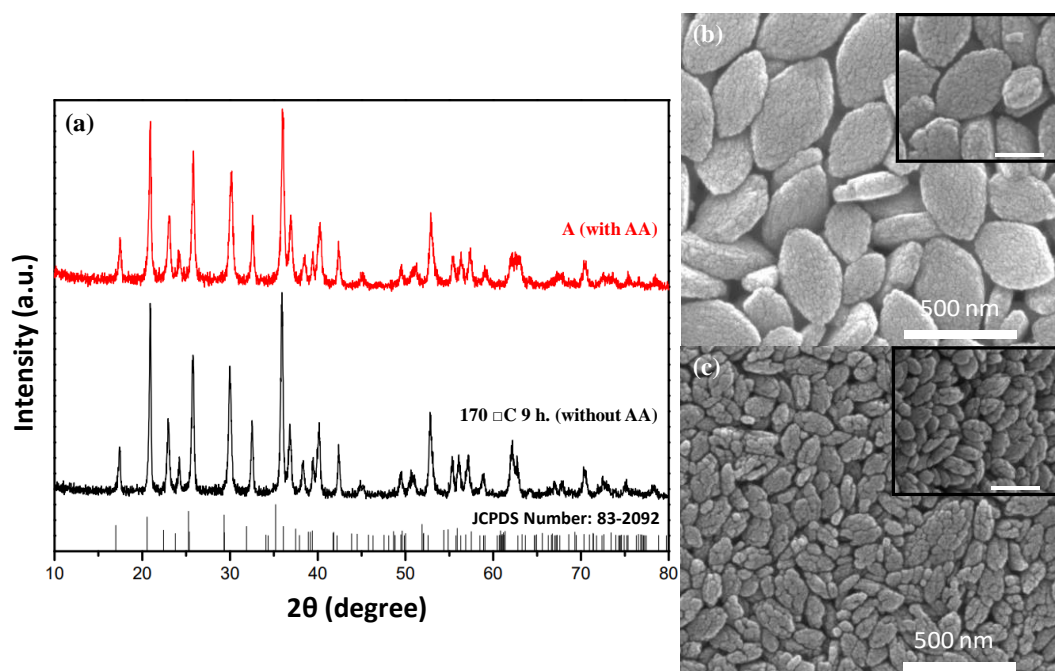


Figure 6.1. Effects of ascorbic acid addition on the LiFePO_4 particles. (a) The X-ray diffraction patterns, and the FE-SEM micrographs of particles synthesized (b) in the absence and (c) presence of the ascorbic acid. The inset scales are 200 nm.

The BET specific surface area of the small fusiforms, which were obtained when AA was used in the synthesis, was measured as $43 \text{ m}^2/\text{g}$. Comparing to the BET surface area of $25 \text{ m}^2/\text{g}$ obtained when organic acids were not used, the larger surface area confirmed the decrease in secondary particle size with AA addition, although the primary particle sizes were similar¹³⁶.

In the SEM micrographs, particles seemed to be individually present in either case. When the particles were mixed into DIW, they did not sediment instantaneously. After a week of observation, the particles synthesized without use of organic acids sedimented more than the ones synthesized in the presence of AA. This behavior was attributed to the size difference, because smaller particles were expected to sediment in longer times as expected from the Stokes' Law¹³⁷.







	170 °C 9 h.	A
Start		
After 1 Day		
After 1 Week		
Primary Particle Size* (nm)	41 ± 12	43 ± 14
Primary Particle Size** (nm)	40	39
Secondary Particle Size (nm)	400±65 × 255±35	115±24 × 75±16

Figure 6.2. Comparison of the sedimentation behavior and the particle dimensions of synthesized particles with and without use of ascorbic acid. * shows measured primary size from the SEM micrographs using ImageJ software. 200 – 250 particles were measured for each sample. For the secondary particle size measurements, about 3000 particles were measured. ** shows the size measurements obtained using Scherrer equation.

One of the advantages of synthesizing dispersible, individual electroactive particles is the potential to increase their tap density. Here, the reference LFP powder and two different synthesized LFP particles were compared in terms of their tap densities. As observed in Figure 6.3, the tap density of the reference powder was $0.84 \pm 0.09 \text{ g/cm}^3$, this value increased to $0.99 \pm 0.04 \text{ g/cm}^3$ when individual particles were used, and the value was $1.42 \pm 0.03 \text{ g/cm}^3$ for the Sample A. It was reasonable to relate the large deviation in the tap density values to the agglomeration state of reference powder, because larger agglomerates might not always locate at their optimum positions during packing, i.e., obtaining a close packing is more of a statistical event with significant limitations. Individual particles, on the other hand, could pack densely, because, when the individual particles were compared to the mostly

agglomerated powders, the individual particles would have much lower average effective size, they would move with more ease when tapped, and it will be statistically more possible to find empty spots and locate themselves during packing. Similarly, particles with broader size distribution or elongated shape are expected to exhibit higher packing fraction. In this study, smaller particles with fusiform shape resulted in much better packing, thus higher tap density. The packing fraction was calculated as 0.28 for large fusiforms, 0.39 for small fusiforms and 0.23 for reference powder (True density of LFP is 3.60 g/cm^3)¹³⁸.

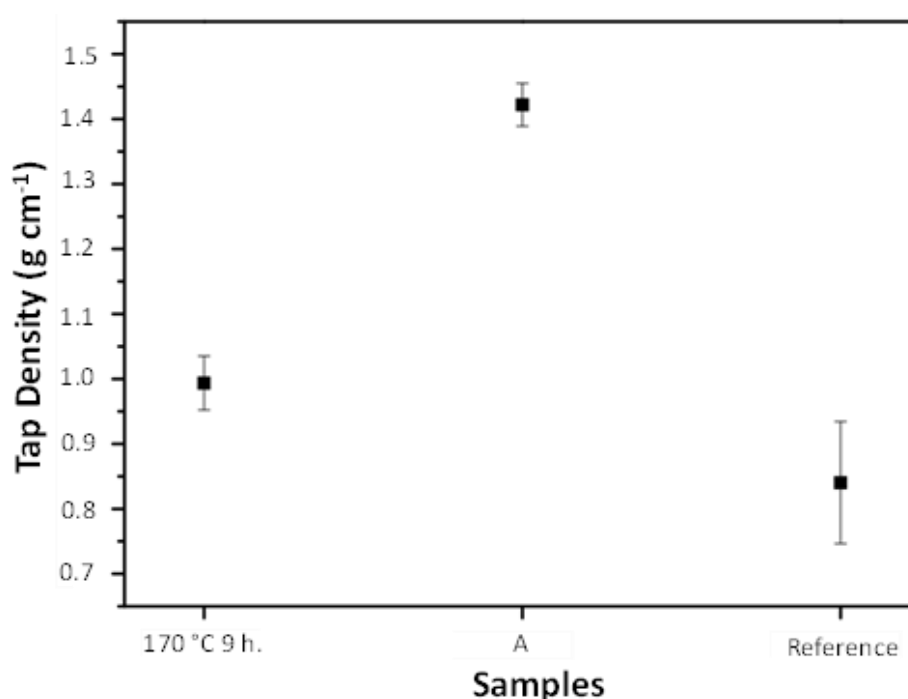


Figure 6.3. Tap densities of 170 °C 9 h. (large fusiforms), A (small fusiforms) and reference powders. Tap density of synthesized particles was higher than the reference powder.

There is an inverse relation between the packing fraction and the suspension viscosity even though it is not always linear¹³⁹. In order to demonstrate the processing performance of the synthesized particles, aqueous suspensions of synthesized and reference powders with particle loading of 40 wt.% were prepared and their rheological behavior were investigated (Figure 6.4).

The suspension of reference powder had a low shear viscosity of about 200 Pa·s and exhibited shear thinning behavior proving the crowdedness of the suspension. The almost solid form of the reference sample, shown in Figure 6.4 (d), indicated that the maximum amount of solid loading had already been achieved, therefore the particles and the hard agglomerates were interacting at the level that limited the flow. Considering the loose packing of agglomerated powders, in order to move such a structure with shear effect, there might be a need for good amount of force which corresponds to higher viscosities at low shear rates. As this structure started to move, it was expected to be broken down, which would lead to lower viscosities with increasing shear rate, i.e., shear thinning behavior¹⁴⁰.

When the individual particles were used, the rheological behavior turned to more Newtonian one for the suspensions of both synthesized powder, indicating that the powders could move almost freely without any significant obstacle in suspension regardless of the applied shear rate. The average viscosity of suspensions prepared from particles synthesized without using organic acid was about 6.3 mPa·s whereas the one prepared from particles synthesized using AA was about 3.5 mPa·s. These values were 3-4 orders of magnitude lower than the reference powder. The difference in flow behavior could be visualized from the images presented in Figure 6.4 (b-d). While the suspension prepared from reference LFP powder did not flow and behaved like almost a solid, others flowed with ease and behaved as a fluid. When the suspension viscosities of synthesized particles were compared, it was realized that the particles synthesized using AA exhibited much lower suspension viscosity than the other one despite its smaller secondary particle size. This behavior might be related to the strength of interparticle interactions, which is beyond the scope of this study.

Using electroactive particle suspensions with such a low viscosity will decrease the power requirement in electrode preparation. Moreover, since the powders were much more homogeneously distributed in suspensions compared to the reference powder case, more uniform electrodes can be produced. Furthermore, 40 wt.% particle loading was almost the maximum amount of powder that could be loaded to this

suspension as it already behaved as a solid at this powder concentration; however, considering fluidity of the suspensions prepared using the powder synthesized in this study, more electroactive particles could be loaded to the same volume, therefore, the volumetric energy density of the electrodes would be expected to be high.

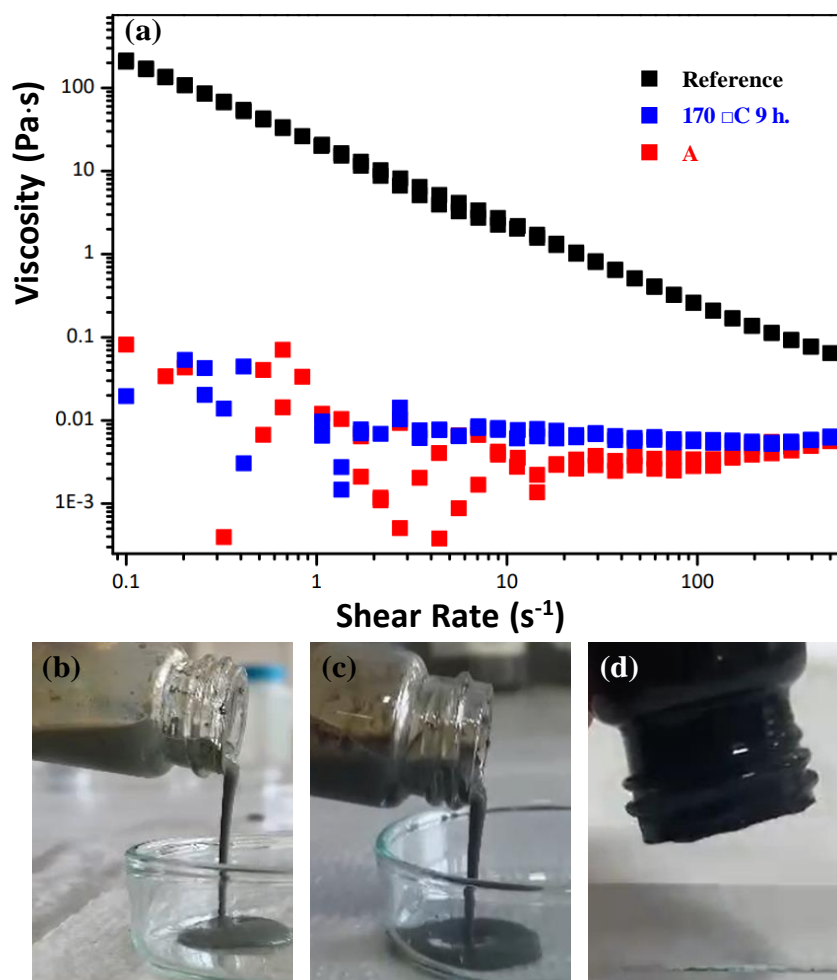


Figure 6.4. (a) Rheological behavior of the synthesized and the reference powders. Images showing the flow behavior of (b) of Sample A, (c) Sample 170 °C 9 h, and (d) the reference powder.

6.2 Addition of Citric Acid

Because the effects of AA addition on LFP particle characteristics was dramatically different when EG-based polyol method was used instead of hydrothermal method,

the effect of CA addition was also separately investigated (Sample B described in Table 3.1).

Previous experiments showed that the reaction media changed from the dark, viscous precursor to a lighter-colored, lower-viscosity suspension when LFP particles were formed. In previous experiments, this transition occurred when temperature reached to 170 °C and reaction continued for 2 hours, however, this transition occurred in much longer times when CA was used in synthesis, so the reaction was carried out for 18 hours to ensure crystal LFP particle formation.

The XRD patterns of the synthesized particles with addition of CA in Figure 6.5 (a) showed that pure LFP crystals could be formed. The broadening in peaks indicated that the crystallite sizes were very small despite the prolonged reaction duration. Compared to Sample A, significant broadening observed indicating that the crystallites are even smaller than 40 nm.

The synthesized particles had hierarchical structure as in the case of Sample A, but the secondary particle morphology changed to almost perfectly spherical flakes, what we called a pancake morphology (Figure 6.5 (b)). Although the same experimental steps were followed, the particles with same morphology could not be reproduced.

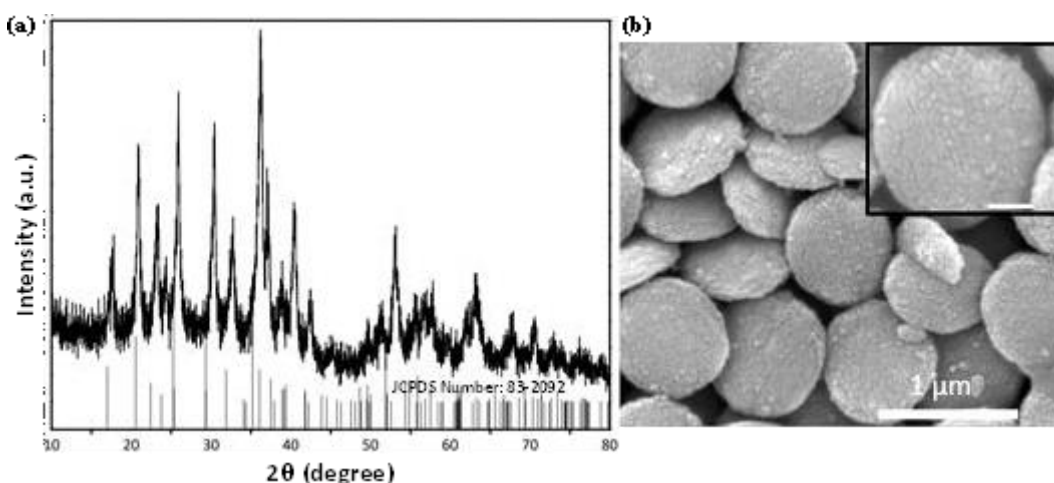


Figure 6.5. Effects of using citric acid during LiFePO_4 synthesis. (a) X-ray diffraction pattern and the (b) FE-SEM micrographs of Sample B.

6.3 Combined Addition of Ascorbic Acid and Citric Acid

In the previous experiments, it was realized that AA affected only the size of secondary particles whereas CA had an effect also on its morphology under EG-based polyol synthesis conditions. In order to combine these two effects, both acids were used in the synthesis, however half of the original amount of each acid was used to keep the total acid content constant.

Firstly, both acids were added simultaneously in solid state while mixing all precursors (Sample C described in Table 3.1). The pH value of the precursor prior to synthesis (Step 3 in Figure 3.3) was measured as 6.47 ± 0.01 . When compared to Sample A, the pH of the precursor suspension of Sample C had a much lower pH value as expected, because at this pH value is above acid dissociation constants of three carboxyl groups of CA (pK_a values of CA are 3.13, 4.76 and 6.40) whereas only the suspension pH value is between the first and second dissociation constants of AA (K_a values of AA are 4.17 and 11.6). The pH of the mother liquor at the end of the synthesis was 6.32 ± 0.03 for Sample C. The XRD analysis showed that pure LFP crystals were synthesized (Figure 6.6(a)). The significant broadening in diffractograms attributed to the smaller size of the primary crystallites and calculated as 28 nm using Scherrer equation (Figure 6.7). Comparing this value with the one obtained from the particle synthesized using sole AA or without using any organic acids (40 nm), the primary particle size decreased. It could be realized from SEM images at high magnification in Figure 6.6 (b) that the morphology of the primary particles also changed from spherical to more elongated structures. The dimensions of primary particles were measured as 50 ± 17 nm \times 20 ± 6 nm. When secondary particles were analyzed and compared with the particles synthesized without using organic acids, fusiform morphology of the particles altered to ellipsoid morphology while preserving its aspect ratio (1.5), but the overall dimensions of particles slightly decreased to 330 ± 79 nm \times 220 ± 63 nm (Figure E.3).

Since the peak broadening in the XRD patterns were both observed in Sample B and Sample C, where CA were used, in order to understand the effect of AA addition on

the primary crystals' nucleation and growth, another experiment was designed in which the AA was added into the reaction medium little after crystallization started, precisely 15 minutes after the temperature reached to 170 °C (Sample D). The pH values of the precursor (Step 3 in Figure 3.3) and mother liquor at the end of the synthesis for Sample D were 6.69 ± 0.02 and 6.32 ± 0.04 , respectively. The synthesized particles have very similar secondary particle dimensions with relatively higher aspect ratio (330 ± 76 nm \times 200 ± 56 nm, aspect ratio of 1.65), yet primary particles were much smaller and spherical (crystallite size was calculated as 19 nm from Scherrer equation and measured as 22 ± 6 nm from SEM micrographs (Figure E.4)). It was interesting to realize that being able to control particle features at almost every dimension by enabling some interventions to the reaction medium.

The BET specific surface area of the Sample C and Sample D were measured as 23 and 46 m²/g, respectively. The difference between the two samples was associated with the difference in shape and size between primary particles. Even though the secondary particles of both samples had similar dimensions, the primaries of the LFP particles of Sample D were much smaller which led to the increase in the BET surface area.

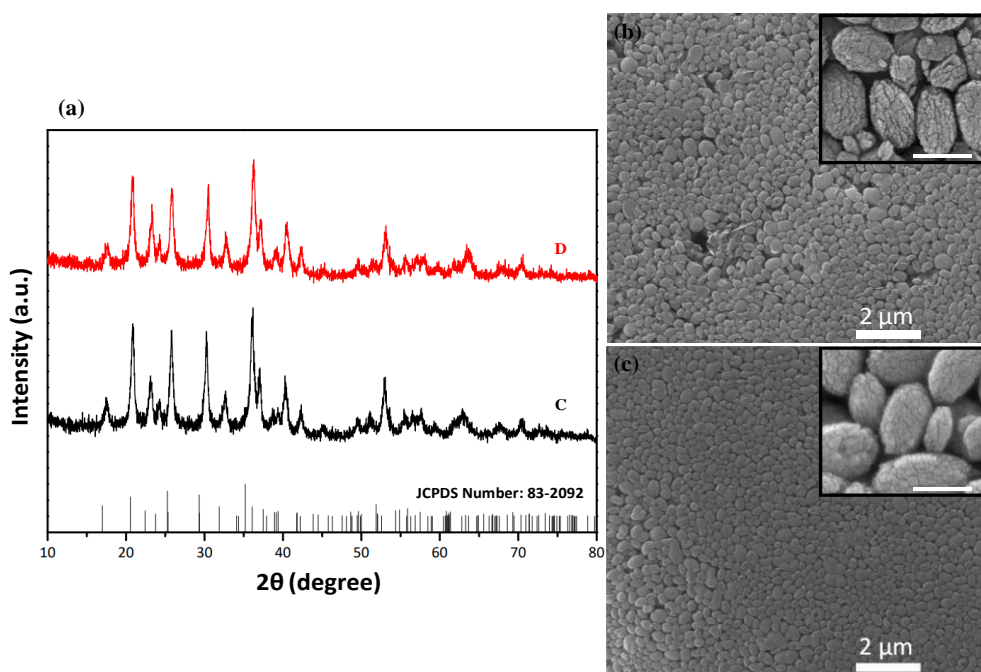


Figure 6.6. Effect of combined addition of citric acid and ascorbic acid to the reaction medium during synthesis of LiFePO_4 . For Sample C, ascorbic acid was added with citric acid while for Sample D, it was added 15 minutes after the reaction temperature reached to $170\text{ }^\circ\text{C}$. (a) X-ray diffraction patterns and FE-SEM micrographs (b) of Sample C and Sample D. The inset scales are 300 nm.

From SEM micrographs, it was obvious that the particles were individually present, thus expected to be dispersible. Together with the similarity of the secondary particle characteristics of Sample C and D, it was not surprising to observe similar sedimentation behavior in both samples (Figure 6.7). Even after a week, the particles did not completely sediment, proving their stability and dispersibility.







	C	D
Start		
After 1 Day		
After 1 Week		
Primary Particle Size* (nm)	50±17 × 20±6	22±6
Primary Particle Size** (nm)	28	19
Secondary Particle Size (nm)	330±79 × 220±63	330±76 × 200±56

Figure 6.7. Comparison of the sedimentation behavior and the particle dimensions of synthesized particles with combined addition of ascorbic acid and citric acid. * shows measured primary size from the SEM micrographs using ImageJ software. 200 – 300 particles were measured for each sample. For the secondary particle size measurements, about 3000 particles were measured. ** shows the size measurements obtained using Scherrer equation.

Similar size and geometry of the particles resulted in similar tap densities. The tap densities were measured as 1.83 ± 0.10 and $1.98 \text{ g/cm}^3 \pm 0.10 \text{ g/cm}^3$ for Sample C and Sample D, respectively (Figure 6.8). When compared to the reported nanoparticle tap densities (typically less than 1 g/cm^{114}) and the tap density of reference powder used in this study ($0.84 \pm 0.09 \text{ g/cm}^3$), the tap densities obtained with Sample C and D almost doubled these values, and to the best of our knowledge, these values are the highest tap densities reported for the LFP particles in literature. The ellipsoid shape of the particles was considered to be effective to obtain better packing due to larger number of contact points between particles.

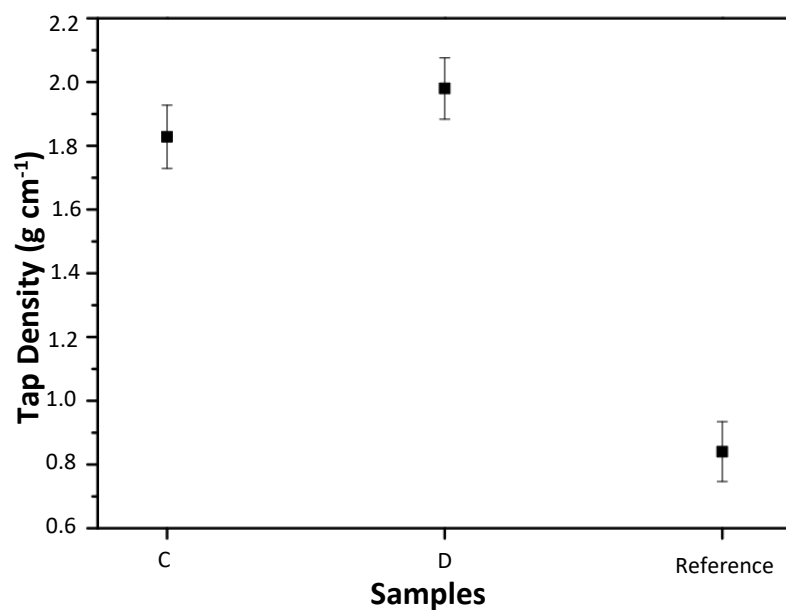


Figure 6.8. The tap density comparison of the Sample C, the Sample D and the reference powder.

The rheological behavior of aqueous suspensions of synthesized and the reference powders with particle loading of 40 wt.% were investigated (Figure 6.9) to demonstrate processing performance. The synthesized particles exhibited almost Newtonian behavior. The average viscosity of suspension prepared from Sample C was about 3.3 mPa·s, while this value was 2.7 mPa·s for Sample D.

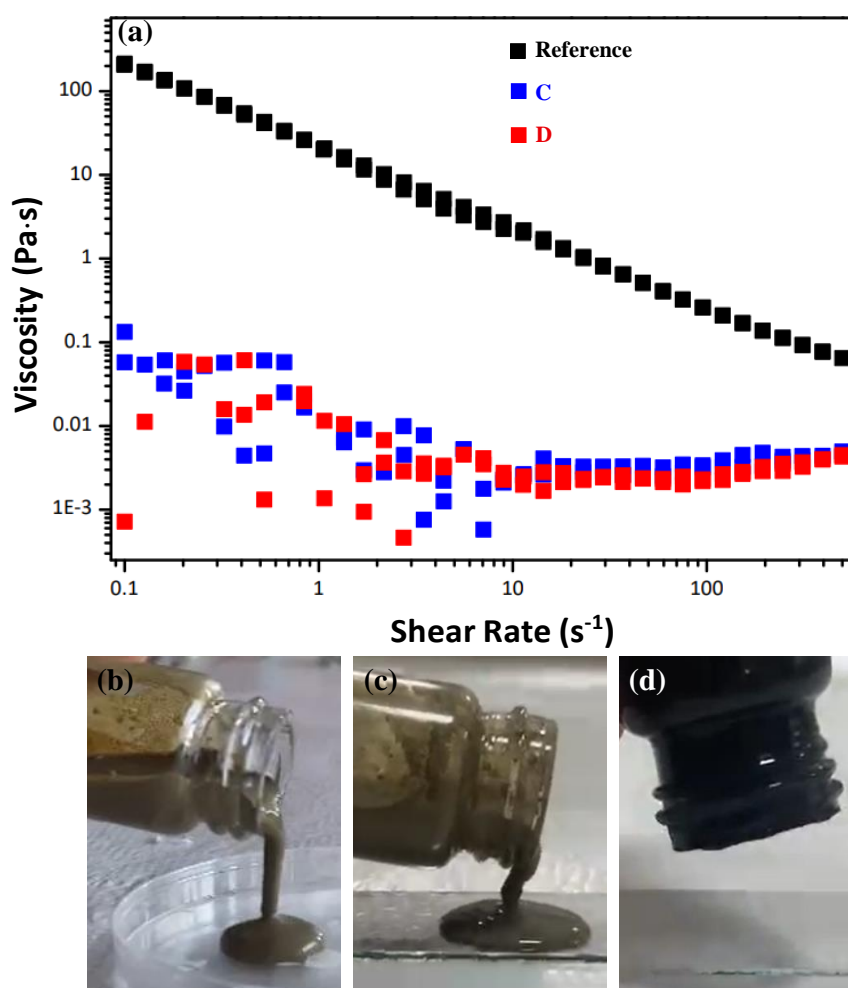


Figure 6.9. (a) The rheological behavior of the suspensions prepared from synthesized (Sample C and Sample D) and the reference powders. Images showing the flow behavior of (b) the Sample C, the Sample D, and the reference powder suspensions.

Because the highest tap density values were measured for Sample D, electrochemical behavior of these particles was tested with 3-electrode set up in aqueous electrolyte (Figure 6.10(b)). Unexpectedly low discharge capacities were recorded. The values started from few mAh/g and increased up to 27 mAh/g after 10 cycles. Considering the very small crystallite size of the powders and all the organic residues remained on LFP particles after synthesis, the powders were subjected to the heat treatment (HT₂).

In XRD patterns, no secondary phase formation was observed after the heat treatment (Figure 6.10(a)). The FWHM of the peaks decreased and the crystallite size was calculated as 30 nm, indicating the growth of primary particles during heat treatment. The change in the primary particle size can also be realized in SEM micrographs given in Figure 6.10 (c). The secondary primary particle morphology, on the other hand, preserved even after the crystal growth during heat treatment.

As a result of heat-treatment, the electrochemical behavior of particles could be improved. Their specific discharge capacity values started from 43 mAh/g and almost leveled off around 74 mAh/g after 10 cycles. It should be noted that the specific discharge capacity values measured with the current 3-electrode set up in aqueous electrolyte were dramatically lower than the values that were measured with a half cell in organic electrolyte. As a reference, the synthesized powders without organic acid (170 °C 9 h.) were analyzed with both setups, and the initial discharge capacity of 121 mAh/g was recorded in organic electrolyte set-up was 46 mAh/g when measured in aqueous electrolyte setup (Figure F.1). Based on this reference, the discharge capacity of the heat-treated Sample D would be comparable with Sample 170 °C 9 h. and it could be predicted that the specific discharge capacity in organic electrolyte was higher than 121 mAh/g. This value was close to reported values for the hierarchical LFP particles¹⁰⁸⁻¹¹³.

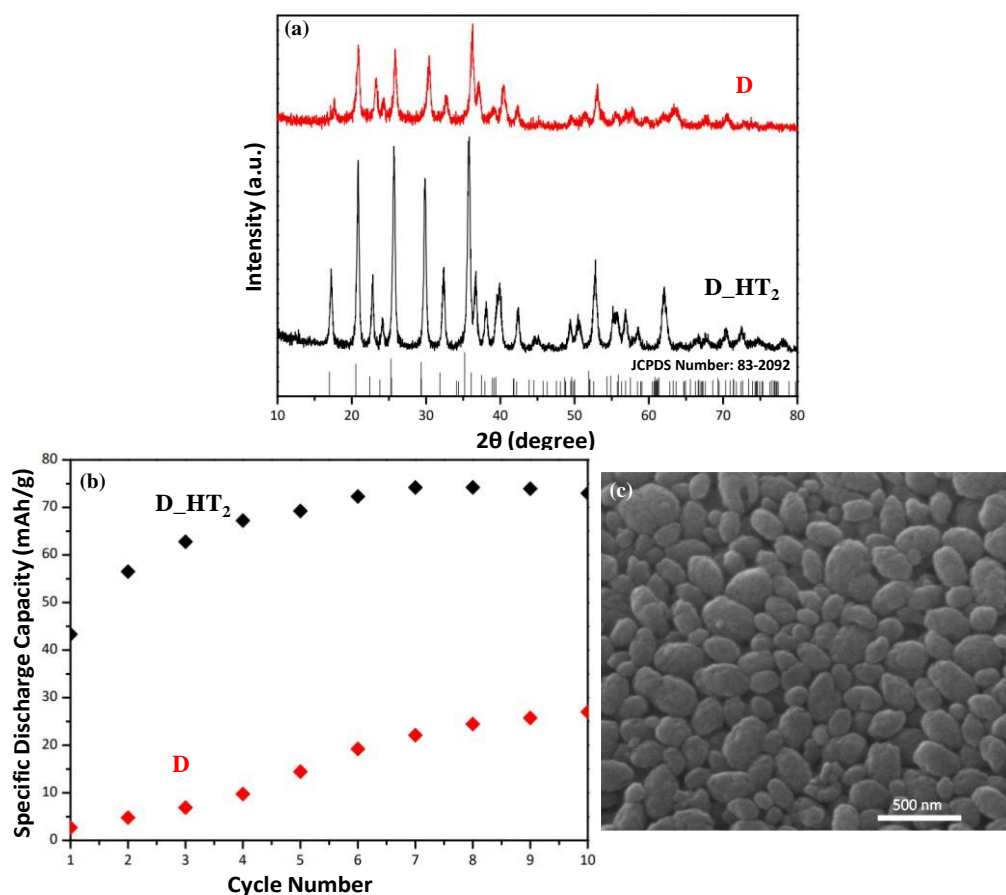


Figure 6.10. Effect of Heat Treatment Procedure 2 on Sample D. (a) The X-ray diffraction patterns, (b) The specific discharge capacities in 3-electrode aqueous setup of Samples D and Sample D_{HT2}. (c) The FE-SEM micrograph of D_{HT2}.

6.4 Effects of Citric Acid Concentration

The experiments with the combination of CA and AA showed that the addition of AA before or after crystallization affects the morphology and size of the primary particles. In order to clarify the effect of CA, the procedure used in preparation of Sample D was followed by doubling the amount of CA and labeled as Sample E. The reaction time was extended to 9 hours since color change indicating crystallization did not occur after 2 hours. The pH value of the precursor (Step 3 in Figure 3.3) was measured as 5.84 ± 0.02 . Among the pH values of the precursors of all samples, the lowest pH was obtained in this sample. This was an expected

decrease in pH, because in this sample the highest amount of organic acid was used. The pH of the mother liquor at the end of the synthesis was 6.65 ± 0.03 .

Increasing CA concentration did not affect the purity of LFP particles based on XRD analysis (Figure 6.11 (a)). It was observed from the SEM micrographs in Figure 6.11 that the particles grew in one specific direction and their dimensions were measured as $600 \pm 76 \text{ nm} \times 235 \pm 48 \text{ nm}$ corresponding to an aspect ratio of 2.55. The primary particles were spherical and crystallite size were measured as 19 nm (from application of Scherrer equation and $20 \pm 5 \text{ nm}$ from the SEM micrographs (Figure E.5)), which were very similar to the primary particle characteristics of Sample D. As a result, it can be concluded that adding CA during preparation of precursor before crystallization was critical to control secondary particle characteristics, while adding AA 15 minutes after all mother liquor ingredients were combined and reaction temperature of $170 \text{ }^\circ\text{C}$ was reached had a significant influence of the primary particle size and morphology. This conclusion was particularly important as it showed that the open atmosphere synthesis approach allowed one to intervene with the reaction and these interventions conveniently facilitated design of particle characteristics during synthesis.

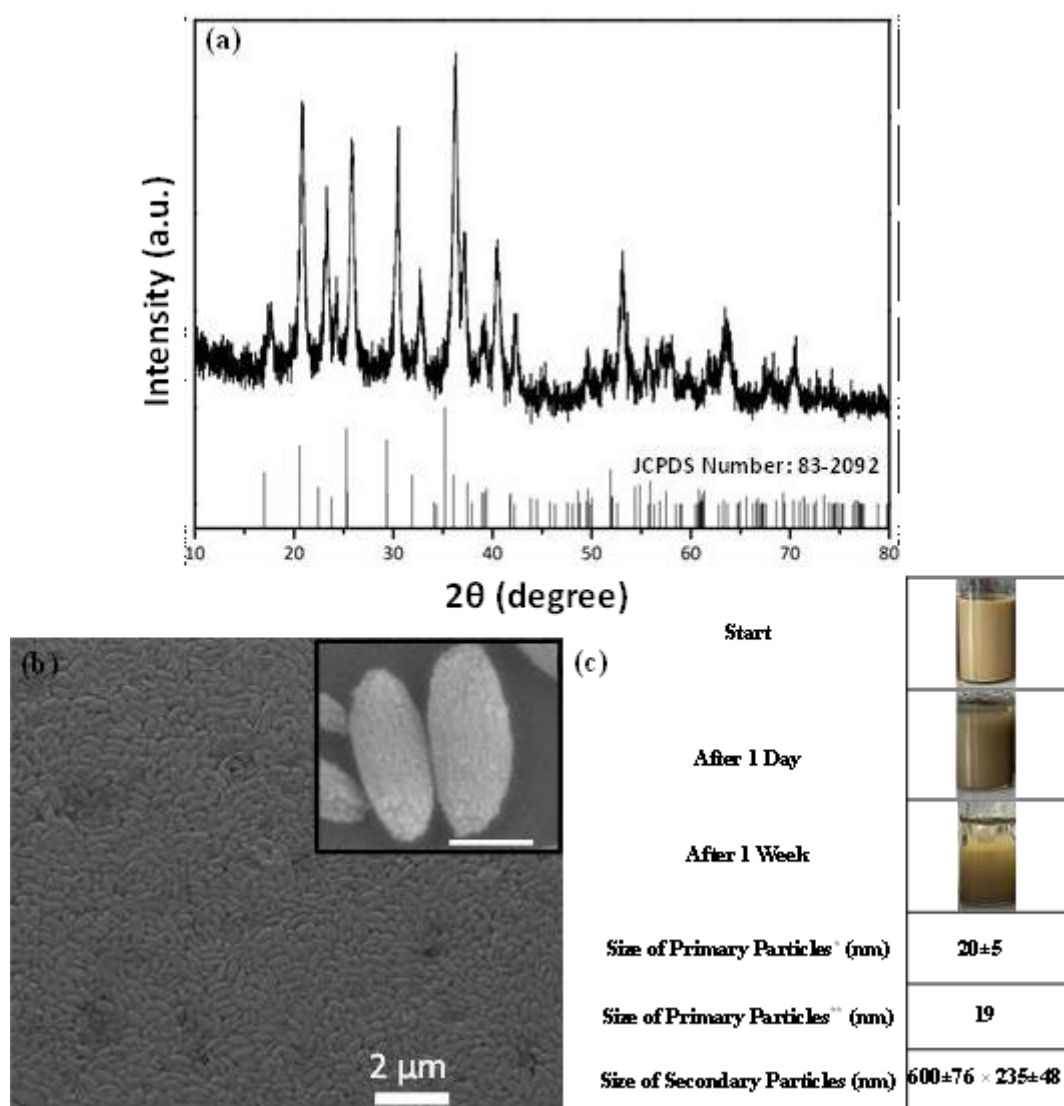


Figure 6.11. The effect of doubled citric acid concentration on the synthesized particle characteristics. (a) The X-ray diffraction patterns, (b) FE-SEM micrographs, and (c) The sedimentation behavior and particle size measurements of Sample E. Inset scale of FE-SEM micrograph is 300 nm. * shows measured primary size from the SEM micrographs using ImageJ software. 200 particles were measured for Sample E. ** shows the crystallite sizes obtained by application of Scherrer equation. 3000 particles were measured for secondary particle size of both samples.

The BET specific surface area of the Sample E was measured as $35 \text{ m}^2/\text{g}$. Sample E had a lower specific surface area compared to Sample D. Although the specific surface area is independent of the aspect ratio, it has an inverse relationship with the particle size, the specific surface area decreases as the particle size increases¹⁴¹. The morphology and sizes of the primary particles of Sample D and Sample E were similar, while the larger secondary particle size of Sample E resulted in a lower specific surface.

When the sedimentation behavior of Sample E was examined, it did not significantly differ from the case of Sample D despite its relatively larger size and higher aspect ratio. However, probably because of the large particle size and high aspect ratio, the tap density decreased to 0.78 ± 0.05 , which was comparable with the reference powder (Figure 6.12). The packing fraction was calculated as 0.22 for Sample E.

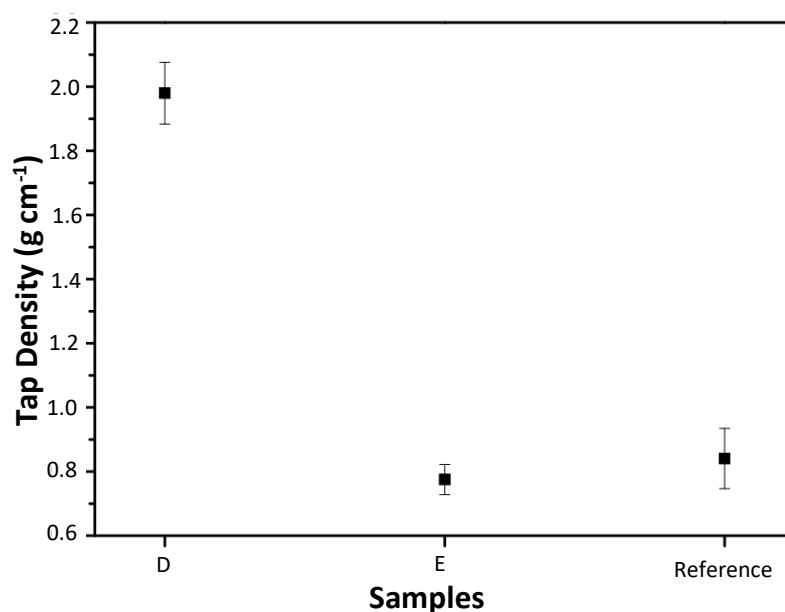


Figure 6.12. Tap density comparison of the Sample C, the Sample D and the reference powder.

Aqueous suspensions of Sample D and Sample E were analyzed in terms of their rheological behavior and compared to one of the reference powder (Figure 6.13). The rheological behaviors of synthesized particles were almost Newtonian. The average viscosity of suspension prepared from Sample D was about $2.7 \text{ mPa}\cdot\text{s}$, while

this value was 5.3 mPa·s for Sample E. The higher average viscosity of the sample with higher aspect ratio was explained by Simha's relation¹⁴². Particles with higher aspect ratio showed higher viscosity compared to the particles with lower aspect ratio because as the aspect ratio of the particles increases, the flow lines of the water flowing around the particles deviate more. Another remarkable result was that the viscosities of the particles were similar at high shear rates. This was explained by alignment of the particles to the flow direction. The particle with high aspect ratio was aligned more to the flow direction of water when the shear rate is increased.

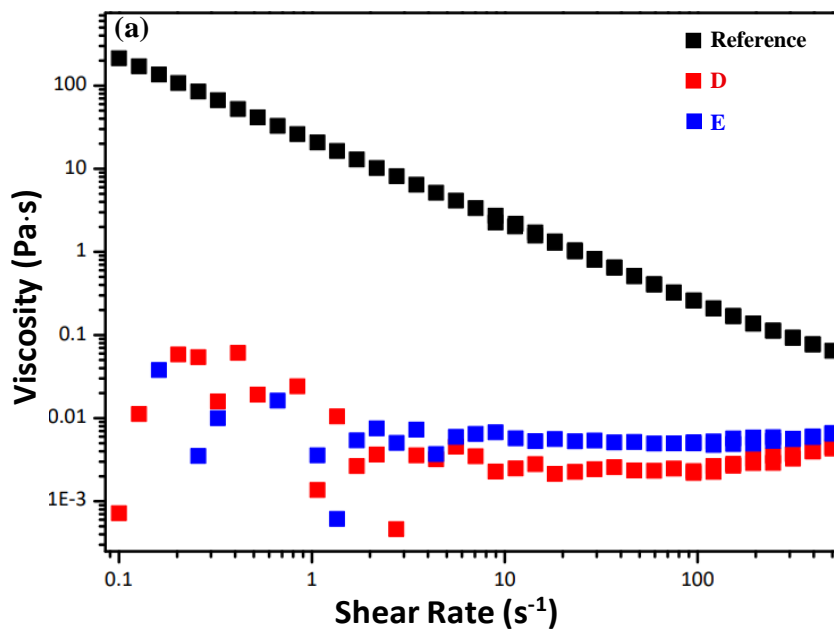


Figure 6.13. (a) The rheological behavior of aqueous suspensions of Sample D, Sample E and their comparison with the one of the reference powders. The images showing the flow behavior of the suspensions prepared from (b) the Sample D, (c) the Sample E, and (d) the reference powder.

6.5 Addition Sequence of Citric Acid During Precursor Preparation

The importance of dissolving the reagents in the synthesis of fusiform shaped LFP particles without using organic acids was discussed in Chapter 4. Since CA is known to be a strong chelating agent, it was predicted that how much CA was dissolved in which reagent before the formation of Fe-P associations might have an effect in the physical characteristics of the synthesized particles. It was also expected that this additional set might bring a remedy for the reproducibility problem observed in Sample B. For this reason, four different paths were followed to dissolve CA as described in Table 3.2. Before discussing the effect of the CA feeding sequence on the particle shape, it should be noted that in all these additional experiments AA was added to the reaction medium in solid form 15 minutes after reaching the synthesis temperature.

The crystal structure, primary and secondary particle sizes (Figure E.6, E.7 and E.8), morphology, dispersibility (Figure 6.14) and the tap density of these samples (Sample F, G and H) did not differ significantly when compared to Sample D (Figure 6.15). The high solubility of CA in DIW could be the reason for these observations. Keeping in mind that the solubility of the CA in DIW at 30 °C and 40 °C is 64.3 wt.% and 68.6 wt.%, respectively¹⁴³. It can be inferred that 0.360 g of CA can dissolve readily in 3.55 g of water coming from the iron and phosphate sources and addition of extra water. Therefore, CA was expected to be completely soluble in each scenario and that could explain the similarity of the results while showing its robustness.

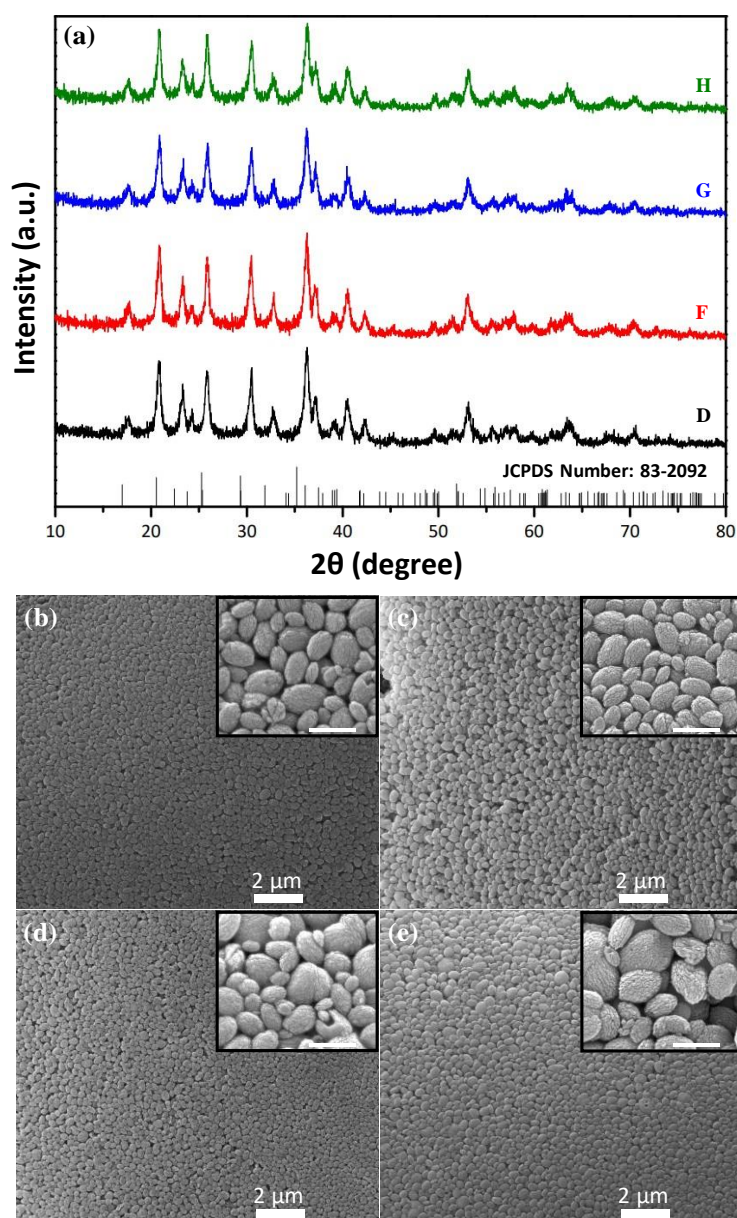


Figure 6.14. The effect of feeding sequence of citric acid on the synthesized particle characteristics. (a) The X-ray diffraction patterns and the FE-SEM micrograph of (b) the Sample D, (c) the Sample F, (d) the Sample G, and (e) the Sample H. The inset scales are 500 nm.

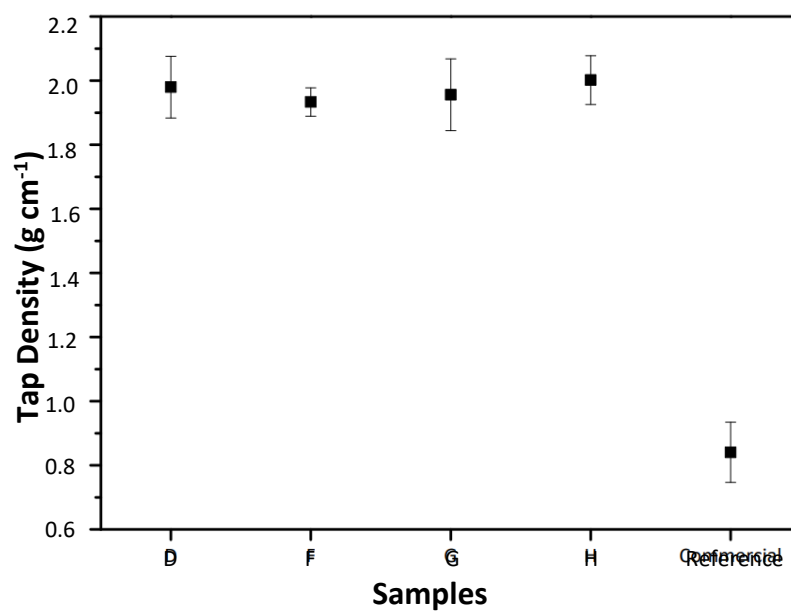


Figure 6.15. The tap densities of the samples D, F, G, H, and the reference powder.

The properties of LFP particles synthesized in this study were summarized in Table 6.1.

Table 6.1 Properties of synthesized LiFePO₄ particles in this thesis

	<i>170 °C 9 h.</i>	<i>A</i>	<i>C</i>	<i>D</i>	<i>E</i>
Primary Particle Size* (nm)	41±12	43±14	50±17 × 20±6	22±6	20±5
Primary Particle Size** (nm)	40	39	28	19	19
Primary Particle Shape	Spherical	Spherical	Elongated Structure	Spherical	Spherical
Secondary Particle Size (nm)	400±65×255±35	115±24 × 75±16	330±79 × 220±63	330±76 × 200±56	600±76 × 235±48
Secondary Particle Shape	Fusiform	Fusiform	Ellipsoid	Ellipsoid	Ellipsoid
Aspect Ratio	1.57	1.53	1.50	1.65	2.55
BET Specific Surface Area (m ² /g)	25	43	23	46	35
Tap Density (g/cm)	0.99±0.04	1.42±0.03	1.83±0.10	1.98±0.10	0.78±0.05
Average Suspension Viscosity (mPa·s) ^{***}	6.3	3.5	3.3	2.7	5.3

* shows measured primary particle size from the SEM micrographs using ImageJ software.

** shows calculated primary particle size using Scherrer equation.

*** Rheological behavior of the suspensions investigated with LFP concentrations of 40 wt. % as a function of shear rate.

CHAPTER 7

CONCLUSIONS

Synthesis of scalable and high yield electroactive materials with controlled size and morphology is a challenge. The synthesis route, dissolution of reagents and surfactants used in synthesis play a role for designing the size and morphology of the synthesized particles. In this thesis, the synthesis of LFP particles with controlled size and morphology and with high yield using polyol route in ethylene glycol (EG) were reported. Ascorbic acid (AA) and citric acid (CA) were used as organic acid to tune the size and morphology of the synthesized particles at different levels. The effect of particle morphology on electrochemical behavior and tap density was studied. The dispersibility and the rheological behavior of suspensions prepared from synthesized powder were also investigated.

LFP particles were synthesized using a scalable polyol method. EG was used as the reaction medium. The amount of water was tuned to increase reaction yield and boiling point of EG. The effect of temperature on crystallization of LFP particles was studied. Dispersible, hierarchical fusiform-shaped particles with a yield of 97% were synthesized after 9 hours of ageing at 170 °C. This temperature is the lowest temperature recorded for LFP synthesis using the polyol route in the literature. The initial discharge capacity of as-synthesized particles was measured as 121 mAh/g in organic electrolyte system although no heat treatment, doping or coating was applied. It was realized that the synthesized particles contained EG-based mother liquor residues.

Heat-treatment, additional washing steps with water and exchange of EG with organic acids were applied to eliminate or minimize the remaining EG. The heat treatment and additional washing steps with water were not effective to obtain dispersible particles because of the interparticle bridging resulting from organic

residues. However, the association of AA and CA with the particle surface during synthesis prevented bridge formation between particles and as a result, dispersible LFP particles could be obtained even after proper treatment at elevated temperatures.

Organic acids, namely CA and AA, were used to tune and design the size and shape of LFP particles. The addition of AA led to a decrease in the secondary particle size while preserving its shape, but it did not affect have any effect on the primary particle size. The synthesized particles had fusiform-shape and were dispersible. As a result, a tap density value as high as 1.42 ± 0.04 g/cm³ was obtained. Tap density values of the synthesized particles were higher than the reference powder since the individual particles could be packed densely. The suspensions of synthesized powders exhibited a liquid-like Newtonian behavior and had an average viscosity of about 3.5 mPa·s for suspension with solids loading of 40 wt.%. The average viscosity values of synthesized powders were 3-4 orders of magnitude lower than the low-shear rate viscosity of suspension prepared from the reference powder.

The addition of CA, on the other hand, led to a change in the shape of the secondary particles, yet the results were not reproducible.

When the AA and CA were added together to the reaction medium, the primary particles became elongated, and the secondary particles were ellipsoids. Compared to the particles synthesized without using organic acids, the BET surface area of particles was similar (23 m²/g and 25 m²/g with and without organics acids, respectively), yet the tap density of particles almost doubled (1.83 ± 0.10 g/cm³ and 0.99 ± 0.04 g/cm³ with and without organics acids, respectively) and the suspension viscosity was halved (6.3 mPa·s and 3.3 mPa·s with and without organics acids, respectively for suspensions with solids loading of 40 wt.%), probably because of the changes in the morphology and the surface characteristics of the particles.

Polyol route allows in situ interventions because of being an open atmosphere synthesis technique. Benefiting from the open atmosphere synthesis conditions, the reaction was intervened with AA addition 15 minutes after the reaction medium including CA reached 170 °C. While the secondary particles were preserved their

size and shape, the primaries of the synthesized particles were spherical shaped and much smaller in size. Doubling the CA concentration in the same experimental conditions, led to almost doubling of secondary particle size particularly in one dimension while showing no direct effect on the primary particles. These results clearly showed that when the reaction conditions were intervened, the size and the morphology of both primary and secondary particles can be tuned. The particles synthesized with intervention and using the same amount of CA with previous experiments, resulted in the tap density of $1.98 \pm 0.10 \text{ g/cm}^3$ and the suspension viscosities of 2.7 mPa·s were obtained. This is the highest tap density value reported in the open literature to the best of our knowledge. Considering the viscosity of pure water is being 1.0 mPa·s, such a low viscosity of suspensions has a potential to ease the electrode processing for LIBs and decrease the power requirement for suspension flow batteries. Moreover, decreasing the suspension viscosity for the same solids loading commonly indicates that the maximum amount of particles that can be load in a unit volume can be increased without sacrificing the flow ability. When the particles are electroactive, then the increase in maximum solids loading can be translated into the increase volumetric energy density for electrodes. The high tap density values achieved in this work support this conclusion.

REFERENCES

1. Barker, J., Saidi, M. Y. & Swoyer, J. L. A Carbothermal Reduction Method for the Preparation of Electroactive Materials for Lithium Ion Applications. *J. Electrochem. Soc.* **150**, A684 (2003).
2. Sun, J., Li, Z., Ren, X., Wang, L. & Liang, G. High volumetric energy density of LiFePO₄/C microspheres based on xylitol-polyvinyl alcohol complex carbon sources. *J. Alloys Compd.* **773**, 788–795 (2019).
3. Cano, Z. P. *et al.* Batteries and fuel cells for emerging electric vehicle markets. *Nat. Energy* **3**, 279–289 (2018).
4. Goodenough, J. B. & Kim, Y. Challenges for rechargeable Li batteries. *Chem. Mater.* **22**, 587–603 (2010).
5. Xu, J., Dou, S., Liu, H. & Dai, L. Cathode materials for next generation lithium ion batteries. *Nano Energy* **2**, 439–442 (2013).
6. Liu, J., Kopold, P., van Aken, P. A., Maier, J. & Yu, Y. Energy Storage Materials from Nature through Nanotechnology: A Sustainable Route from Reed Plants to a Silicon Anode for Lithium-Ion Batteries. *Angew. Chemie* **127**, 9768–9772 (2015).
7. Chen, R. *et al.* A Comparative Review of Electrolytes for Organic-Material-Based Energy-Storage Devices Employing Solid Electrodes and Redox Fluids. *ChemSusChem* **13**, 2205–2219 (2020).
8. Xu, K. Nonaqueous liquid electrolytes for lithium-based rechargeable batteries. *Chem. Rev.* **104**, 4303–4417 (2004).
9. Park, M., Ryu, J., Wang, W. & Cho, J. Material design and engineering of next-generation flow-battery technologies. *Nat. Rev. Mater.* **2**, (2016).
10. Wang, W. *et al.* Recent progress in redox flow battery research and development. *Adv. Funct. Mater.* **23**, 970–986 (2013).

11. Qi, Z. & Koenig, G. M. Review Article: Flow battery systems with solid electroactive materials. *J. Vac. Sci. Technol. B, Nanotechnol. Microelectron. Mater. Process. Meas. Phenom.* **35**, 040801 (2017).
12. Duduta, M. *et al.* Semi-solid lithium rechargeable flow battery. *Adv. Energy Mater.* **1**, 511–516 (2011).
13. Geng, L., Foley, S. B., Dong, H. & Koenig, G. M. LiFePO₄ -Accelerated Change in Surface and Electrochemical Properties in Aqueous Systems Induced by Mechanical Agitation. *Energy Technol.* **7**, (2019).
14. Wei, X. *et al.* Materials and Systems for Organic Redox Flow Batteries: Status and Challenges. *ACS Energy Lett.* **2**, 2187–2204 (2017).
15. Skyllas-Kazacos, M., Chakrabarti, M. H., Hajimolana, S. A., Mjalli, F. S. & Saleem, M. Progress in Flow Battery Research and Development. *J. Electrochem. Soc.* **158**, R55 (2011).
16. Wang, Y., Yi, J. & Xia, Y. Recent progress in aqueous lithium-ion batteries. *Adv. Energy Mater.* **2**, 830–840 (2012).
17. Chang, Z. *et al.* A lithium ion battery using an aqueous electrolyte solution. *Sci. Rep.* **6**, 2–7 (2016).
18. Chen, X., Shen, W., Vo, T. T., Cao, Z. & Kapoor, A. An overview of lithium-ion batteries for electric vehicles. *10th Int. Power Energy Conf. IPEC 2012* 230–235 (2012) doi:10.1109/ASSCC.2012.6523269.
19. Eftekhari, A. LiFePO₄/C nanocomposites for lithium-ion batteries. *J. Power Sources* **343**, 395–411 (2017).
20. Deng, H. *et al.* Synthesis of cage-like LiFePO₄/C microspheres for high performance lithium ion batteries. *J. Power Sources* **220**, 342–347 (2012).
21. Di Lupo, F., Meligrana, G., Gerbaldi, C., Bodoardo, S. & Penazzi, N. Surfactant-assisted mild solvothermal synthesis of nanostructured LiFePO₄/C

- cathodes evidencing ultrafast rate capability. *Electrochim. Acta* **156**, 188–198 (2015).
22. Tian, Y. *et al.* Promises and Challenges of Next-Generation ‘beyond Li-ion’ Batteries for Electric Vehicles and Grid Decarbonization. *Chem. Rev.* **121**, 1623–1669 (2021).
 23. Zhang, X., Porras-Gutierrez, A. G., Mauger, A., Groult, H. & Julien, C. M. Nanotechnology of positive electrodes for Li-Ion batteries. *Inorganics* **5**, 1–17 (2017).
 24. Uddin, M. J., Alaboina, P. K. & Cho, S. J. Nanostructured cathode materials synthesis for lithium-ion batteries. *Mater. Today Energy* **5**, 138–157 (2017).
 25. Guo, X. *et al.* Solid-state synthesis and electrochemical performance of Li₄Ti₅O₁₂/graphene composite for lithium-ion batteries. *Electrochim. Acta* **109**, 33–38 (2013).
 26. Santhanam, R. & Rambabu, B. Research progress in high voltage spinel LiNi_{0.5}Mn_{1.5}O₄ material. *J. Power Sources* **195**, 5442–5451 (2010).
 27. Satyavani, T. V. S. L., Srinivas Kumar, A. & Subba Rao, P. S. V. Methods of synthesis and performance improvement of lithium iron phosphate for high rate Li-ion batteries: A review. *Eng. Sci. Technol. an Int. J.* **19**, 178–188 (2016).
 28. Hu, M. Z. C., Miller, G. A., Payzant, E. A. & Rawn, C. J. Homogeneous (co)precipitation of inorganic salts for synthesis of monodispersed barium titanate particles. *J. Mater. Sci.* **35**, 2927–2936 (2000).
 29. Yeap, S. P. Permanent agglomerates in powdered nanoparticles: Formation and future prospects. *Powder Technol.* **323**, 51–59 (2018).
 30. DYNYS, F. W. & HALLORAN, J. W. Influence of Aggregates on Sintering. *J. Am. Ceram. Soc.* **67**, 596–601 (1984).

31. Benedek, P., Wenzler, N., Yarema, M. & Wood, V. C. Low temperature hydrothermal synthesis of battery grade lithium iron phosphate. *RSC Adv.* **7**, 17763–17767 (2017).
32. Wang, L. *et al.* Nano particle LiFePO₄ prepared by solvothermal process. *J. Power Sources* **244**, 94–100 (2013).
33. Dong, H., Chen, Y. C. & Feldmann, C. Polyol synthesis of nanoparticles: status and options regarding metals, oxides, chalcogenides, and non-metal elements. *Green Chem.* **17**, 4107–4132 (2015).
34. Lee, J. H., Lee, P., Lee, D., Lee, S. S. & Ko, S. H. Large-scale synthesis and characterization of very long silver nanowires via successive multistep growth. *Cryst. Growth Des.* **12**, 5598–5605 (2012).
35. Johan, M. R. *et al.* Synthesis and growth mechanism of silver nanowires through different mediated agents (CuCl₂ and NaCl) polyol process. *J. Nanomater.* **2014**, (2014).
36. Poul, L., Jouini, N. & Fievet, F. Layered hydroxide metal acetates (metal = zinc, cobalt, and nickel): Elaboration via hydrolysis in polyol medium and comparative study. *Chem. Mater.* **12**, 3123–3132 (2000).
37. Fievet, F. *et al.* The polyol process: a unique method for easy access to metal nanoparticles with tailored sizes, shapes and compositions. *Chem. Soc. Rev.* **47**, 5187–5233 (2018).
38. Bandwar, R. P. & Rao, C. P. Relative reducing abilities in vitro of some hydroxy-containing compounds, including monosaccharides, towards vanadium(V) and molybdenum(VI). *Carbohydr. Res.* **277**, 197–207 (1995).
39. Kim, D. *et al.* Synthesis of highly crystalline olivine-type LiFePO₄ nanoparticles by solution-based reactions. *Surf. Rev. Lett.* **17**, 111–119 (2010).
40. Larcher, D. & Patrice, R. Preparation of metallic powders and alloys in polyol media: A thermodynamic approach. *J. Solid State Chem.* **154**, 405–411

- (2000).
41. Singh, M., Singh, B. & Willert-Porada, M. Reaction mechanism and morphology of the LiFePO₄ materials synthesized by chemical solution deposition and solid-state reaction. *J. Electroanal. Chem.* **790**, 11–19 (2017).
 42. Zhou, Y. X. *et al.* Hierarchical FeWO₄ microcrystals: Solvothermal synthesis and their photocatalytic and magnetic properties. *Inorg. Chem.* **48**, 1082–1090 (2009).
 43. Yan, C. & Xue, D. Morphosynthesis of hierarchical hydrozincite with tunable surface architectures and hollow zinc oxide. *J. Phys. Chem. B* **110**, 11076–11080 (2006).
 44. Ghoshal, T., Kar, S. & Chaudhuri, S. ZnO Doughnuts: Controlled Synthesis, Growth Mechanism, and Optical Properties. *Cryst. Growth Des.* **7**, 136–141 (2007).
 45. Sivakumar, M., Muruganatham, R. & Subadevi, R. Synthesis of surface modified LiFePO₄ cathode material via polyol technique for high rate lithium secondary battery. *Appl. Surf. Sci.* **337**, 234–240 (2015).
 46. Hu, Y. K. *et al.* Synthesis of rod-like LiFePO₄/c materials with different aspect ratios by polyol process. *Wuli Huaxue Xuebao/Acta Phys. - Chim. Sin.* **30**, 75–82 (2014).
 47. Kim, D. H. & Kim, J. Synthesis of LiFePO₄ nanoparticles in polyol medium and their electrochemical properties. *Electrochem. Solid-State Lett.* **9**, (2006).
 48. Lu, J. *et al.* Synthesis and optimization of three-dimensional lamellar LiFePO₄ and nanocarbon composite cathode materials by polyol process. *Ceram. Int.* **42**, 1281–1292 (2016).
 49. Sinha, N. N. & Munichandraiah, N. Single-Shot Preparation of Crystalline Nanoplate LiFePO₄ by a Simple Polyol Route. *J. Electrochem. Soc.* **157**, A824 (2010).

50. Singh, M. & Willert-Porada, M. Polyol process for the synthesis of LiFePO₄ rhombohedral particles. *Adv. Powder Technol.* **22**, 284–289 (2011).
51. Mathew, V. *et al.* Morphology-controlled LiFePO₄ cathodes by a simple polyol reaction for Li-ion batteries. *Mater. Charact.* **89**, 93–101 (2014).
52. Wu, G., Zhou, Y., Gao, X. & Shao, Z. Facile low-temperature polyol process for LiFePO₄ nanoplate and carbon nanotube composite. *Solid State Sci.* **24**, 15–20 (2013).
53. Azib, T. *et al.* Crystallinity of nano C-LiFePO₄ prepared by the polyol process. *J. Power Sources* **217**, 220–228 (2012).
54. Wu, G., Zhou, Y. & Shao, Z. Carbon nanotube and graphene nanosheet co-modified LiFePO₄ nanoplate composite cathode material by a facile polyol process. *Appl. Surf. Sci.* **283**, 999–1005 (2013).
55. Kim, D. H., Kim, T. R., Im, J. S., Kang, J. W. & Kim, J. A new method to synthesize olivine phosphate nanoparticles. *Phys. Scr. T* **T129**, 31–34 (2007).
56. Li, S. *et al.* A facile route to modify ferrous phosphate and its use as an iron-containing resource for LiFePO₄ via a polyol process. *ACS Appl. Mater. Interfaces* **6**, 9449–9457 (2014).
57. Wu, G. *et al.* 3D amorphous carbon and graphene co-modified LiFePO₄ composite derived from polyol process as electrode for high power lithium-ion batteries. *J. Energy Chem.* **23**, 363–375 (2014).
58. Kim, D. H. & Kim, J. Synthesis of LiFePO₄ nanoparticles and their electrochemical properties. *J. Phys. Chem. Solids* **68**, 734–737 (2007).
59. Huang, C., Ai, D., Wang, L. & He, X. LiFePO₄ Crystal Growth during Coprecipitation. *Int. J. Electrochem. Sci.* **11**, 754–762 (2016).
60. Yang, C. *et al.* Synthesis of nano-sized urchin-shaped LiFePO₄ for lithium ion batteries. *RSC Adv.* **9**, 13714–13721 (2019).

61. Abid, N. *et al.* Synthesis of nanomaterials using various top-down and bottom-up approaches, influencing factors, advantages, and disadvantages: A review. *Adv. Colloid Interface Sci.* **300**, 102597 (2022).
62. Thanh, N. T. K., Maclean, N. & Mahiddine, S. Mechanisms of nucleation and growth of nanoparticles in solution. *Chem. Rev.* **114**, 7610–7630 (2014).
63. Ammar, S. & Fiévet, F. Polyol synthesis: A versatile wet-chemistry route for the design and production of functional inorganic nanoparticles. *Nanomaterials* **10**, 1–8 (2020).
64. Nguyen, T. D. From formation mechanisms to synthetic methods toward shape-controlled oxide nanoparticles. *Nanoscale* **5**, 9455–9482 (2013).
65. Malik, R., Burch, D., Bazant, M. & Ceder, G. Particle size dependence of the ionic diffusivity. *Nano Lett.* **10**, 4123–4127 (2010).
66. Nan, C. *et al.* Size and shape control of LiFePO₄ nanocrystals for better lithium ion battery cathode materials. *Nano Res.* **6**, 469–477 (2013).
67. Vu, A. & Stein, A. Multiconstituent synthesis of LiFePO₄/C composites with hierarchical porosity as cathode materials for lithium ion batteries. *Chem. Mater.* **23**, 3237–3245 (2011).
68. Oh, S. W. *et al.* Polyvinylpyrrolidone-assisted synthesis of microscale C-LiFePO₄ with high tap density as positive electrode materials for lithium batteries. *Electrochim. Acta* **55**, 1193–1199 (2010).
69. Du, X. & Zhang, B. Robust Solid Electrolyte Interphases in Localized High Concentration Electrolytes Boosting Black Phosphorus Anode for Potassium-Ion Batteries. *ACS Nano* **15**, 16851–16860 (2021).
70. An, S. J. *et al.* The state of understanding of the lithium-ion-battery graphite solid electrolyte interphase (SEI) and its relationship to formation cycling. *Carbon N. Y.* **105**, 52–76 (2016).

71. Nadimpalli, S. P. V. *et al.* Quantifying capacity loss due to solid-electrolyte-interphase layer formation on silicon negative electrodes in lithium-ion batteries. *J. Power Sources* **215**, 145–151 (2012).
72. Genovese, D. B. Shear rheology of hard-sphere, dispersed, and aggregated suspensions, and filler-matrix composites. *Adv. Colloid Interface Sci.* **171–172**, 1–16 (2012).
73. Saravanan, K., Balaya, P., Reddy, M. V., Chowdari, B. V. R. & Vittal, J. J. Morphology controlled synthesis of LiFePO₄/C nanoplates for Li-ion batteries. *Energy Environ. Sci.* **3**, 457–464 (2010).
74. Ma, Z. *et al.* Tunable morphology synthesis of LiFePO₄ nanoparticles as cathode materials for lithium ion batteries. *ACS Appl. Mater. Interfaces* **6**, 9236–9244 (2014).
75. Chen, Z., Zhang, W. & Yang, Z. A review on cathode materials for advanced lithium ion batteries: Microstructure designs and performance regulations. *Nanotechnology* **31**, (2020).
76. Xu, G. L. *et al.* Tuning the structure and property of nanostructured cathode materials of lithium ion and lithium sulfur batteries. *J. Mater. Chem. A* **2**, 19941–19962 (2014).
77. Wang, Y., Zhang, D., Chang, C., Deng, L. & Huang, K. Controllable growth of LiFePO₄ microplates of (010) and (001) lattice planes for Li ion batteries: A case of the growth manner on the Li ion diffusion coefficient and electrochemical performance. *Mater. Chem. Phys.* **148**, 933–939 (2014).
78. Pei, B., Yao, H., Zhang, W. & Yang, Z. Hydrothermal synthesis of morphology-controlled LiFePO₄ cathode material for lithium-ion batteries. *J. Power Sources* **220**, 317–323 (2012).
79. Chateau, X. *Particle packing and the rheology of concrete. Understanding the Rheology of Concrete* (Woodhead Publishing Limited, 2012).

doi:10.1533/9780857095282.2.117.

80. Jin, Y. *et al.* High-tap density LiFePO₄ microsphere developed by combined computational and experimental approaches. *CrystEngComm* **20**, 6695–6703 (2018).
81. Donev, A. *et al.* Improving the Density of Jammed Disordered Packings Using Ellipsoids. *Science (80-.)*. **303**, 990–993 (2004).
82. Rueda, M. M. *et al.* Rheology and applications of highly filled polymers: A review of current understanding. *Prog. Polym. Sci.* **66**, 22–53 (2017).
83. Jiang, J., Oberdörster, G. & Biswas, P. Characterization of size, surface charge, and agglomeration state of nanoparticle dispersions for toxicological studies. *J. Nanoparticle Res.* **11**, 77–89 (2009).
84. Xia, Y., Yoshio, M. & Noguchi, H. Improved electrochemical performance of LiFePO₄ by increasing its specific surface area. *Electrochim. Acta* **52**, 240–245 (2006).
85. Kraytsberg, A. & Ein-Eli, Y. Conveying Advanced Li-ion Battery Materials into Practice The Impact of Electrode Slurry Preparation Skills. *Adv. Energy Mater.* **6**, (2016).
86. Hawley, W. B. & Li, J. Electrode manufacturing for lithium-ion batteries—Analysis of current and next generation processing. *J. Energy Storage* **25**, 100862 (2019).
87. Wenzel, V., Nirschl, H. & Nötzel, D. Challenges in Lithium-Ion-Battery Slurry Preparation and Potential of Modifying Electrode Structures by Different Mixing Processes. *Energy Technol.* **3**, 692–698 (2015).
88. Ponrouch, A. & Palacín, M. R. On the impact of the slurry mixing procedure in the electrochemical performance of composite electrodes for Li-ion batteries: A case study for mesocarbon microbeads (MCMB) graphite and Co₃O₄. *J. Power Sources* **196**, 9682–9688 (2011).

89. Sullivan, J. P. & Bose, A. On the connection between slurry rheology and electrochemical performance of graphite anodes in Lithium-ion batteries. *Electrochem. commun.* **141**, 107353 (2022).
90. Sato, K., Li, J. G., Kamiya, H. & Ishigaki, T. Ultrasonic dispersion of TiO₂ nanoparticles in aqueous suspension. *J. Am. Ceram. Soc.* **91**, 2481–2487 (2008).
91. Mat, A., Sulaiman, K. S. & Arof, A. K. Effect of citric acid on the performance of LiFePO₄ as a cathode material for lithium batteries. *Ionics (Kiel)*. **22**, 135–142 (2016).
92. Kanagaraj, A. B., Chaturvedi, P., Kim, H. J. & Choi, D. S. Controllable synthesis of LiFePO₄ microrods and its superior electrochemical performance. *Mater. Lett.* **283**, 128737 (2021).
93. Meligrana, G., Gerbaldi, C., Tuel, A., Bodoardo, S. & Penazzi, N. Hydrothermal synthesis of high surface LiFePO₄ powders as cathode for Li-ion cells. *J. Power Sources* **160**, 516–522 (2006).
94. Chen, Z. yong, Zhu, H. li, Ji, S., Fakir, R. & Linkov, V. Influence of carbon sources on electrochemical performances of LiFePO₄/C composites. *Solid State Ionics* **179**, 1810–1815 (2008).
95. Lin, J. Multiform oxide optical materials via the versatile pechini-type sol-gel process. *Proc. Int. Meet. Inf. Disp.* **8**, 1247–1250 (2008).
96. Qian, J., Zhou, M., Cao, Y., Ai, X. & Yang, H. Template-free hydrothermal synthesis of nanoembossed mesoporous LiFePO₄ microspheres for high-performance lithium-ion batteries. *J. Phys. Chem. C* **114**, 3477–3482 (2010).
97. Zhang, D. *et al.* Ballmilling-Assisted Synthesis and Electrochemical Performance of LiFePO₄/C for Lithium-Ion Battery Adopting Citric Acid as Carbon Precursor. *J. Electrochem. Soc.* **156**, A802 (2009).
98. Yang, M. R., Ke, W. H. & Wu, S. H. Preparation of LiFePO₄ powders by co-

- precipitation. *J. Power Sources* **146**, 539–543 (2005).
99. Ni, J. *et al.* Hydrothermal preparation of LiFePO₄ nanocrystals mediated by organic acid. *J. Power Sources* **195**, 2877–2882 (2010).
 100. Lee, J. H. *et al.* Evaluation of surface acid and base properties of LiFePO₄ in aqueous medium with pH and its electrochemical properties. *J. Phys. Chem. C* **114**, 4466–4472 (2010).
 101. Qin, X. *et al.* Mechanism for hydrothermal synthesis of LiFePO₄ platelets as cathode material for lithium-ion batteries. *J. Phys. Chem. C* **114**, 16806–16812 (2010).
 102. Liu, J., Jiang, R., Wang, X., Huang, T. & Yu, A. The defect chemistry of LiFePO₄ prepared by hydrothermal method at different pH values. *J. Power Sources* **194**, 536–540 (2009).
 103. Gu, Y. J. *et al.* Novel synthesis of plate-like LiFePO₄ by hydrothermal method. *J. New Mater. Electrochem. Syst.* **19**, 33–36 (2016).
 104. Song, Q., Ou, X., Wang, L., Liang, G. & Wang, Z. Effect of pH value on particle morphology and electrochemical properties of LiFePO₄ by hydrothermal method. *Mater. Res. Bull.* **46**, 1398–1402 (2011).
 105. Lin, M. *et al.* Morphology-Controlled Synthesis of Self-Assembled LiFePO₄/C/RGO for High-Performance Li-Ion Batteries. (2014).
 106. Huang, X., He, X., Jiang, C. & Tian, G. Morphology evolution and impurity analysis of LiFePO₄ nanoparticles via a solvothermal synthesis process. *RSC Adv.* **4**, 56074–56083 (2014).
 107. Yang, L. *et al.* LiFePO₄ nanoplates with {010} exposed active planes prepared by hydrothermal method. *J. Mater. Sci. Mater. Electron.* **27**, 12258–12263 (2016).
 108. Wu, Y. F. *et al.* Hierarchical carbon-coated LiFePO₄ nano-grain microspheres

- with high electrochemical performance as cathode for lithium ion batteries. *J. Power Sources* **256**, 336–344 (2014).
109. Wei, W., Chen, D., Wang, R. & Guo, L. Hierarchical LiFePO₄/C microspheres with high tap density assembled by nanosheets as cathode materials for high-performance Li-ion batteries. *Nanotechnology* **23**, (2012).
 110. Wang, Q. *et al.* Hydrothermal synthesis of hierarchical LiFePO₄ microspheres for lithium ion battery. *J. Alloys Compd.* **553**, 69–74 (2013).
 111. Wang, Q., Zhang, W., Yang, Z., Weng, S. & Jin, Z. Solvothermal synthesis of hierarchical LiFePO₄ microflowers as cathode materials for lithium ion batteries. *J. Power Sources* **196**, 10176–10182 (2011).
 112. Xia, Y. *et al.* Self-assembled mesoporous LiFePO₄ with hierarchical spindle-like architectures for high-performance lithium-ion batteries. *J. Power Sources* **196**, 5651–5658 (2011).
 113. Guo, B., Ruan, H., Zheng, C., Fei, H. & Wei, M. Hierarchical LiFePO₄ with a controllable growth of the (010) facet for lithium-ion batteries. *Sci. Rep.* **3**, (2013).
 114. Wang, M., Yang, Y. & Zhang, Y. Synthesis of micro-nano hierarchical structured LiFePO₄/C composite with both superior high-rate performance and high tap density. *Nanoscale* **3**, 4434–4439 (2011).
 115. Ravet, N. *et al.* Mechanism of the Fe³⁺ reduction at low temperature for LiFePO₄ synthesis from a polymeric additive. *Chem. Mater.* **19**, 2595–2602 (2007).
 116. Carroll, K. J., Reveles, J. U., Shultz, M. D., Khanna, S. N. & Carpenter, E. E. Preparation of elemental Cu and Ni nanoparticles by the polyol method: An experimental and theoretical approach. *J. Phys. Chem. C* **115**, 2656–2664 (2011).
 117. Wei, Z., Qiao, H., Yang, H., Zhang, C. & Yan, X. Characterization of NiO

- nanoparticles by anodic arc plasma method. *J. Alloys Compd.* **479**, 855–858 (2009).
118. Sun, C., Rajasekhara, S., Goodenough, J. B. & Zhou, F. Monodisperse porous LiFePO₄ microspheres for a high power Li-ion battery cathode. *J. Am. Chem. Soc.* **133**, 2132–2135 (2011).
 119. Kyaw, A. M. M., Panomsuwan, G. & Munprom, R. Solid-state reaction synthesis and characterization of Mn-doped LiFePO₄ cathode material. *IOP Conf. Ser. Mater. Sci. Eng.* **1234**, 012029 (2022).
 120. Zhang, T., Lin, S. & Yu, J. Influence Mechanism of Precursor Crystallinity on Electrochemical Performance of LiFePO₄/C Cathode Material. *Ind. Eng. Chem. Res.* **61**, 5181–5190 (2022).
 121. Huang, C. Y., Kuo, T. R., Yougbaré, S. & Lin, L. Y. Design of LiFePO₄ and porous carbon composites with excellent High-Rate charging performance for Lithium-Ion secondary battery. *J. Colloid Interface Sci.* **607**, 1457–1465 (2022).
 122. Logan, E. R. *et al.* The Effect of LiFePO₄ Particle Size and Surface Area on the Performance of LiFePO₄/Graphite Cells. *J. Electrochem. Soc.* **169**, 050524 (2022).
 123. Zhang, X., Ai, Z., Jia, F. & Zhang, L. Generalized one-pot synthesis, characterization, and photocatalytic activity of hierarchical BiOX (X = Cl, Br, I) nanoplate microspheres. *J. Phys. Chem. C* **112**, 747–753 (2008).
 124. Rangappa, D., Sone, K., Kudo, T. & Honma, I. Directed growth of nanoarchitected LiFePO₄ electrode by solvothermal synthesis and their cathode properties. *J. Power Sources* **195**, 6167–6171 (2010).
 125. Burba, C. M. & Frech, R. Raman and FTIR Spectroscopic Study of Li_xFePO₄ (0 ≤ x ≤ 1). *J. Electrochem. Soc.* **151**, A1032 (2004).
 126. Zhang, G. *et al.* Removal of Organics by Pyrolysis for Enhancing Liberation

and Flotation Behavior of Electrode Materials Derived from Spent Lithium-Ion Batteries. *ACS Sustain. Chem. Eng.* **8**, 2205–2214 (2020).

127. Wu, S. H., Hsiao, K. M. & Liu, W. R. The preparation and characterization of olivine LiFePO₄ by a solution method. *J. Power Sources* **146**, 550–554 (2005).
128. Xing, Y. *et al.* LiFePO₄/C composite with 3D carbon conductive network for rechargeable lithium ion batteries. *Electrochim. Acta* **109**, 512–518 (2013).
129. Huang, X., He, X., Jiang, C., Tian, G. & Liu, Y. Reaction Mechanisms on Solvothermal Synthesis of Nano LiFePO₄ Crystals and Defect Analysis. *Ind. Eng. Chem. Res.* **56**, 10648–10657 (2017).
130. Qin, X. *et al.* Hydrothermally synthesized LiFePO₄ crystals with enhanced electrochemical properties: Simultaneous suppression of crystal growth along [010] and antisite defect formation. *Phys. Chem. Chem. Phys.* **14**, 2669–2677 (2012).
131. Lan, J., Hou, H., Huang, B., Li, H. & Li, J. The positive role of vitamin C in spindle-like LiFePO₄/C cathode derived from two wastes. *Ionics (Kiel)*. **28**, 1583–1593 (2022).
132. Pieliowski, K. & Flejtuch, K. Non-oxidative thermal degradation of poly(ethylene oxide): Kinetic and thermoanalytical study. *J. Anal. Appl. Pyrolysis* **73**, 131–138 (2005).
133. Pang, S. F., Wu, C. Q., Zhang, Q. N. & Zhang, Y. H. The structural evolution of magnesium acetate complex in aerosols by FTIR-ATR spectra. *J. Mol. Struct.* **1087**, 46–50 (2015).
134. Shukla, N., Liu, C., Jones, P. M. & Weller, D. FTIR study of surfactant bonding to FePt nanoparticles. *J. Magn. Magn. Mater.* **266**, 178–184 (2003).
135. Caccamo, M. T. & Magazù, S. Thermal restraint on PEG-EG mixtures by FTIR investigations and wavelet cross-correlation analysis. *Polym. Test.* **62**,

- 311–318 (2017).
136. Dubois, I. E., Holgersson, S., Allard, S. & Malmström, M. E. Dependency of BET surface area on particle size for some granitic minerals. *Proc. Radiochem.* **1**, 75–82 (2020).
 137. Robinson, B. C. S. Some Factors Influencing Sedimentation1 average dimension of particles. **58**, 869–871 (1926).
 138. Zhang, W. J. Structure and performance of LiFePO₄ cathode materials: A review. *J. Power Sources* **196**, 2962–2970 (2011).
 139. Wildemuth, C. R. & Williams, M. C. Viscosity of suspensions modeled with a shear-dependent maximum packing fraction. *Rheol. Acta* **23**, 627–635 (1984).
 140. Cross, M. M. Relation between viscoelasticity and shear-thinning behaviour in liquids. *Rheol. Acta* **18**, 609–614 (1979).
 141. Yin, H. & Casey, P. S. Effects of aspect ratio (AR) and specific surface area (SSA) on cytotoxicity and phototoxicity of ZnO nanomaterials. *Chemosphere* **124**, 116–121 (2015).
 142. Simha, R. A treatment of the viscosity of concentrated suspensions. *J. Appl. Phys.* **23**, 1020–1024 (1952).
 143. Bennett, G. The merck index: An encyclopedia of chemicals, drugs and biologicals. *Journal of Hazardous Materials* vol. 30 373 at [https://doi.org/10.1016/0304-3894\(92\)87022-8](https://doi.org/10.1016/0304-3894(92)87022-8) (1992).
 144. Relations, V. P. P. Glycol-Water Mixtures. 66–68.

APPENDICES

A. BOILING POINT OF REACTION MEDIUM AND YIELD CALCULATIONS

Boiling Point of Reaction Medium

When EG is mixed with water, its boiling point decreases. The maximum temperature that can be reached depends on how much water is present in the reaction medium. The most significant factor affecting the Gibbs free energy is supersaturation, which is affected by the solubility of reagents, and it increases with the amount of water. Considering all these, the amount of water and reagents used are important to adjust reaction temperature, nucleation rate, nuclei size and crystal growth. The amounts of reagents and solvent used for LFP synthesis were given in Table A.1.

Table A.1 Experimental details of LiFePO₄ synthesis without organic acid addition.

Reagent	Number of moles	Weight (g)	Moles of Water
LiOH	0.054	1.29	0
FeSO ₄ ·7H ₂ O	0.018	5.00	0.126
H ₃ PO ₄ (85 wt.%)	0.018*	2.08*	0.017*
EG	3.12	193.46	0

* H₃PO₄ (85 wt.%) was used as PO₄⁻³ reagent. Number of pure H₃PO₄ moles was 0.018, solution weight was 2.075 g and number of water moles coming from solution was 0.017.

0.143 (i.e., 0.126+0.017) moles is equivalent to 2.57 g of water presented in the reaction medium without the addition of extra water to increase the solubility of LiOH in EG. $\frac{2.57 \text{ g}}{(193.46+2.08+5.00+1.29)\text{g}} \times 100 = 1.27 \text{ wt.}\%$ water before the addition of extra water.

While the amount of EG being used for the solubility of the Fe^{2+} and phosphate sources was sufficient, extra water was needed for further dissolution of the Li^+ source. 0.054 moles (0.97 g) of water were added to the LiOH-EG mixture.

$$\frac{(2.57+0.97) \text{ g}}{(193.46+2.08+5.00+1.29+0.97) \text{ g}} \times 100 = 1.75 \text{ wt. \% water after the addition of extra water.}$$

The temperature that could be reached was 173 °C when the water concentration in the reaction medium was 1.75 wt.%. The decreases in the boiling point of EG with increasing water contents at different pressure values were reported¹⁴⁴. The boiling temperatures that had been found at pressure values close to ambient pressure value in Ankara were examined, the observation of a maximum temperature of 173 °C was found reasonable. The reaction medium was a dynamic system that was constantly refluxed. The ratio of water and EG in vapor was different than that in the reaction medium. Due to this additional ambiguity the reaction temperature was fixed at 170 °C to minimize thermal fluctuations.

Reaction Yield Calculations:

In this study, 0.054 mol LiOH, 0.018 mol H_3PO_4 and 0.018 mol $\text{FeSO}_4 \cdot 7\text{H}_2\text{O}$ were used for LFP synthesis.

$0.054 \text{ mol Li}^+ + 0.018 \text{ mol Fe}^{2+} + 0.018 \text{ mol PO}_4^{-3} \rightarrow 0.018 \text{ mol LiFePO}_4$ (2.84 g) is synthesized if the reaction yield is 100%.

2.58 g of LFP was synthesized when reaction temperature (170 °C) was reached.

Reaction yield was $\frac{2.58}{2.84} \times 100 = 91\%$.

2.75 g of LFP was synthesized after 9 hours of synthesis. Reaction yield was

$\frac{2.75}{2.84} \times 100 = 97\%$.

B. HEATING PROFILE OF PRECURSOR SUSPENSION IN THE HEATING MANTLE

The heating profile (Figure B.1) was created by recording the seconds and the corresponding thermocouple readings in the heating mantle as temperature increased.

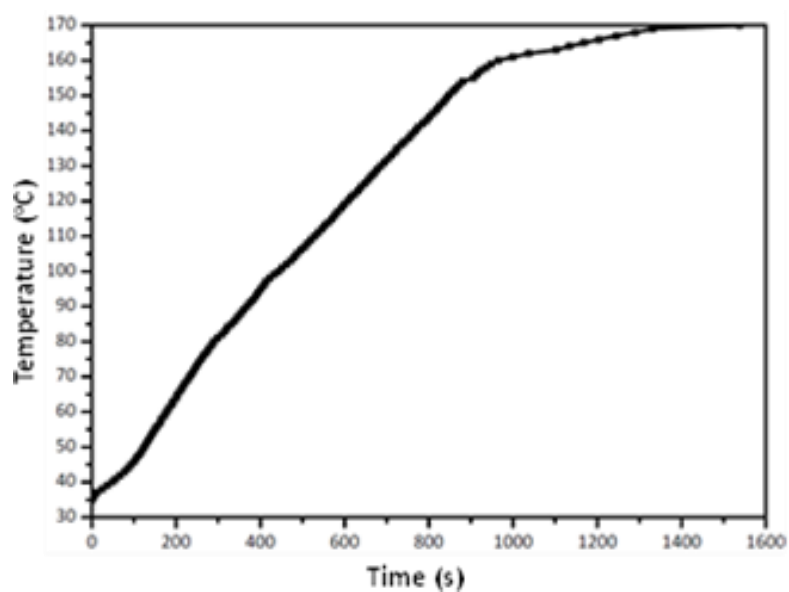


Figure B.1. Heating profile of precursor suspension in the heating mantle.

C. CALCULATIONS OF EXPERIMENTS WITH ORGANIC ACID ADDITION

Experimental details of hydrothermal synthesis in which AA and CA were used separately as crystal growth templating auxiliary reagents are as follows:

0.005 moles $(\text{NH}_4)\text{FeSO}_4 \cdot 6\text{H}_2\text{O}$, and $(\text{NH}_4)\text{H}_2\text{PO}_4$ and 0.015 moles $\text{LiOH} \cdot \text{H}_2\text{O}$ were thoroughly dissolved in 3×10 mL water at room temperature. After mixing the iron precursor, phosphate precursor and 1.04×10^{-3} moles of CA or 1.14×10^{-3} moles of AA, lithium precursor was added¹⁰⁷. The ratio of moles of iron to CA was 4.80 and the ratio of iron to AA was 4.39. These ratios were taken as the basis while designing our experimental procedure. The moles of the iron reagent we used was 0.018. $\frac{0.018}{4.80}$ moles (0.720 g) of CA and $\frac{0.018}{4.39}$ moles (0.722 g) of AA were used.

D. ATR-FTIR DECONVOLUTION WITH FITYK-CURVE FITTING AND PEAK FITTING SOFTWARE

Deconvolution was performed using Fityk-Curve and Fitting Software to determine the positions of the peaks in ATR-FTIR spectra. Before deconvolution, the Savitzky-Golay filter with 9 windows was used 5 times for noise reduction. During the deconvolution of organic regions, 4 ranges in which the peaks were seen were determined as 1750-1500 cm^{-1} , 1600-1450 cm^{-1} , 1450-1300 cm^{-1} and 1230-800 cm^{-1} . Pearson7 function was determined as the most suitable function and used for deconvolution. Stretching vibrations of PO_4^{3-} ions were observed in the 1230-800 cm^{-1} range in both pristine and heat-treated sample (Figure D.1). In pristine LFP particles, peaks are observed in the 1750-1500 cm^{-1} (Figure D.2) and 1450-1300 cm^{-1} (Figure D.4) ranges, while in heat treated samples, these ranges are 1600-1450 cm^{-1} (Figure D.3) and 1450-1300 cm^{-1} (Figure D.5).

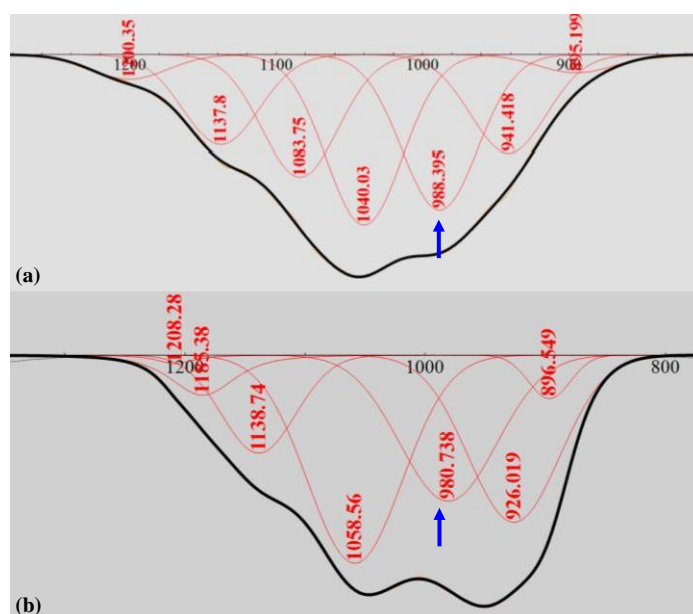


Figure D.1. Deconvolution of ATR-FTIR spectra in the wavenumber range of 1230-800 cm^{-1} for (a) Sample 170 °C 9 h. (b) Sample H. The arrows on the figure show the peaks indicating the anti-site defects.

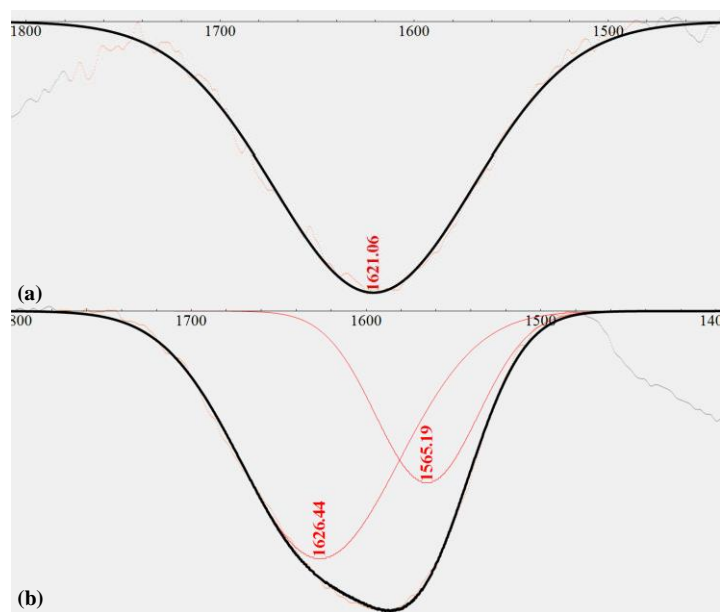


Figure D.2. Deconvolution of ATR-FTIR spectra in the wavenumber range of 1750-1500 cm^{-1} for (a) Sample 170 °C 9 h. (b) Sample H.

E. PARTICLE SIZE ANALYSIS USING IMAGE J SOFTWARE

Average sizes of particles were calculated using Image J software on FE-SEM micrograph. Representative FE-SEM micrographs were given for each sample in the figures below.

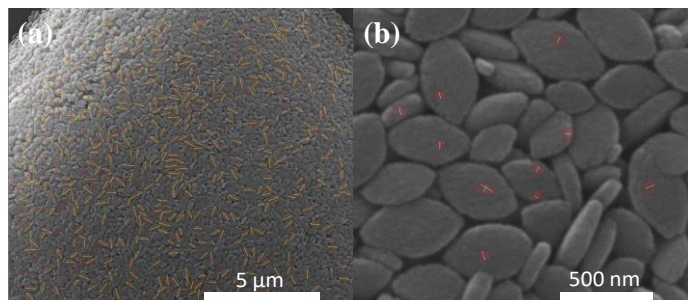


Figure E.1. An example for the average size calculation of Sample LFP_170 °C 9 h. (a) Measurement of secondary particles. (b) Measurement of primary particles.

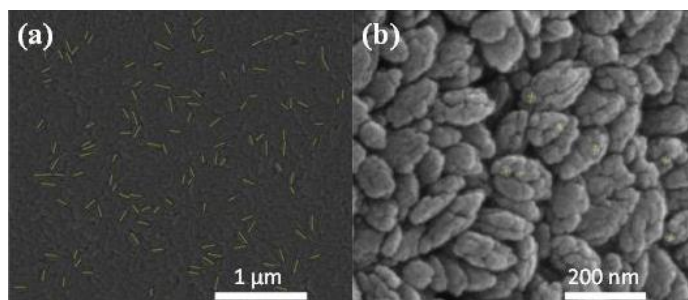


Figure E.2. An example for the average size calculation of Sample A. (a) Measurement of secondary particles. (b) Measurement of primary particles.

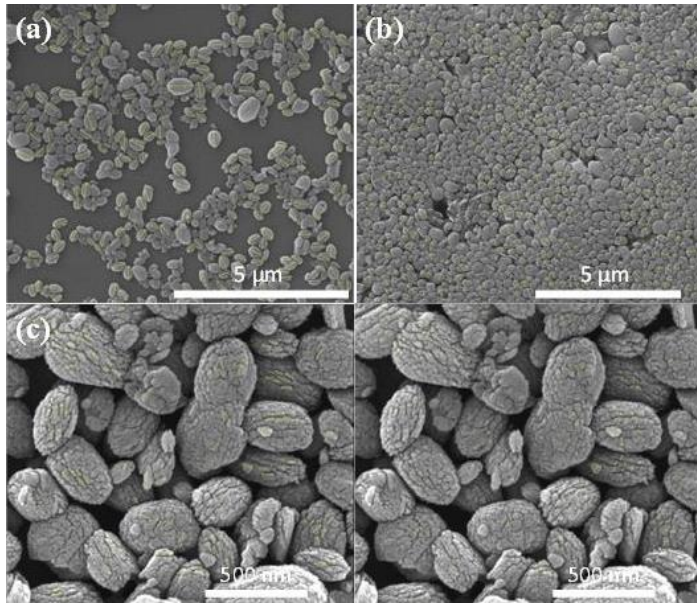


Figure E.3. An example for the average size calculation of Sample C. (a) Measurement of length of secondary particles. (b) Measurement of width of secondary particles. (c) Measurement of length of primary particles. (d) Measurement of width of primary particles.

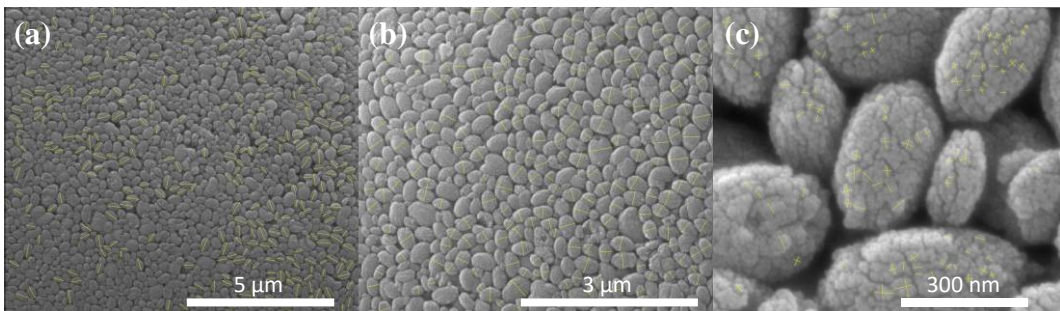


Figure E.4. An example for the average size calculation of Sample D (a) Measurement of length of secondary particles. (b) Measurement of width of secondary particles. (c) Measurement of primary particles.

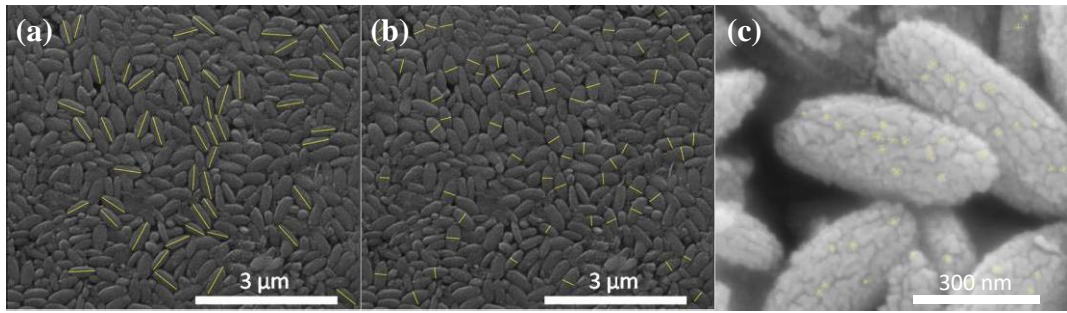


Figure E.5. An example for the average size calculation of Sample E (a) Measurement of length of secondary particles. (b) Measurement of width of secondary particles. (c) Measurement of primary particles.

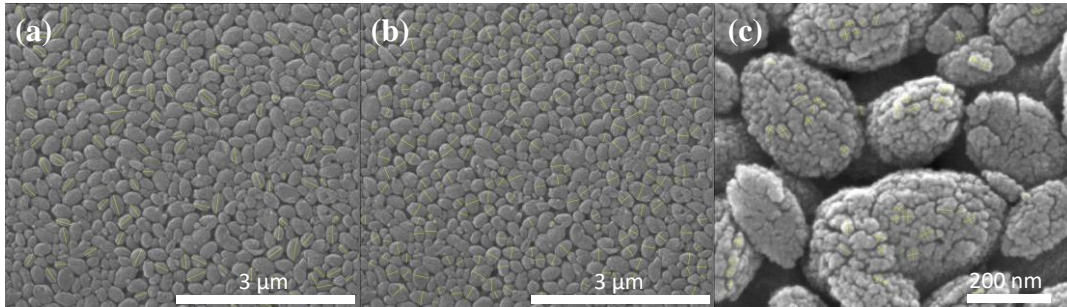


Figure E.6. An example for the average size calculation of Sample F (a) Measurement of length of secondary particles. (b) Measurement of width of secondary particles. (c) Measurement of primary particles.

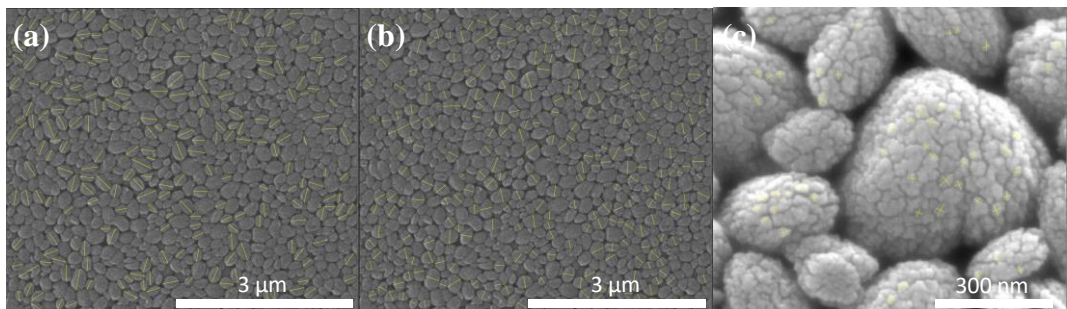


Figure E.7. An example for the average size calculation of Sample G (a) Measurement of length of secondary particles. (b) Measurement of width of secondary particles. (c) Measurement of primary particles.

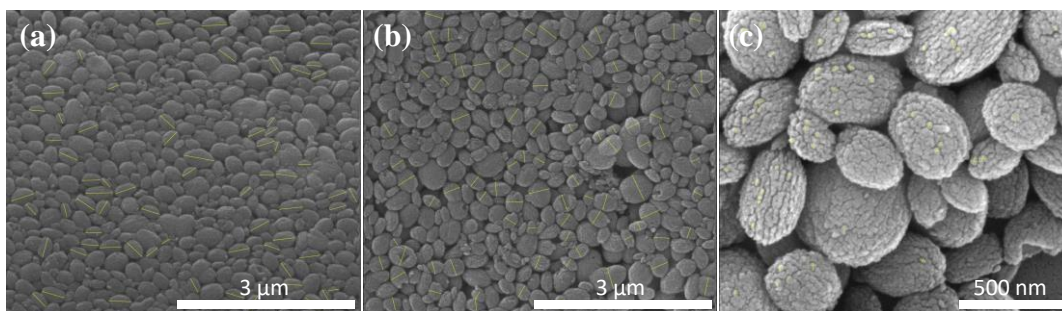


Figure E.8. An example for the average size calculation of Sample H (a) Measurement of length of secondary particles. (b) Measurement of width of secondary particles. (c) Measurement of primary particles.

F. COMPARISON OF ORGANIC AND AQUEOUS ELECTROLYTE

Specific discharge capacities of 170 °C 9 h. was measured both in half cell setup with organic electrolyte and 3-electrode vial cell setup with aqueous electrolyte to reveal the difference between two setups (Figure F.1).

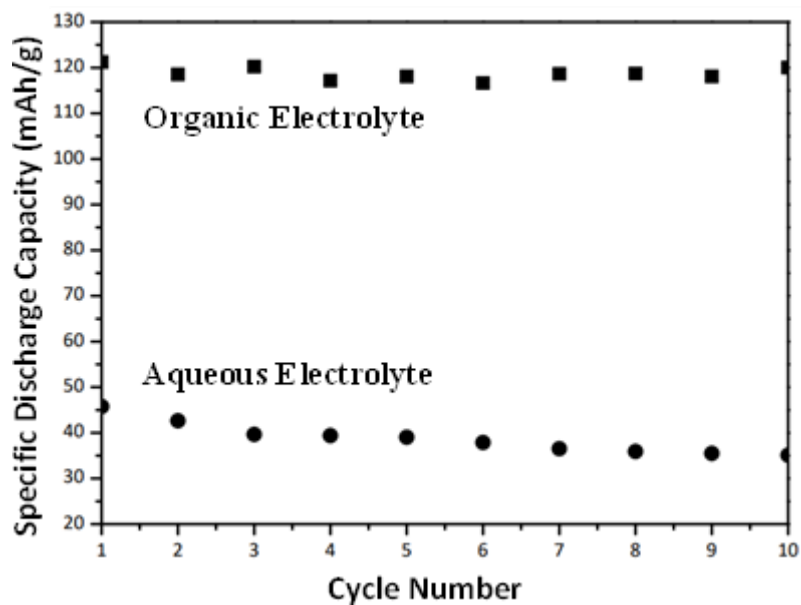


Figure F.1. Specific discharge capacities of 170 °C 9 h. in half cell setup with organic electrolyte and 3-electrode vial cell setup with aqueous electrolyte.